ARO 13817.1-GS

PENN STATE

AD A082129

The Role of Diabatic Heating in Generating Lower Tropospheric Mesoscale Circulations

Contract DAAG29-76-G-0157

Final Report for the Period 23 February 1976 - 31 December 1979

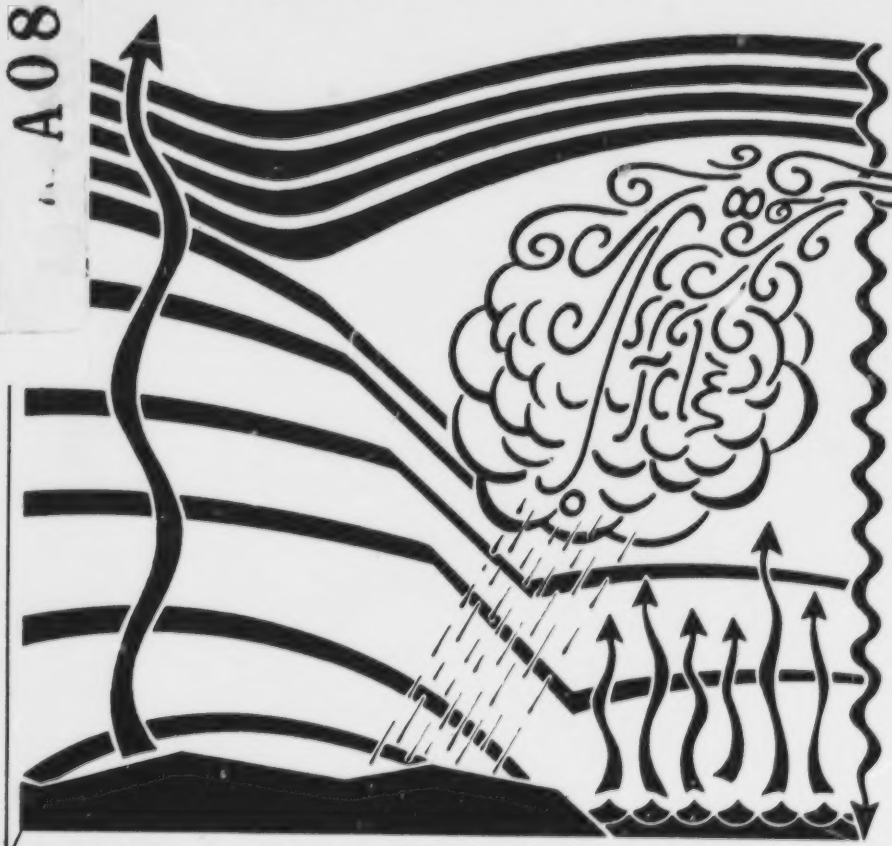

LEVEL II

Thomas T. Warner,
Richard A. Anthes
and
Nelson L. Seaman

December 1979

DTIC
ELECTE
MAR 1 1 1980
S D
C

DEPARTMENT OF METEOROLOGY THE PENNSYLVANIA STATE UNIVERSITY

DDC FILE COPY

Prepared for: U.S. Army Research Office, Geosciences Division
P. O. Box 12211
Research Triangle Park, NC 27709

APPROVED FOR PUBLIC RELEASE; DISTRIBUTION UNLIMITED

80 3 7 056

The findings in this report are not to be construed as an official Department of the Army position, unless so designated by other authorized documents.

SECURITY CLASSIFICATION OF THIS PAGE (When Data Entered)

REPORT DOCUMENTATION PAGE

READ INSTRUCTIONS BEFORE COMPLETING FORM

1. REPORT NUMBER: DAAG29-76-G-0157

2. GOVT ACCESSION NO.:

3. RECIPIENT'S CATALOG NUMBER: (9)

4. TITLE (and Subtitle): (6) The Role of Diabatic Heating in Generating Lower Tropospheric Mesoscale Circulations.

5. TYPE OF REPORT & PERIOD COVERED: Final Report. 23 Feb 76 — 31 Dec 79.

6. PERFORMING ORG. REPORT NUMBER:

7. AUTHOR(s): (10) Thomas T. Warner, Richard A. Anthes, Nelson L. Seaman

8. CONTRACT OR GRANT NUMBER(s): (15) DAAG29-76-G-0157, EPA-R-805659

9. PERFORMING ORGANIZATION NAME AND ADDRESS:
The Pennsylvania State University
503 Walker Building
University Park, PA 16802

10. PROGRAM ELEMENT, PROJECT, TASK AREA & WORK UNIT NUMBERS: (12) 106
NA

11. CONTROLLING OFFICE NAME AND ADDRESS:
U.S. Army Research Office
Post Office Box 12211
Research Triangle Park, NC 27709

12. REPORT DATE: (11) 31 Dec 79

13. NUMBER OF PAGES: 98

14. MONITORING AGENCY NAME & ADDRESS (if different from Controlling Office): (18) ARO
(19) 13817.1-GSX
NA

15. SECURITY CLASS. (of this report): Unclassified

15a. DECLASSIFICATION/DOWNGRADING SCHEDULE: NA

16. DISTRIBUTION STATEMENT (of this Report)

Approved for public release; distribution unlimited.

17. DISTRIBUTION STATEMENT (of the abstract entered in Block 20, if different from Report)

NA

18. SUPPLEMENTARY NOTES

The findings in this report are not to be construed as an official Department of the Army position, unless so designated by other authorized documents.

19. KEY WORDS (Continue on reverse side if necessary and identify by block number)

Mesoscale circulations
Diabatic heating
Mixed-layer model

20. ABSTRACT (Continue on reverse side if necessary and identify by block number)

A two-dimensional, multilevel primitive equation model is used to investigate various characteristics of thermally driven circulations. The sensitivity of the mesoscale circulations to the magnitude of the surface, sensible heat flux is established through examination of various quantifiable circulation features such as the planetary boundary layer depth and the horizontal and vertical wind maxima. The simulations fall into two groups; one deals with circulations over flat terrain in the vicinity of a

(Continued on back)

DD FORM 1 JAN 73 1473 EDITION OF 1 NOV 65 IS OBSOLETE

400 131 JOB

SECURITY CLASSIFICATION OF THIS PAGE (When Data Entered)

20. continued.

coastline and the other deals with circulations induced by heating of the irregular terrain in the vicinity of the Tennessee Valley. The results establish a surprisingly linear relationship between forecast errors and errors in the specification of the surface sensible heat flux.

The results of the Tennessee Valley simulations are verified using satellite visible imagery. The model-predicted subsidence over the valley corresponds very closely in location to anomalous cloud-free regions observed in numerous satellite photographs.

A series of increasingly complicated meteorological circulations is modeled by a two-dimensional, multilevel primitive equation model (MLM) and a one-dimensional mixed layer model (XLM) in order to determine the extent to which the simple mixed-layer model can provide accurate predictions of the mean structure of the planetary boundary layer (PBL). Under horizontally homogeneous conditions, the PBL structure in the XLM agreed closely with the average structure in the MLM. When horizontal inhomogeneities associated with differential heating over complex terrain and across a land-water boundary were introduced, the XLM solutions became less accurate when compared to the MLM solutions. For these conditions a multilevel model appears to be essential to the correct prediction of flow within the PBL, because mass-wind adjustments in the flow above the PBL produce important changes on the pressure gradient within the PBL.

Summary of Research Progress

This report covers progress since 23 February 1976 on investigations into the importance of differential heating on generating mesoscale circulations. The investigations are carried out with relatively simple one- and two-dimensional models, even though most applications will require fully three-dimensional models. By using models with reduced spatial dimensions, it is possible to run many more simulations and to more easily understand the physical processes which affect mesoscale circulations. The insight gained from these simulations often helps in the development and understanding of three-dimensional models.

The physical situations modeled here include circulations induced by differential surface heating over complex terrain and across boundaries between land and water. All simulations start with a stagnant base state and the effects of moisture are neglected. Numerical effects and alternative computational methods are not considered. Future work should include addition of mean flows and moisture effects and consideration of alternative numerical techniques to the finite difference equations utilized in these simulations.

The support of the Army Research Office is acknowledged with thanks. Part of this research was also supported by the Environmental Protection Agency under EPA Grant R-805659, and their support is also gratefully acknowledged.

Accession For
NTIS GRA&I
DDC TAB
Unannounced
Justification
By
Distribution/
Availability Codes
Dist | Avail and/or special
A

Table of Contents

The role of diabatic heating in producing mesoscale circulations in a two-dimensional model.

Thomas T. Warner

1. Introduction .
2. Numerical framework of the high-resolution model
3. Sensitivity of mesoscale circulations to the surface, sensible heat flux
   a. Differential heating at a coastline
      1) Coastal-breeze simulation with a specified surface heat flux
      2) Coastline circulation sensitivity studies
   b. Differential heating resulting from inhomogeneous terrain
      1) Mountain-valley breeze simulations with a calculated surface heat flux
      2) Mountain-valley circulation sensitivity studies
   c. Sensitivity of the heat flux to ground characteristics
4. Diurnal oscillation of the planetary boundary layer structure
5. Summary and conclusions

Comparisons of numerical simulations of the planetary boundary layer by a mixed-layer and multilevel model

Richard A. Anthes, Nelson Seaman and Thomas T. Warner

1. Introduction
2. Simulations under horizontally homogeneous conditions
3. Simulation of a sea breeze
4. Simulations over complex terrain and a coastal region
   a. Initialization of mixed-layer model over variable terrain
   b. Multilevel simulation

Table of Contents Cont'd

c. Multilevel and mixed-layer simulations

5. Summary

The Role of Diabatic Heating in Producing Mesoscale Circulations in a Two-Dimensional Model.

Abstract

A two-dimensional, multilevel primitive equation model is used to investigate various characteristics of thermally driven circulations. The sensitivity of the mesoscale circulations to the magnitude of the surface, sensible heat flux is established through examination of various quantifiable circulation features such as the planetary boundary layer depth and the horizontal and vertical wind maxima. The simulations fall into two groups; one deals with circulations over flat terrain in the vicinity of a coastline and the other deals with circulations induced by heating of the irregular terrain in the vicinity of the Tennessee Valley. The results establish a surprisingly linear relationship between forecast errors and errors in the specification of the surface sensible heat flux.

The results of the Tennessee Valley simulations are verified using satellite visible imagery. The model-predicted subsidence over the valley corresponds very closely in location to anomalous cloud-free regions observed in numerous satellite photographs.

1. Introduction

Thermally-driven, mesoscale circulations seldom totally determine the local state of the atmosphere, however their imprint on the large-scale flow is sometimes dramatic and often must be considered when preparing local forecasts or diagnosing the cause of current weather conditions. These circulations, which represent the response of the atmosphere to pressure gradients caused by horizontally differential heating, can result from horizontal variation in terrain elevation or from variation in the thermal characteristics of the earth's surface. The diurnal temperature and wind oscillations not only represent a mechanism for the genesis of mesoscale precipitation producing systems, but also can significantly alter the local air pollution ventilation and transport climatology.

Air pollution dispersion and transport can result from the differential heating along a coastline whether it be of Lake Michigan (Lyons and Olson, 1973; Lyons and Keen, 1976), the San Franscisco Bay (Williams and Demandel, 1966), the Florida Peninsula (Pielke, 1974), the Los Angeles Coastal Plain (Edinger and Helvey, 1961) or the Del.-Mar.-Va. Peninsula (Warner, et al. 1978-a). Anthes (1978) and Warner, et al. (1978-b) have shown, through calculation of parcel trajectories, that thermally driven coastal circulations can produce transport (e.g. of pollution, radioactive debris) over a significant distance during the course of a diurnal heating cycle. Urban heat island circulations can also produce effective atmospheric transport as described by Findlay and Hirt (1969) for Toronto and by Chandler (1965) for London.

Small-scale precipitation can be generated or larger-scale precipitation can be modulated by mesoscale thermal circulation patterns. An analysis of thunderstorm frequency along many land-water boundaries shows a temporal

and spatial maximum related to the convergence zone produced by the sea/lake breeze circulation. Metaxas (1978) has documented this effect in the Mediterranian region while Plank (1960) discussed the convective clouds produced by the sea breeze over the Florida Peninsula. There are also many examples of thermal circulations induced by terrain irregularities producing mesoscale precipitation features. The effects of the thermal circulation are normally not separable from the dynamic effect of the terrain anomaly on the prevailing wind. However, when relatively calm synoptic-scale flow prevails, enhanced convection over higher elevations is commonly observed in satellite photos.

Numerous attempts have been made to simulate these thermally driven circulations using models of widely varying complexity. Venkatesh and Danard (1978) used an economical, one-layer model to simulate lake breeze-related anemometer-level winds and Keyser and Anthes (1977) employed a simple mixed-layer model to predict mesoscale perturbations to flow over heated topography. However, if the three-dimensional wind structure is required for transport calculations or if precipitation predictions are desired, a three-dimensional primitive equation model is necessary.

The following sections will describe model simulations that have been designed to investigate various characteristics of thermally-driven circulations. The model is a two-dimensional, multi-level primitive equation model that can resolve explicitly the details of the lower tropospheric circulations. Details about the structure of the model are provided in section 2.

The sensitivity of the lower-tropospheric, thermally driven circulations to the specification of the thermal forcing at the lower boundary has customarily been ignored in model simulations. Either the models were

used to answer a question in a qualitative sense, in which case the exactness of the surface thermal forcing was not thought to be important, or the forcing was specified to the greatest accuracy possible with no consideration given to the sensitivity of the solution to the level of forcing. In section 3 we describe a series of simulations that will quantitatively relate the response of the model atmosphere to different magnitudes of surface, sensible heat flux. The simulations fall into two groups; one deals with circulations over flat terrain in the vicinity of a coastline, where sensible heating of the atmosphere only occurs over the land, and the other deals with circulations induced by heating of an irregular terrain surface. In both cases, various structural characteristics as well as other quantifiable features of the circulations will be viewed in terms of the linearity of the model atmosphere's response to the amplitude of the diurnal heating function. These results will establish a relationship between forecast errors and errors in the specification of the surface heat flux. For example, if the actual amplitude of the surface heating function is 25% of the solar constant and the modeler errs by allowing a 30% amplitude, a comparison of the results of the simulations using these two amplitudes will indicate the amount of corresponding error produced in the forecast. The surface heat flux is specified in these simulations, and not calculated using a surface energy balance equation, so that the actual heat flux can be incremented from one simulation to the next. These surface heat flux amplitude increments will be translated (section 3.c) into differences in surface albedo, cloud cover, soil moisture etc. The implications of errors in these parameters can thus also be inferred.

The influence of the circulations on the detailed planetary boundary layer structure is of practical interest. The ability of the atmosphere to

disperse particulates and gases emitted from sources at the lower boundary depends on the wind and temperature structure of the planetary boundary layer. This structure depends in turn on dynamic and thermodynamic effects of differential heating. In section 4 we will follow the transition of the wind and temperature structure at various points within the coastal and mountain-valley circulations.

2. Numerical framework of the high-resolution model

The high-resolution, two-dimensional model is described in complete detail by Anthes and Warner (1978) and will be summarized here. It is based on the primitive equations of motion and is hydrostatic, where the number of vertical levels and horizontal grid points is arbitrary and is only dependent on the simulation requirements and available computer time and storage. The model's vertical coordinate is σ defined by

$$\sigma = \frac{P-P_t}{P_*-P_t} \tag{2.1}$$

where P_* is the surface pressure and P_t is the pressure of the upper boundary of the model. The horizontal and vertical grid structure is staggered. Space differencing is centered while the time differencing follows the technique of Brown and Campana (1978).

The fluxes of heat and momentum in the planetary boundary layer (PBL) are calculated according to Busch et al. (1976) and are based on a time dependent mixing length computed at various levels within the PBL. Model layers are relatively shallow (about 250 m deep) within the lowest 2 km, so that the PBL structure can be explicitly resolved. The temperature of the earth's surface is a requirement of the PBL model and is normally computed based on a prognostic model developed by Blackadar (1978). The prediction is based on the state of the ground surface (e.g., wetness, roughness,

albedo) and the relevant astronomical parameters such as latitude, longitude and the time of year. An alternative approach is to specify the surface heat flux instead of calculating it using the computed ground temperature. Both procedures will be used in simulations discussed in this report.

The lateral boundary conditions imposed on the dependent variables are open. Momentum values at the boundary points are forecast based on a specified advective change and a change based on the computed boundary layer flux convergence of momentum. Temperatures at the lateral boundaries are assumed to change only as a result of the vertical flux convergence of heat. The surface pressure at the boundary is set equal to the value of the first interior point. These boundary conditions allow gravity-wave energy to propagate out of the domain while providing for the forecasting of diurnal PBL wind and temperature profiles at the boundary points.

3. Sensitivity of mesoscale circulations to the surface, sensible heat flux

a. Differential heating at a coastline

In order to determine how sensitive the various characteristics of the coastal circulation are to the intensity of the surface heat flux, a series of six experiments has been performed. The surface, sensible heat flux over land was specified according to

$$H = H_o \sin\left(\frac{2\pi t}{24}\right) \qquad (3.1)$$

where H is the time-dependent heat flux, H_o is the amplitude of the heating function and t is the time elapsed from the beginning of the heating period. The duration of the six simulations is 12 h, which is the length of the imposed heating cycle. Surface sensible heat fluxes over water were assumed to be zero. The six cases differed according to the amplitude of the heating function H_o. Experiments one through six correspond to values of H_o

ranging from 15% of the solar constant to 40% of the solar constant respectively, at intervals of 5%. Other model characteristics are summarized in Table 1.

Table 1

Summary of Coastline Experiment Characteristics

P_{top} = 250 mb

ΔX_{min} = 10 km; Δt = 23 s

Latitude = 35°

Number of grid points = 31

Number of levels = 12

Land grid-point numbers (left to right) = 1 to 21

The grid was telescoped such that the grid interval at the boundaries was $8\Delta X_{min}$ and decreased to $4\Delta X_{min}$ and $2\Delta X_{min}$ for the second and third intervals from the boundary respectively. For the remaining grid intervals, the distance was 10 km. The top boundary of the model corresponded to the 250 mb isobaric surface.

The wind components at the beginning of the forecast were specified as zero and the temperature profile, as illustrated in Fig. 1, corresponded to the standard atmosphere for mid-latitudes.

1) COASTAL-BREEZE SIMULATION WITH A SPECIFIED SURFACE HEAT FLUX

Before discussing the sensitivity of different aspects of coastal circulations to the surface, sensible heat flux, we will examine the details of one of the simulations - specifically, the one having a surface heat flux amplitude of 25% of the solar constant. Fig. 2 depicts the velocity component in the plane of the cross-section after 6 and 12 h of simulation time. The heavy line represents the model-predicted depth of the planetary

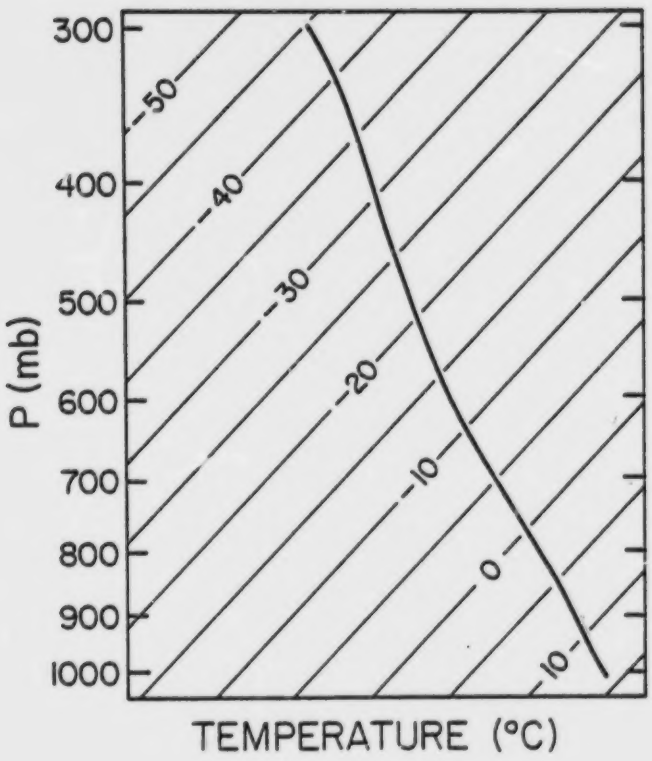

Fig. 1. Temperature profile used as initial conditions for the coastline and mountain-valley circulation experiments.

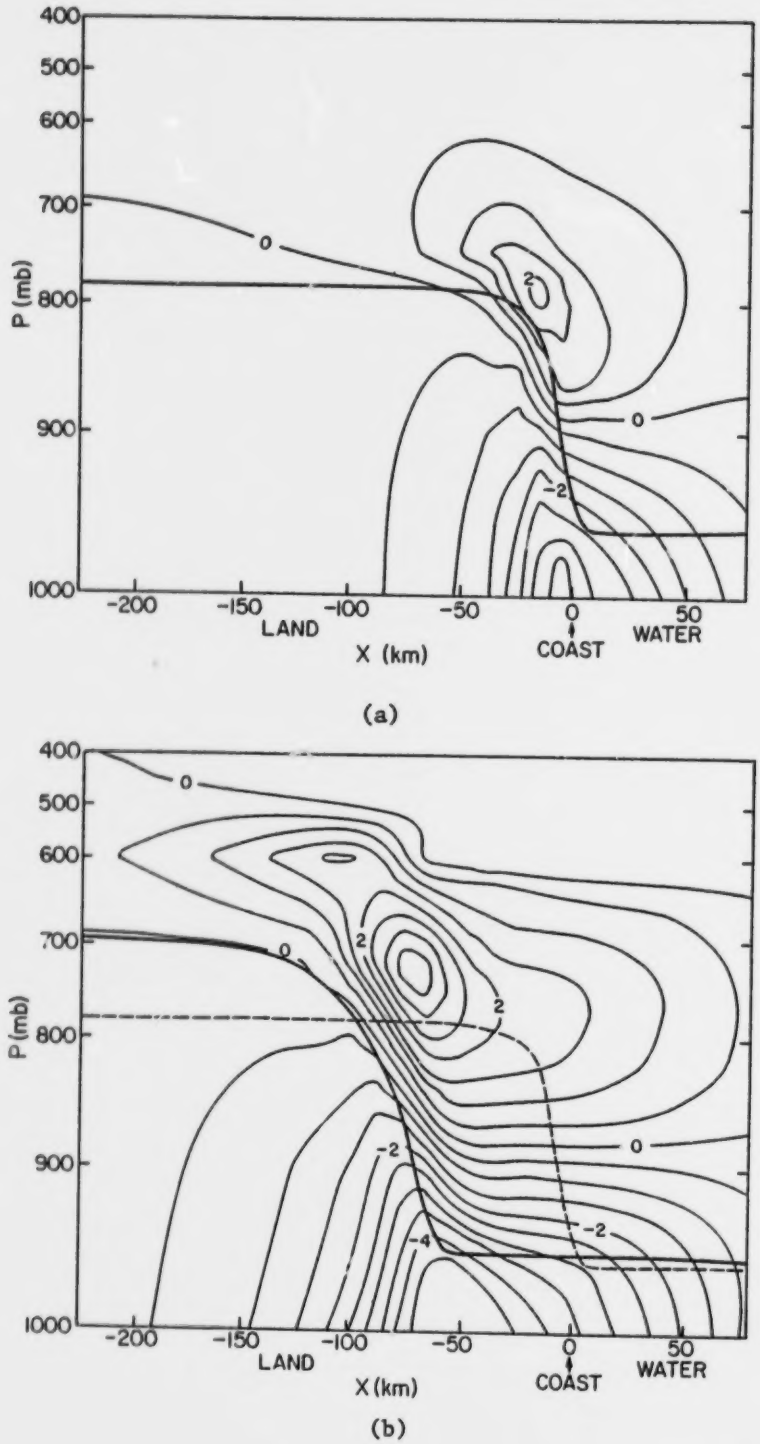

Fig. 2. Coastline simulation after 6h (a) and 12h (b) where the heat-flux amplitude was 25% of the solar constant. Contours are of the velocity component in the plane of the cross section. The heavy line represents the top of the predicted PBL. The dashed line in (b) shows the 6h predicted PBL top.

boundary layer (PBL). After 6 h of heating, the onshore branch of the circulation shows a speed maximum of 3.50 m s^{-1} at grid point 21 of the lowest computational level located at about 80 m above the surface. The offshore, upper branch shows a maximum speed of 2.14 m s^{-1} about 10 km inland of the maximum in the onshore component and at an elevation of about 2 km. The PBL at 6 h exhibits an abrupt change in height at the coastline, the inland values being approximately 2 km above the surface. After 12 h, the onshore flow maximum has reached 5.1 m s^{-1} and moved inland to grid point 17, a distance of 45 km from the coastline. The offshore flow maximum is 3.75 m s^{-1} and is located 25 km to the west of the onshore maximum and at a height of about 3 km. At both 6 h and 12 h, the zero isotach, separating the onshore and offshore flow regimes, corresponds closely with the top of the PBL over land. Over water the PBL depth remains relatively constant. The greatest change in the PBL depth that occurs between 6 and 12 h is found along the coastline, even though it has risen at inland locations by about 1 km during this period. The dotted line in Fig. 2b represent the PBL top at 6 h. Note that advection of cool, low-level, maritime air by the lower branch of the circulation has stabilized the lowest 100 mb of the atmosphere for a distance of 50 km inland from the coastline, and caused an "erosion" of the PBL depth in this region.

Fig. 3 illustrates the vertical motion patterns at 6 and 12 h. The 6 h vertical motion field illustrates the existence of two narrow zones of relatively large vertical velocities, where less than 10 km horizontal distance separates the maxima of upward and downward motion. The upward motion maximum is about 15 km inland of the coastline. The maximum downward vertical velocity is situated about one kilometer above the maximum in the upward motion. The slope of the zero isotach of the vertical motion field is of the order of 1 to 10 with the tendency for the slope to become less as this

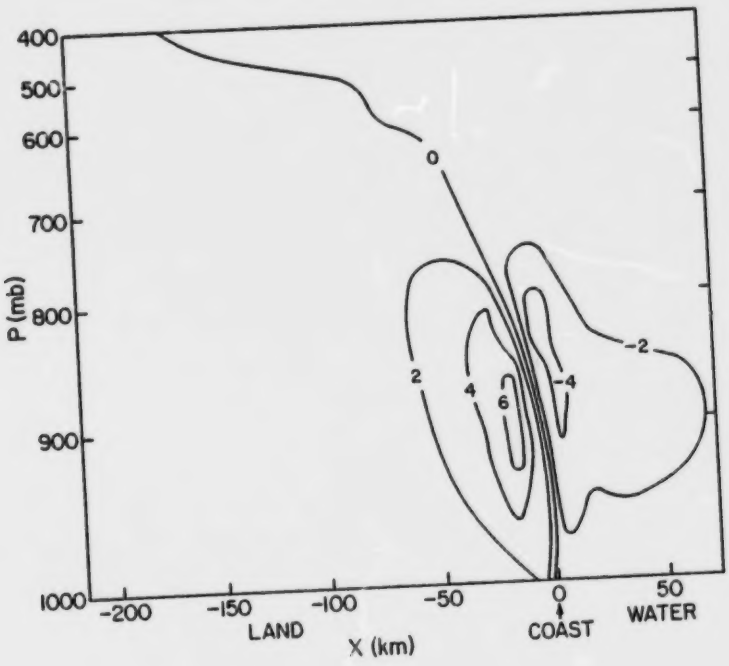

(a)

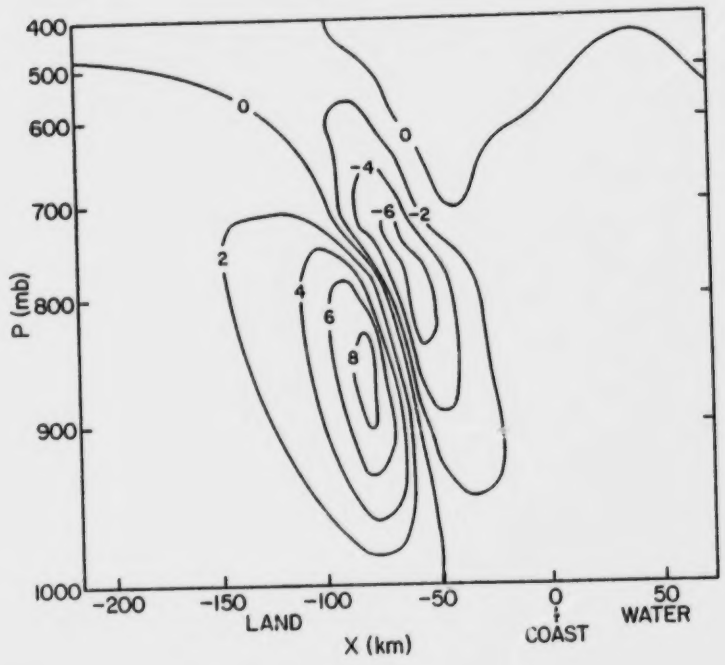

(b)

Fig. 3. Vertical motion associated with the coastline simulation after 6h (a) and 12h (b) where the heat-flux amplitude was 25% of the solar constant. Contours are labeled in cm s^{-1}.

isotach rises and tilts inland. The upward motion maximum is approximately 7 cm s^{-1} whereas the downward motion maximum reflects a speed of about 5 cm s^{-1}. The 12 h configuration is qualitatively similar to that at 6 h. The upward motion maximum, now having a value of about 9 cm s^{-1}, is 75 km from the coastline. The downward motion maximum is still displaced upwards and toward the coastline and has a value of about 7 cm s^{-1}. Again, there is a strong shear zone of vertical motion with no more than 20 km horizontal distance separating the two maxima. Note that these vertical velocities correspond to 10 km averages. In reality, ascent along the sea-breeze front often occurs on much smaller scales (1 km) and is therefore much larger at a given point than these values.

Fig. 4 illustrates the integrated effect of the temperature changes that occurred during the 12 h simulation. The cooler, maritime air has penetrated inland over a large distance as indicated by the temperature gradient near the surface between - 100 and - 150 km on shore. The maximum in the temperature change over water resulted from the integrated effect of the subsidence that prevailed over the water for the duration of the forecast.

2) COASTLINE CIRCULATION SENSITIVITY STUDIES

We will now consider a variety of properties of the coastal circulations and how their qualitative and quantitative natures depend on the surface, sensible heat flux: (1) the location of the coastal-breeze front, (2) the pressure gradients produced by the differential heating, (3) the location of the upward motion maximum, (4) the location of the zero isotach separating the onshore flow from the offshore flow, (5) the location of the onshore and offshore wind maxima, and (6) the PBL depth.

The extent of the inland penetration of the coastal-breeze front is defined in this paper by the integrated temperature changes. The point at

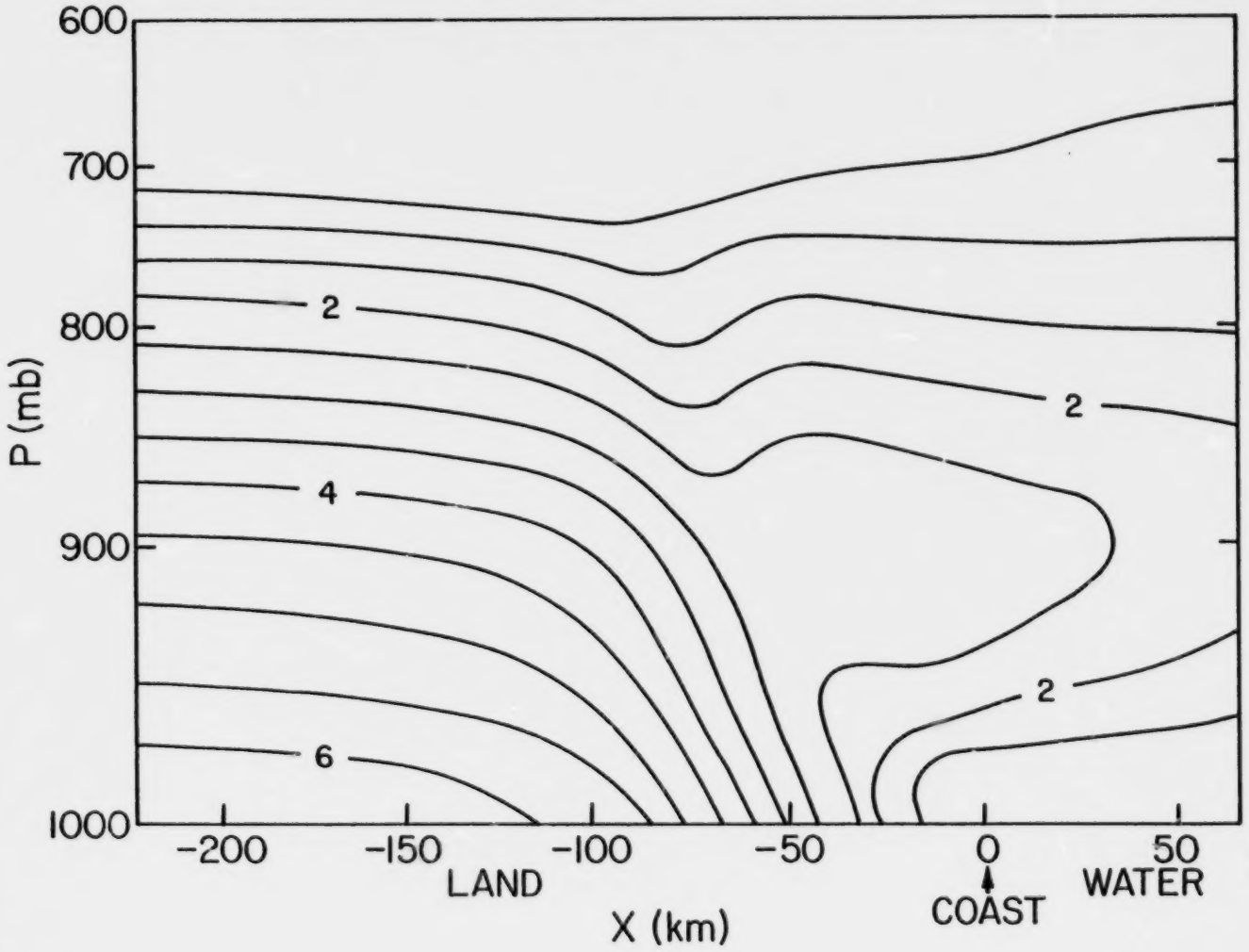

Fig. 4. Temperature change during the 12h coastline simulation where the heat-flux amplitude was 25% of the solar constant.

which the maritime-air advection has suppressed the temperature rise in the lowest model layer by greater than 0.1°C is defined as the near-ground-level location of the front. Because the winds that effect the inland advection of the maritime air are driven by the pressure gradient that results ultimately from the contrast in surface, sensible heat flux, we would expect to see a relationship between frontal displacement from the shoreline and the amplitude of the heating function. Fig. 5 illustrates the frontal displacement from the shoreline as a function of time within the 12 h heating cycle, for heating function amplitudes of 15%, 25%, and 35% of the solar constant. The frontal position differs by about 50 km between the two extremes in the value of H_o. The relationship between frontal displacement and surface sensible heat flux seems to be approximately linear, at least within this range of heat flux values. Fig. 6 gives the detailed temperature changes as a function of space and time at the lowest model computation level for the same three surface heat flux amplitudes. The circled points correspond to the diagnosed locations of the coastal-breeze front for that particular time. The three graphs show qualitatively the same behavior of the temperature. The greatest low-level temperature increase occurs at inland locations, beyond the "reach" of the coastal-front, while the most rapid increase in temperature occurs during the first 6 h of the heating cycle. Locations behind the front not only show a lower rate of temperature increase with time, but experience a temperature change reversal when the effect of the cold advection exceeds the diabatic heating effect. For example, when H was 35% of the solar constant (Fig. 6c), the point 25 km inland of the coastline experienced a temperature rise to the 6 h point in the heating cycle, after which the temperature decreased for the remainder of the simulation. It is also worth noting than an isentropic analysis of the results shows the vertical slope of the coastal-front to

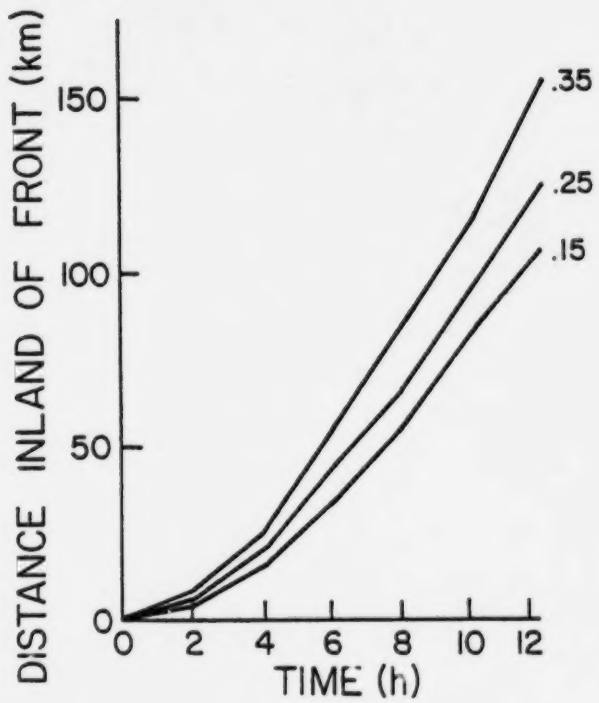

Fig. 5. Frontal displacement from the shoreline as a function of time within the 12h heating cycle, for heating function amplitudes of 15%, 25% and 35% of the solar constant.

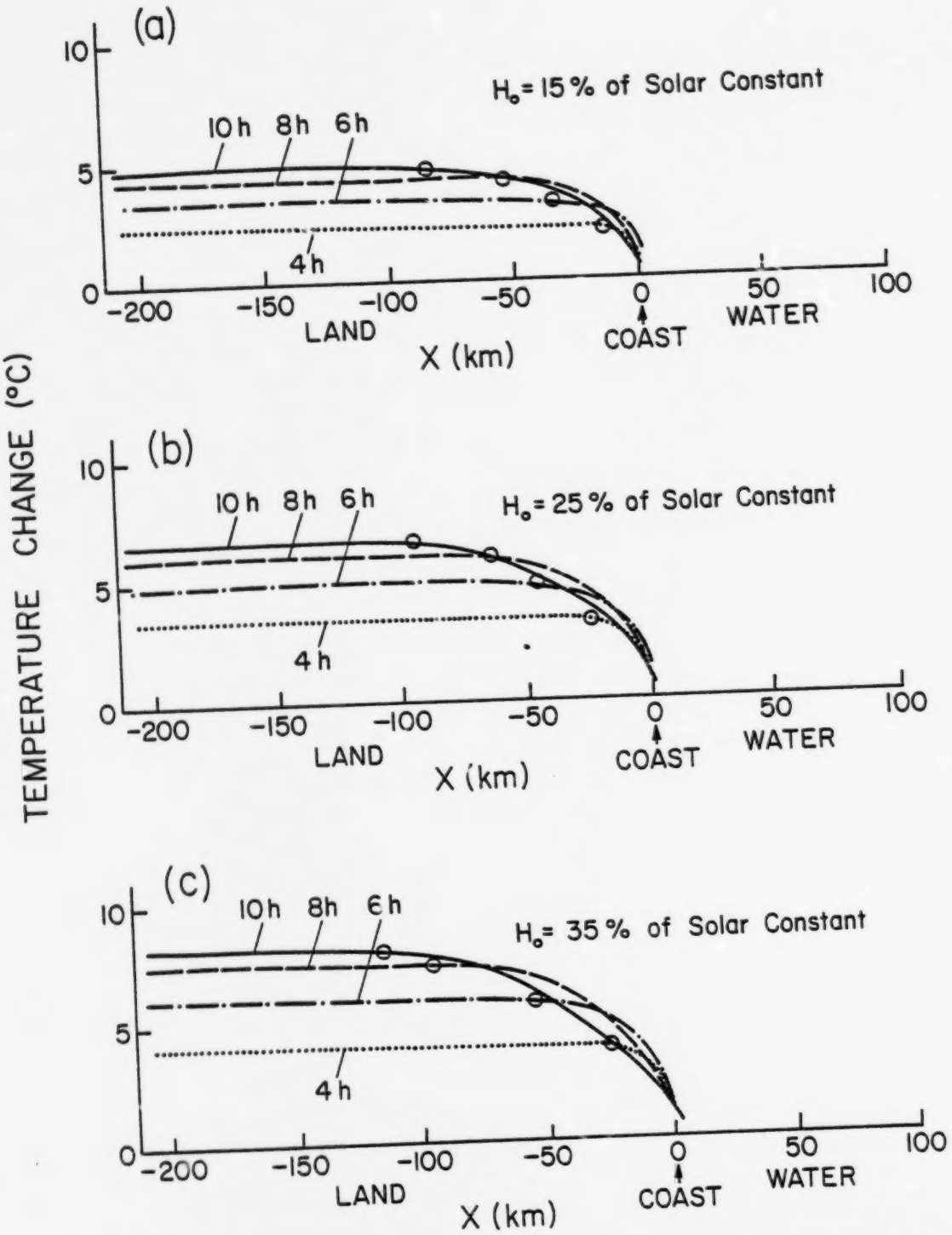

Fig. 6. Temperature change as a function of time and distance from the coastline, at the lowest model computation level for heat flux amplitudes of 15%, 25% and 35% of the solar constant.

be approximately .2, considerably more steep than a synoptic-scale cold front.

The amplitude of the pressure changes that drive the coastal circulation is also a function of the surface, sensible heat flux. Fig. 7 shows the surface pressure field at three times in the heating cycle for three different heating function amplitudes. The pressure change at points over water and over land is about 1 mb with increases over water and decreases over the land. The pressure gradient is initially confined to the coastline where the temperature gradient first appears. As cool maritime air is advected inland, producing a broader region where the temperature gradient exists, the pressure gradient decreases in magnitude and extends further inland. For larger, surface, sensible heat fluxes, the amplitude of the pressure change increases as does the inland penetration of the pressure gradient. This of course parallels the penetration inland of the winds and temperature gradient. Fig. 8 compares the 8 h pressure fields for the six experiments. The dominant effect of the surface heat flux is on the amplitude of the pressure change. The character of the wave is relatively unchanged in that the strongest pressure gradient remains within 50 km of the coastline.

Fig. 9 shows the transition undergone by the upward-motion maximum associated with the coastal-breeze front, in terms of the value of the maximum as well as its position relative to the coastline. Graphs are plotted for surface sensible heat fluxes equal to 15%, 25%, and 35% of the solar constant. The time since the start of the heating cycle is shown at 2, 4, 6, 8, 10 and 12 h for each plot. Several trends are evident. First, the upward-motion maximum moves inland at about the speed of the coastal-breeze front, with a positive acceleration during the heating cycle.

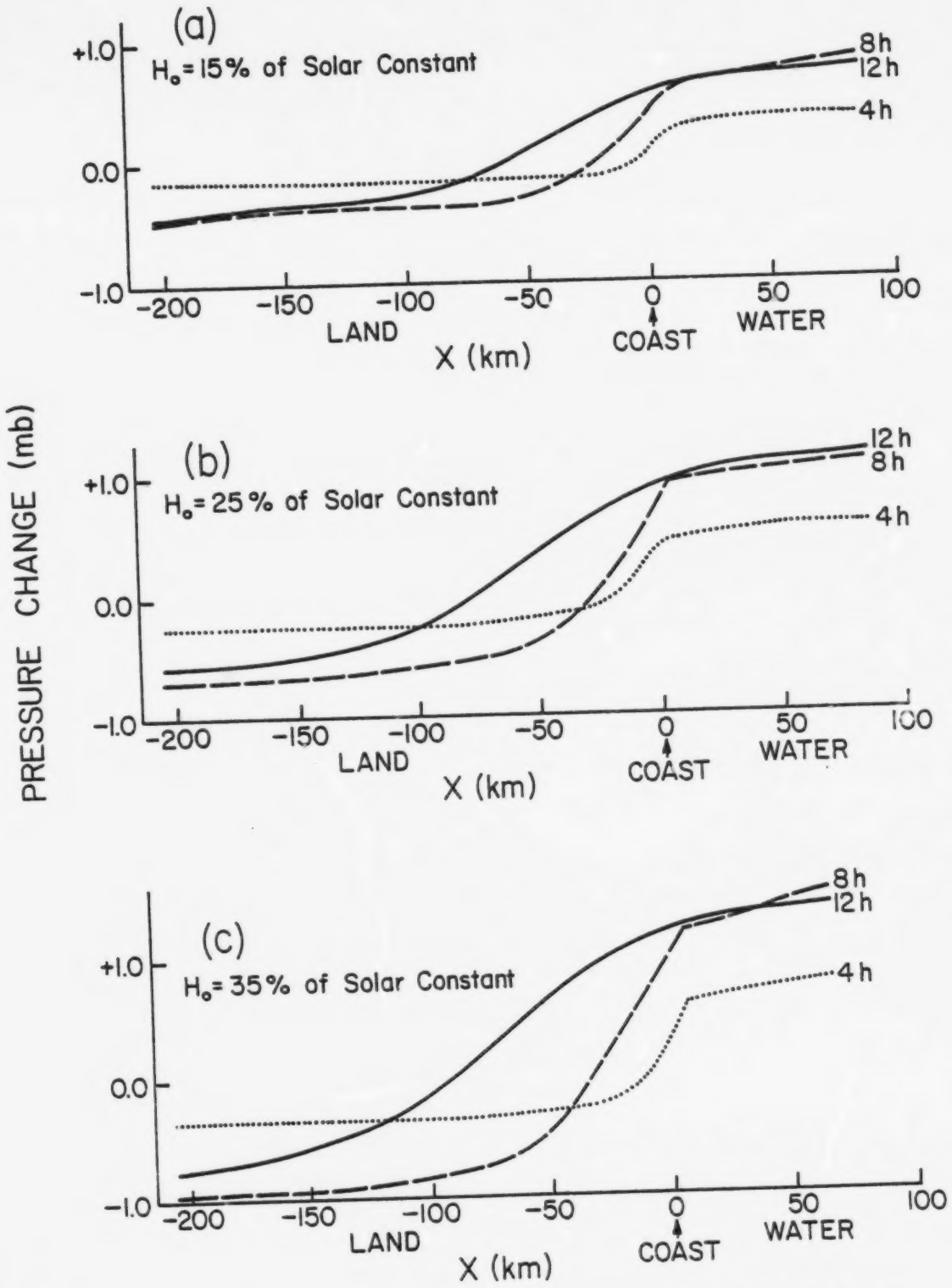

Fig. 7. Surface pressure change as a function of time and distance from the coastline for various heat flux amplitudes.

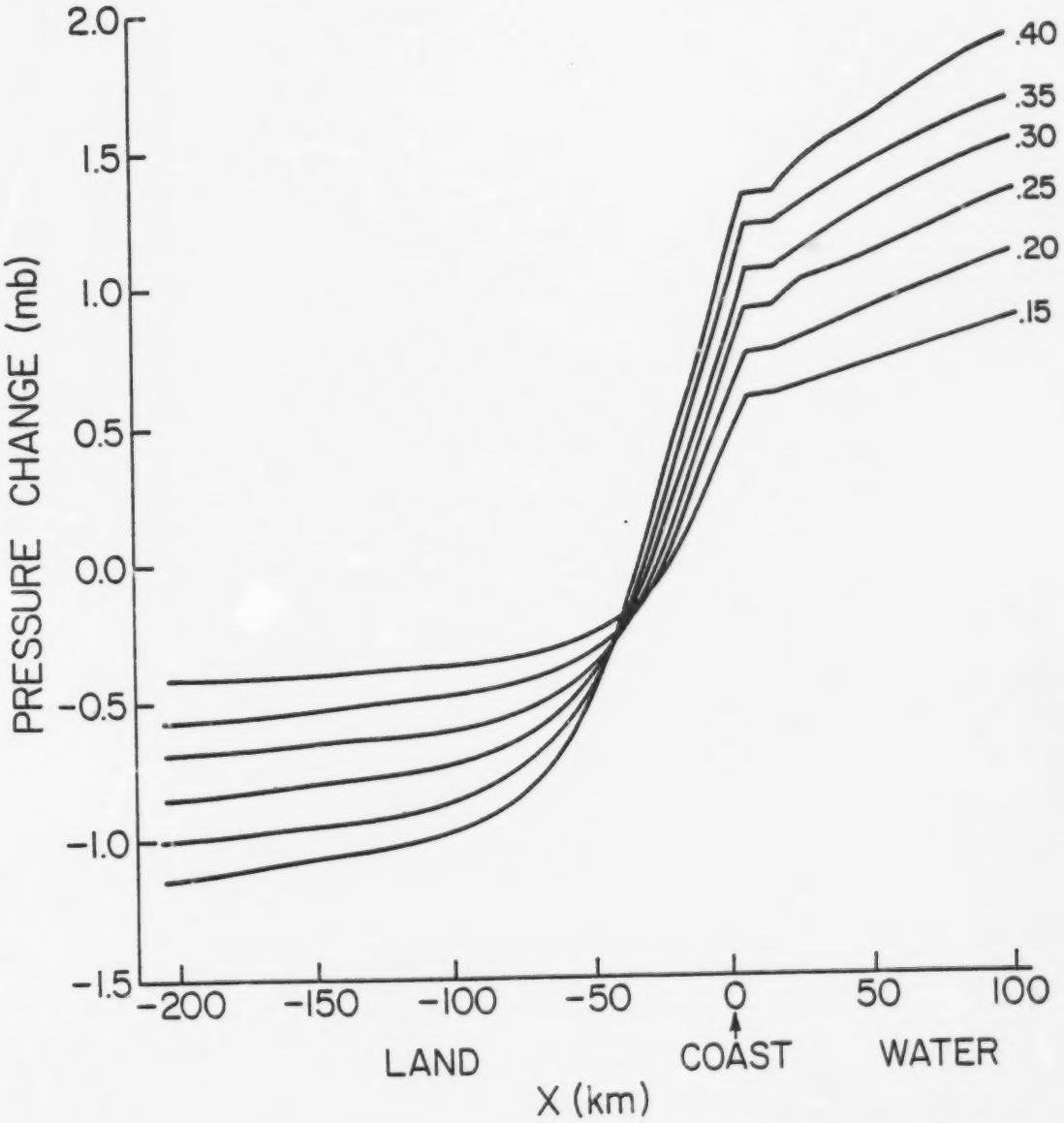

Fig. 8. Surface pressure change as a function of distance from the coastline, after 8h of the heating cycle for various amplitudes of the heating function.

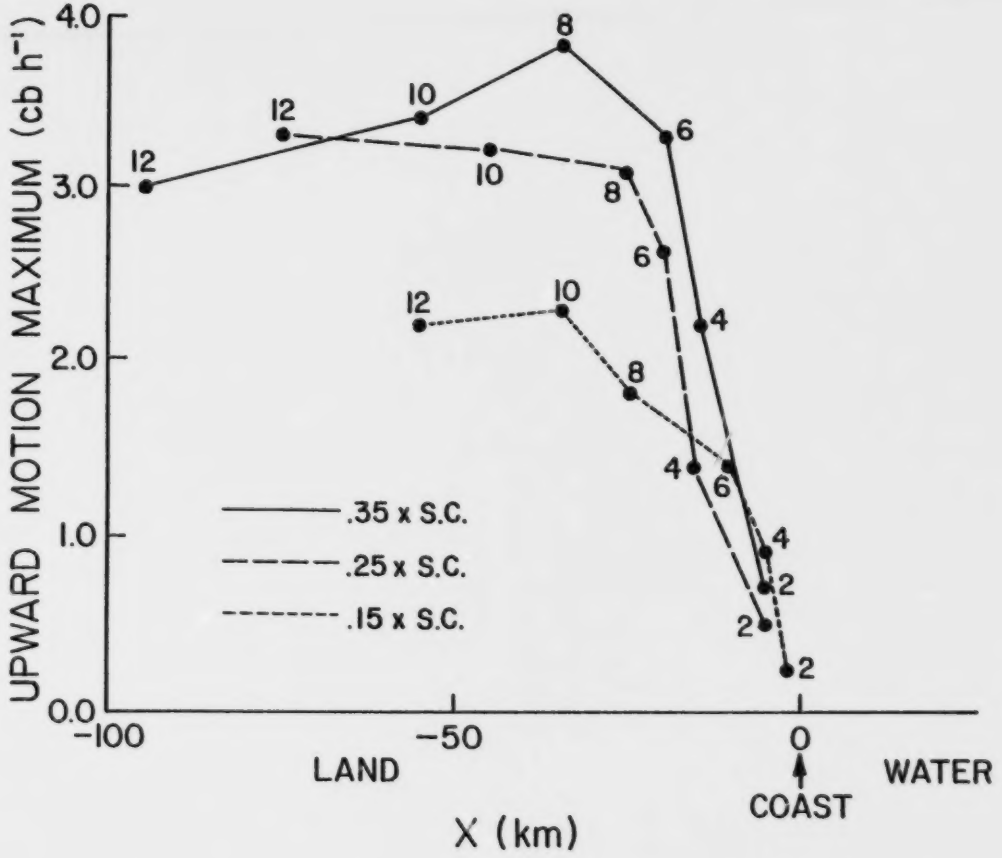

Fig. 9. Horizontal position and intensity of the upward motion maximum associated with the sea-breeze front for heatinf function amplitudes of 15%, 25% and 35% of the solar constant. The ordinate is labeled in terms of the intensity of the upward motion and the numbers associated with the dots on the curves correspond to the time in hours within the 12h period of the simulation.

This acceleration can also be seen in Fig. 5 by noting the increase of the slope with time of the curve depicting frontal displacement as a function of time. Secondly, the magnitude of the upward motion maximum increases most rapidly during the first 6 to 8 h of the heating cycle. For the higher heating rates, even a slight decrease is noted after 8 h. It should be kept in mind that the maximum vertical velocity is almost certainly underestimated by the model because of the relatively coarse grid mesh.

An aspect of the circulation that has important air pollution transport implications is the separation between the onshore and offshore flow regimes. Depending on the spatial relationship between the height at which pollution is inserted into the atmosphere (e.g., the effective stack height) and the height of the zero isotach of the horizontal motion, the effluent may be transported either landward or seaward. It has been noted earlier that, over land, this isotach is normally located at about the same elevation as the top of the PBL. Fig. 10 illustrates the dependence of the height of this zero isotach, that separates the two flow regimes, on the surface sensible heat flux. The plot applies 8 h after the beginning of the heating cycle. For larger heating rates, this line of separation is more elevated as is the top of the PBL. The differences in elevation among the lines for the different heating rates however is generally less than 25% of the total distance of the line from the ground level. For a doubling of the surface heat flux amplitude from 15% to 30% of the solar constant, the change in elevation during the heating cycle was always less than 500 m where the total distance above the surface was over 2000 m for large distances inland. To visualize the transition of this line during the heating cycle, we can examine Fig. 11. Figs. 11a and b are x - p plots of this line at 2 h intervals from 4 to 12 h into the heating cycle for surface heat flux amplitudes of 15% and 40% of the solar constant, respectively. The temporal transition of this line is complicated but a pattern to the transition is common for all the surface heat-flux amplitudes. The zero isotach is relatively high early in the integration, but during the heating

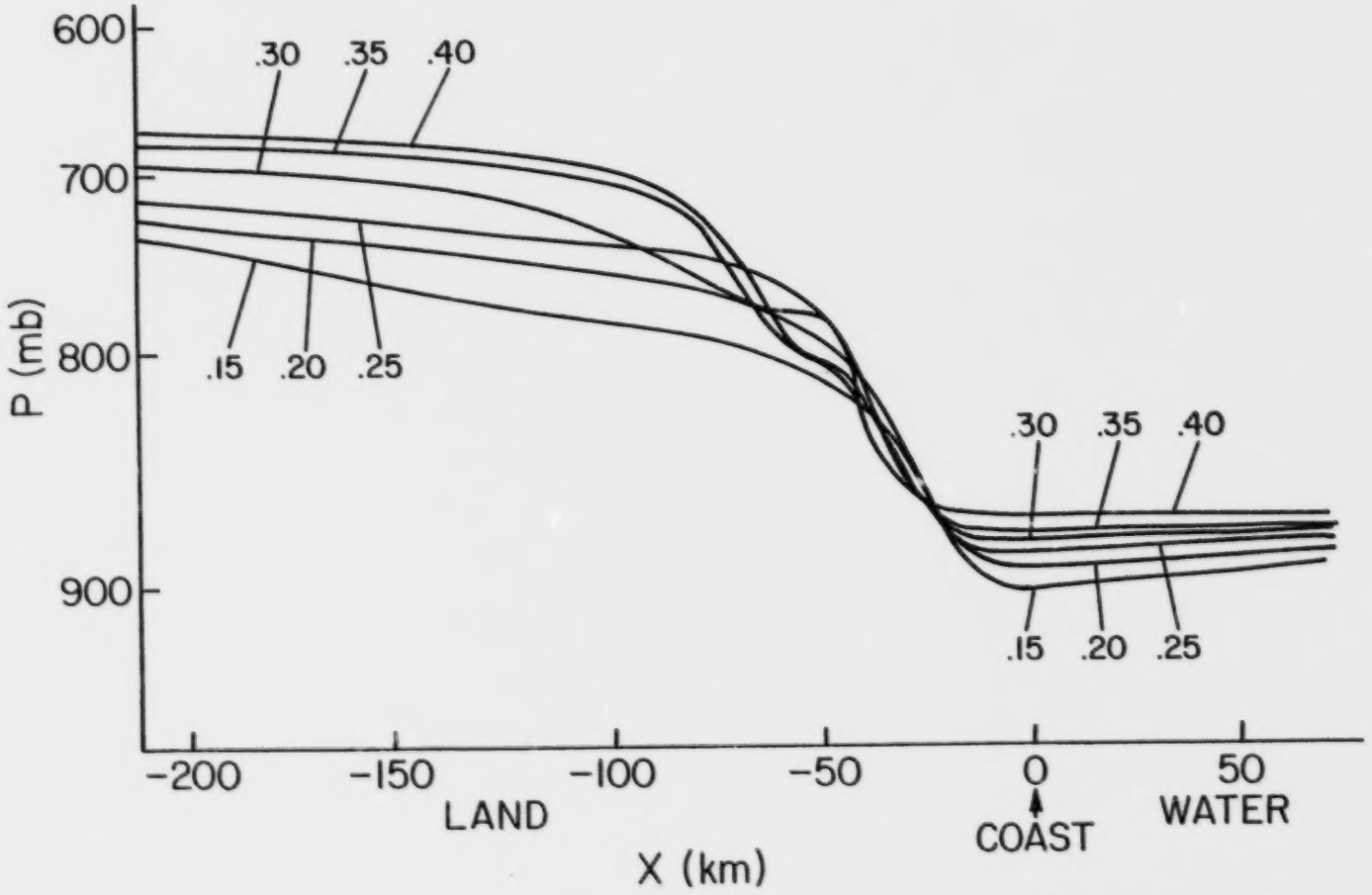

Fig. 10. Height of the isotach of zero horizontal motion after 8h of simulation for various heating function amplitudes. The curves are labeled in terms of the amplitudes of the heating function expressed as a fraction of the solar constant.

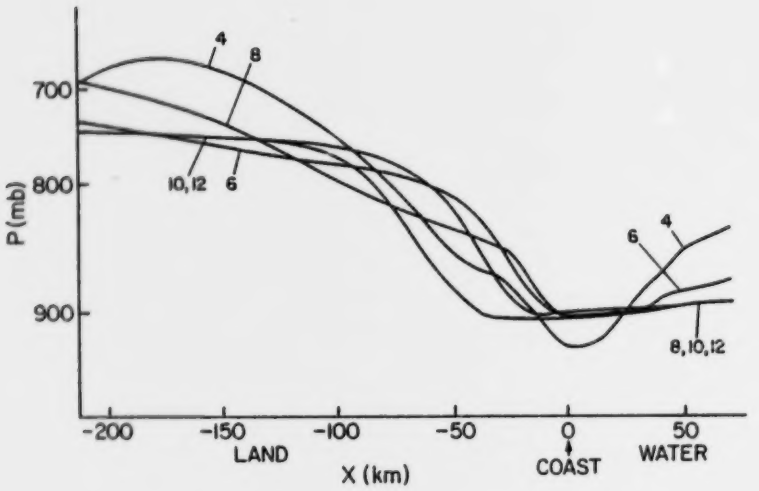

(a)

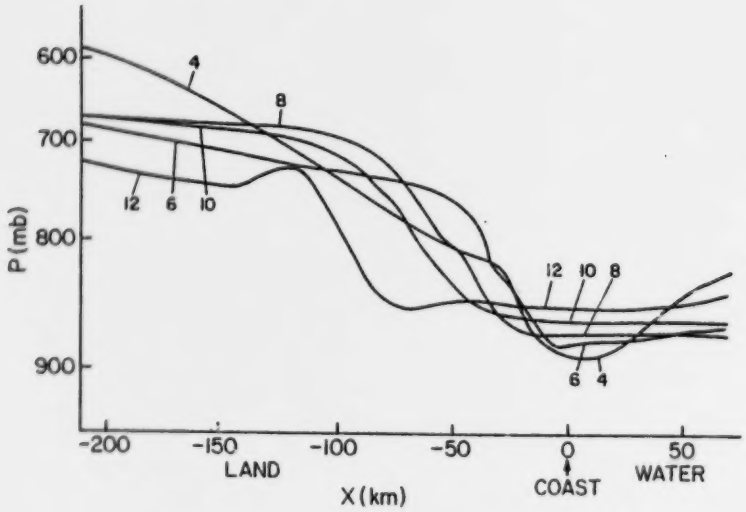

(b)

Fig. 11. Height of the isotach of zero horizontal motion for various times (h) within the heating cycle where the amplitude of the heating function was 15% (a) and 40% (b) of the solar constant.

cycle it decends over land and water in an irregular manner. At the end of the heating cycle it is located about 500 to 1000 m below its original position. The observation here and by Anthes (1978) that this level of wind reversal is generally coincident with the top of the PBL over land is only correct for times late in the heating cycle and does not imply the existence of any strong physical relationship. It should not be surprising that the zero isotach first appears at a high elevation because the horizontal pressure gradient that is produced by the differential heating appears first aloft, with the acceleration toward the water increasing in magnitude with height.

The greatest change in elevation of the zero isotach during the heating cycle occurs within 50 to 100 km of the coastline. A 1 km deep layer, which extends this distance inland from the coastline, experiences complex reversals in the wind direction during the heating cycle.

So that the different, important aspects of the circulation that were enumerated earlier can be interpreted as a whole and so that the complicated temporal and spatial relationships among them can be better understood, we will examine Figs. 12a - e which, in an x - p cross-section, depict all of the important characteristics of the circulation at 2 h intervals from 4 h to 12 h for the experiment having a surface heat-flux amplitude of 25% of the solar constant. As the heating cycle progresses, a persistent relationship between the PBL depth over land and the circulation characteristics is observed. The center of the circulation and the locations of the horizontal and vertical wind speed maxima all maintain a characteristic spatial relationship to the PBL structure. The downward motion maximum is above the PBL while the upward motion maximum is within it. The horizontal wind maximum directed toward the water is consistently above the steepest slope of the PBL; both move inland at approximately the same rate during the

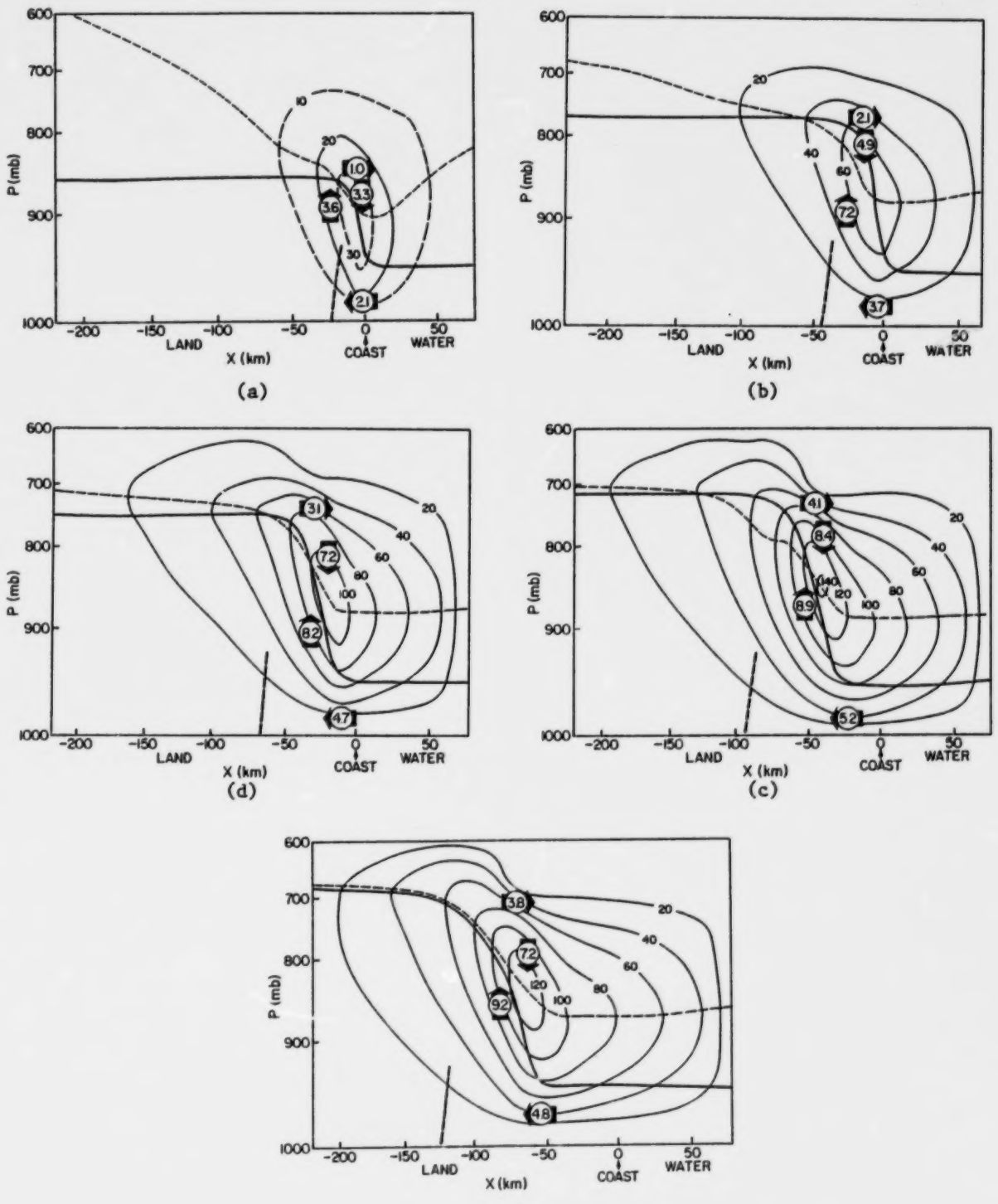

Fig. 12. Characteristics of the coastal circulation after 4h (a), 6h (b), 8h (c), 10h (d) and 12h (e) where the amplitude of the heating function was 25% of the solar constant. The solid line is the top of the PBL, the unlabeled dashed line aloft is the zero isotach of horizontal motion, the concentric lines are the streamfunction, the horizontal arrows indicate the maxima in the onshore and offshore flow and are labeled in m s^{-1}, the vertical arrows indicate the maxima in the vertical motion field and are labeled in cm s^{-1} and the dashed line intersecting the surface is the coastal-breeze front. All velocity maxima given to nearest tenth.

heating cycle.

Figs. 13a - c illustrate these same characteristics applying at the end of the heating cycle for heating function amplitudes of 15%, 25% and 35% of the solar constant, respectively. The spatial relationships among the different features that characterize the circulation, such as the PBL depth, the streamline pattern and the location of the coastal front, do not differ between the high and low heat flux amplitude experiments. The center of the circulation is above the top of the PBL, between the coast and the leading edge of the maritime air being advected inland from the coastline. It has an elevation approximately halfway between that of the top of the PBL over the water and that over land, and is about half the distance inland of the coastal-breeze front. The basic geometric characteristics of the circulation are, therefore, not functions of the amplitude of the surface heating function.

b. Differential heating resulting from inhomogeneous terrain

Another common mechanism by which thermally driven circulations can be generated is through the existence of terrain elevation maxima, which represent elevated heat sources during daylight hours. Sensitivity experiments were conducted, employing the same six heating function amplitudes as before, with a real terrain profile. The terrain profile represents an east-west transect of the Appalachian Mountains, located and oriented in such a way that the Tennessee River Valley is well defined. Fig. 14 shows the terrain profile used. The main Appalachian Ridge to the east of the Tennessee Valley reaches a maximum elevation of 930 m above the valley level whereas the low mountains, defining the western edge of the valley, reach an elevation of 320 m above the valley level.

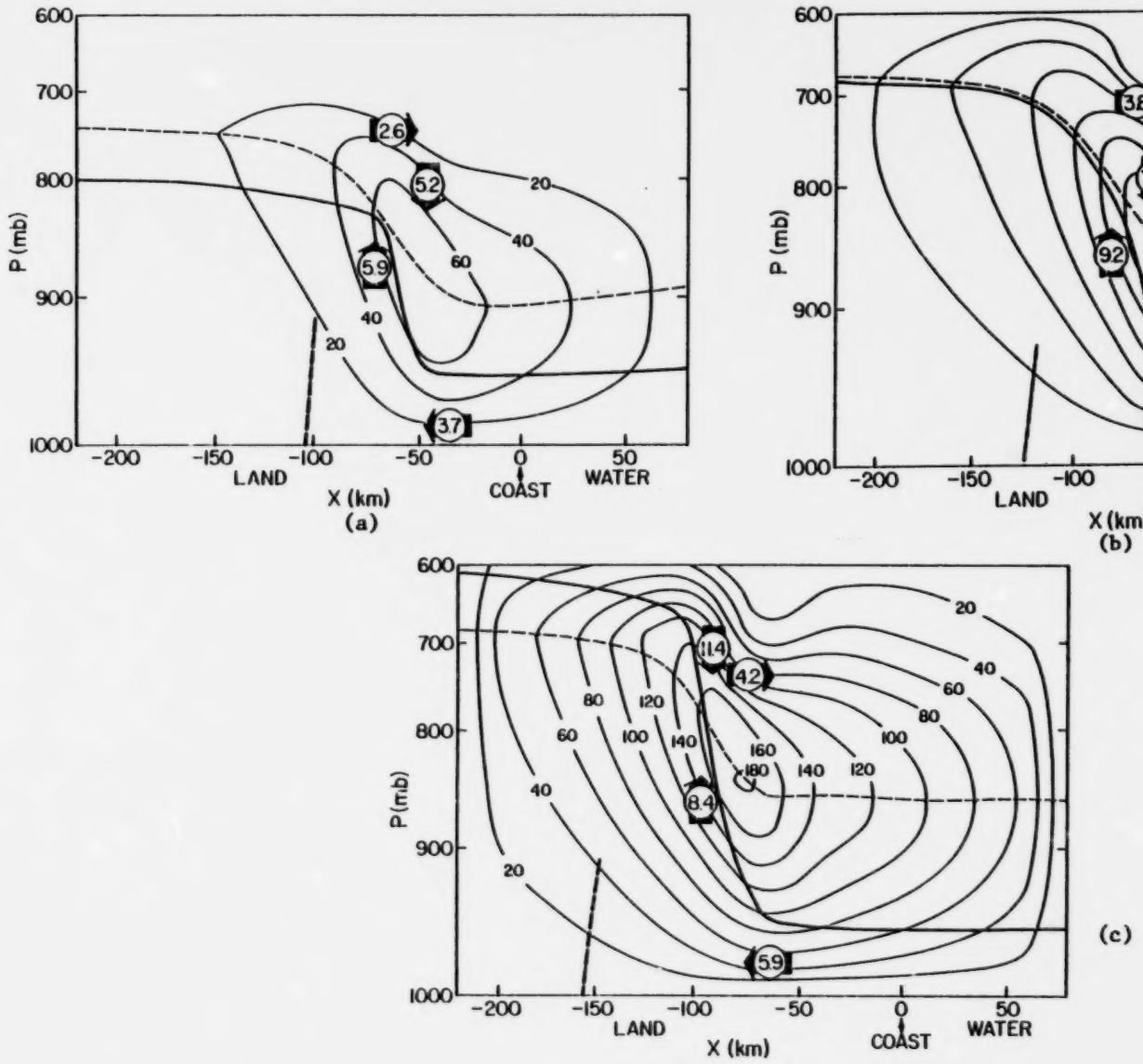

Fig. 13. Characteristics of the coastal circulation after 12h for heating function amplitudes of 15% (a), 25% (b) and 35% (c) of the solar constant. The solid line is the top of the PBL, the dashed line aloft is the zero isotach of horizontal motion, the concentric lines are the streamfunction, the horizontal arrows indicate the maxima in the onshore and offshore flow and are labeled in m s^{-1}, the vertical arrows indicate the maxima in the vertical motion field and are labeled in cm s^{-1} and the dashed line intersecting the surface is the coastal-breeze front.

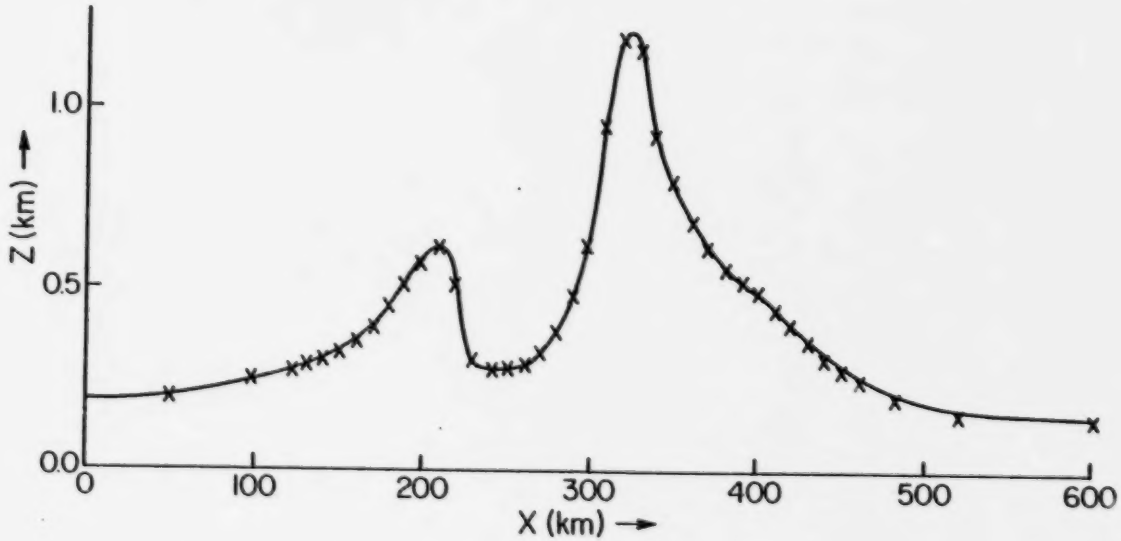

Fig. 14. Terrain profile along a northwest-southeast transect of the Tennessee Valley and Appalachian Mountain Range. The cross marks show the positions of model grid points.

1) MOUNTAIN-VALLEY BREEZE SIMULATIONS WITH A CALCULATED SURFACE HEAT FLUX

Before the sensitivity experiments were conducted using the specified, surface sensible heat flux, a number of simulations were performed with a version of the model employing the surface energy balance equation of Blackadar (1978). This allowed a realistic in-model calculation of the surface sensible heat flux. These simulations were used to better understand and define the nature of the circulation patterns before the sensitivity studies were conducted. Characteristics of the model structure that are common among all the preliminary experiments are summarized in Table 2. Differences among the experiments are tabulated in Table 3.

Table 2

Summary of Model Characteristics Common to the Preliminary Tennessee Valley Simulations

P_{top} = 200 mb

ΔX_{min} = 10 km

Latitude = 35°N

Number of grid points = 41

Number of model levels = 12

Initial local-apparent time = 0439 L.A.T.

Forecast duration = 12 h

Surface Albedo = 0.2

Soil heat capacity per unit volume = 1.07×10^{6} J m^{-3} K^{-1}

Soil thermal conductivity = 0.5 J m^{-1} s^{-1} K^{-1}

Initial winds = calm

Initial temperature structure = U.S. Standard Atmosphere

Because the chosen, observed topography is very complex, it is advisable to first test the dynamic response of the model atmosphere to forcing by a smooth, synthetic terrain profile. Fig. 15 illustrates this terrain and the vertical motion ($\omega = \frac{dp}{dt}$) pattern after 2 h and 6 h as forced by this upper level heat source (simulation P1).

Table 3

Preliminary Tennessee Valley Simulations - Specific Differences

Simulation	Solar Forcing	Terrain
P1	appropriate for 23 June*	idealized simple ridge
P2	appropriate for 23 June*	observed
P3	appropriate for 1 April†	observed
P4	appropriate for 23 June*	observed except that east ridge removed
P5	appropriate for 23 June*	observed except that west ridge removed

*sunrise = 0447 L.A.T. at 35° Lat.

†sunrise = 0548 L.A.T. at 35° Lat.

After 2 h, the deep upward motion is initially confined to the atmosphere immediately above the ridge top. Upward motion also exists in a shallow layer along the sides of the ridge. The subsidence of the return circulation has two maxima located at a distance of about 100 km from the center of the ridge. After 6 h of simulation, the upward vertical motion above the ridge has divided into 3 maxima; one over the ridge top

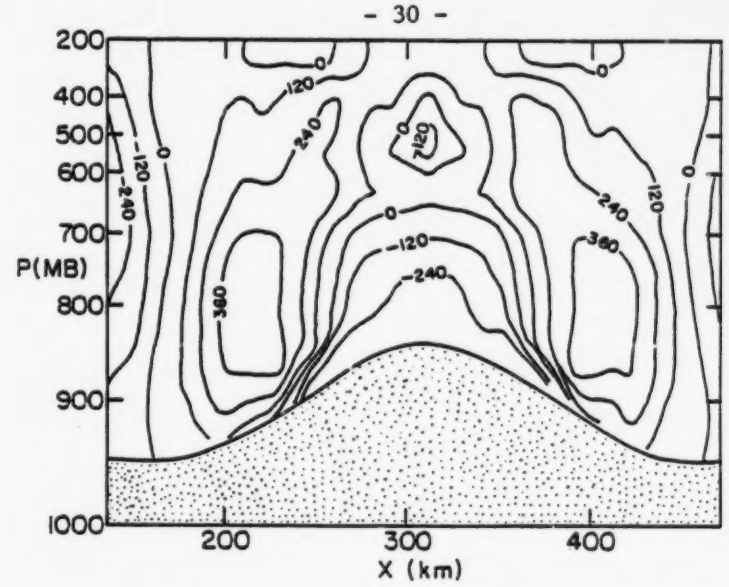

(a)

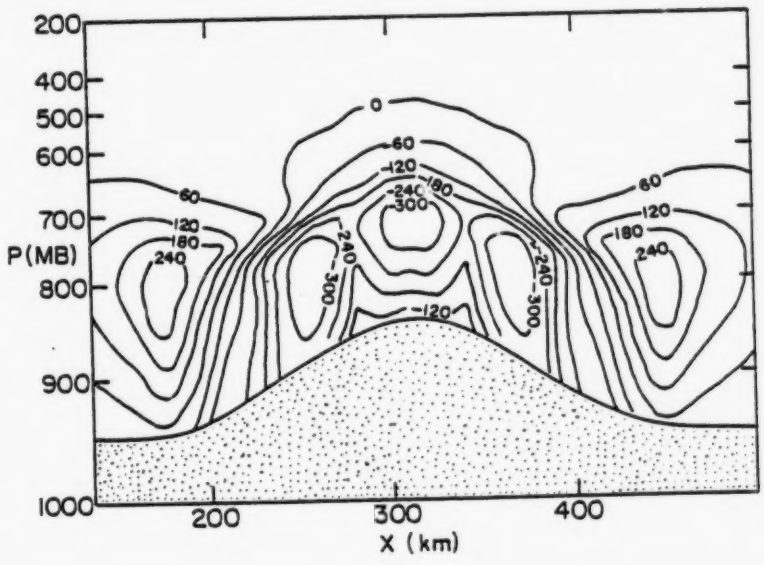

(b)

Fig. 15. Vertical velocities above a smooth, synthetic terrain profile after 2h (a) and 6h (b). The contours are labeled in cb s^{-1} ($x10^6$).

and one over each slope. The regions of subsidence associated with the return flow have moved to a position 140 km from the ridge centerline by 6 h. Fig. 16 depicts the u velocity component at 6 h. Upslope flow maxima of 1.9 m s^{-1} are observed at the lowest model layer, while the return flow aloft reaches 1.8 m s^{-1}. The intensity of the circulation defined by the speed of the low-level wind reaches a maximum after 8 h and then diminishes as afternoon solar forcing continues to become weaker.

In summary, the upward motion along the ridge slope is initially confined to a shallow layer whereas the upward motion above the ridge is much deeper. As the heating cycle progresses, the regions of subsidence are forced farther from the ridge as the upward motion over the sides of the ridge extends closer to the base of the ridge and extends through a deeper layer. It should be understood that this simulation only provides a qualitative indication of the nature of the circulation forced by the real terrain profile. Steeper terrain gradients and asymmetries will alter the circulations in important respects.

Simulation P2 is identical to P1 except that the observed terrain is substituted for the idealized ridge. The vertical motion pattern, which is perhaps one of the most effective fields for characterizing the circulations, is shown in Fig. 17 for 6 and 10 h. At 6 h, corresponding to 1030 L.A.T., the upward motion over the ridge has attained a speed of over 6 cm s^{-1} and extends well down the sides of the ridge to the valley. Because the western slope of the main Appalachian Ridge (to the east of the valley) is steeper than the slope on the east side, the upward motion field is stronger to the west of the ridge centerline. The upward motion maximum over the smaller ridge in the west edge of the valley attains a value at

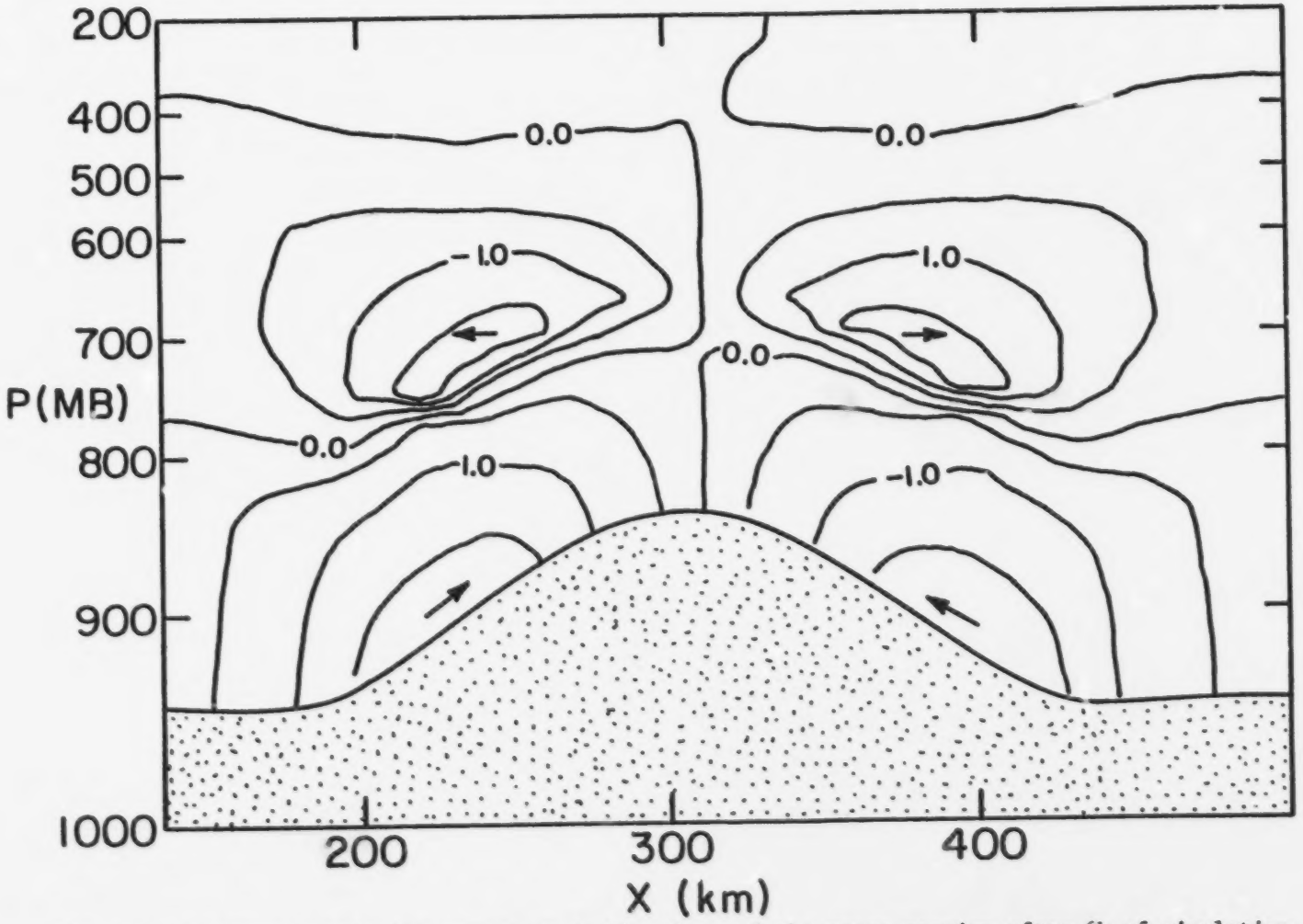

Fig. 16. Horizontal velocity component in the plane of the cross section after 6h of simulation. The contour internal is 0.5 m s^{-1}.

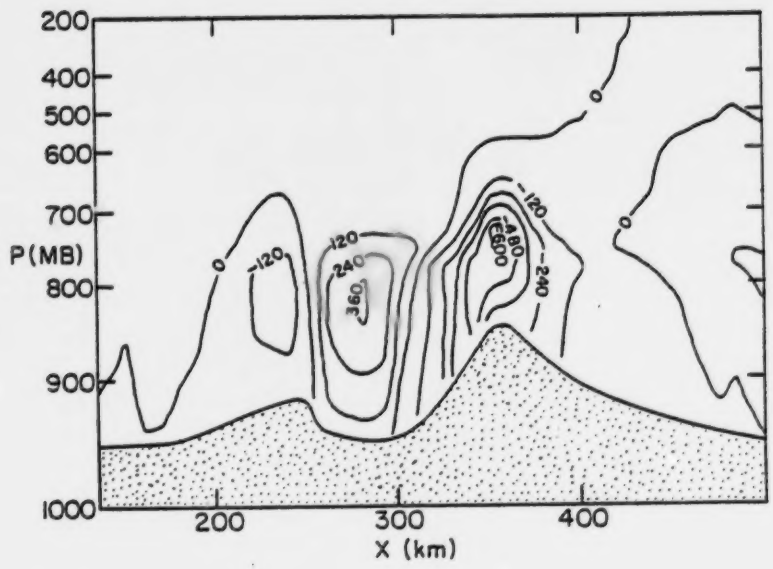

(a)

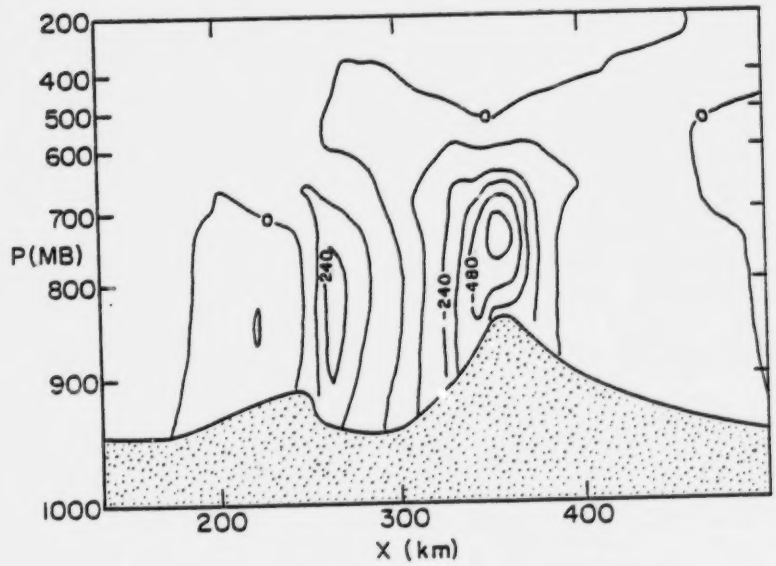

(b)

Fig. 17. Vertical velocities above the observed terrain profile after 6h (a) and 10h (b) where the solar forcing was appropriate for 21 June. The contours are labeled in cb s^{-1} ($x10^6$).

6 h of 1.7 cm s^{-1}, roughly 25% of the vertical velocity over the ridge on the right. The subsidence over the Tennessee Valley represents a large fraction of the return circulation from the two zones of upward motion. Its width is greatest at high levels where the upward motion has not spread laterally to as great a degree as it has near the surface. Table 4 illustrates the transitions undergone by the extrema in the vertical motion pattern over the two ridges and the valley. After 12 h, corresponding to 1630 L.A.T., the subsidence over the valley has diminished dramatically from a maximum of almost 4.0 cm s^{-1} to 1.3 cm s^{-1}.

Table 4

Transitions in the vertical motion extrema for P2 (23 June) and P3 (1 April)

Time(h)	Left Ridge (cm s^{-1})		Right Ridge (cm s^{-1})		Tennessee Valley (cm s^{-1})	
	P2	P3	P2	P3	P2	P3
2	0.5	0.2	1.5	0.6	-0.6	-0.4
4	1.7	1.3	5.4	4.0	-2.4	-1.8
6	1.7	1.7	6.2	6.0	-3.8	-3.5
8	1.5	1.4	6.1	5.7	-3.5	-3.3
10	1.2	1.0	6.5	5.2	-3.0	-2.4
12	0.9	*	5.1	*	-1.3	*

*unavailable

The eastern half of the Tennessee Valley is dominated by the westward spread of the upward motion from the large ridge. The subsidence has displaced the western, upward motion maximum to the western slope of the ridge. Upward motion over the large ridge is still being maintained at near the maximum intensity.

In order to provide some insight into the seasonal variability of this mesoscale circulation pattern, another experiment (P3) was conducted where the solar forcing was appropriate to 1 April. The initial time of the model remained at 0430 L.A.T. so that the elapsed forecast time has the same relationship to the local time as in simulation P2. Sunrise in P2 is about one hour earlier than in P3.

Table 4 also summarizes the development of vertical motions during this experiment. Percentage differences in vertical motion extrema between P2 and P3 average 5-15% for corresponding times. The patterns of vertical motion for P2 and P3 are similar. However, in P3, the large cell of upward motion did not displace the subsidence and western upward motion cell as far to the west as was the case in P2 with the stronger solar forcing. This relationship will be illustrated in a later discussion of other sensitivity experiments that employ a specified surface heat flux. Because our objective in comparing P2 and P3 is to analyze only the sensitivity of the solution to the amount of solar forcing, we have not changed any of the seasonally varying parameters that contribute to the net forcing such as albedo. In addition, these experiments, P1 through P5, are primarily intended to provide insight into the general nature of the circulations and thus a full range of seasonal forcing dates was not chosen.

The following questions about the circulations observed in P2 and P3 are suggested by the previous analysis.

1) Would the subsidence over the Tennessee Valley exist as close to the eastern ridge if a valley did not exist - that is, if the western ridge did not exist and hence no valley was defined.
2) To what degree, if any, is the upward motion over the western ridge suppressed by the return circulation of the eastern ridge.
3) Is the subsidence area between the ridges enhanced in intensity because of the existence of the western ridge or does this ridge's

spatially confining influence depress the intensity of the subsidence.

These questions can be addressed by evaluating simulations that have been performed without the eastern ridge (P4) and without the western ridge (P5). We will first compare simulation P5, without the western ridge, with P2 having the complete terrain profile. Figs. 18a and b illustrate the 6 h and 10 h vertical velocity predictions without the western ridge and should be compared with Figs. 17a and b. Table 5 compares simulations P2 and P5 in terms of the magnitude of the downward motion maximum, its displacement to the west of the center of the eastern ridge, the width of the region of subsidence, and the distance the upward vertical motion extends to the west of the ridge at ridge-top level. The intensity of the subsidence at 6 h is 30% less without the western ridge. After 10 h, the subsidence in the simulation without the ridge has moved so far to the west that it is no longer well represented on the computational domain.

Clearly, the western ridge does exert a strong influence on the location of the subsidence especially during the last half of the forecast. Also the magnitudes of the downward motion are 50% to 75% greater with the western ridge than without it.

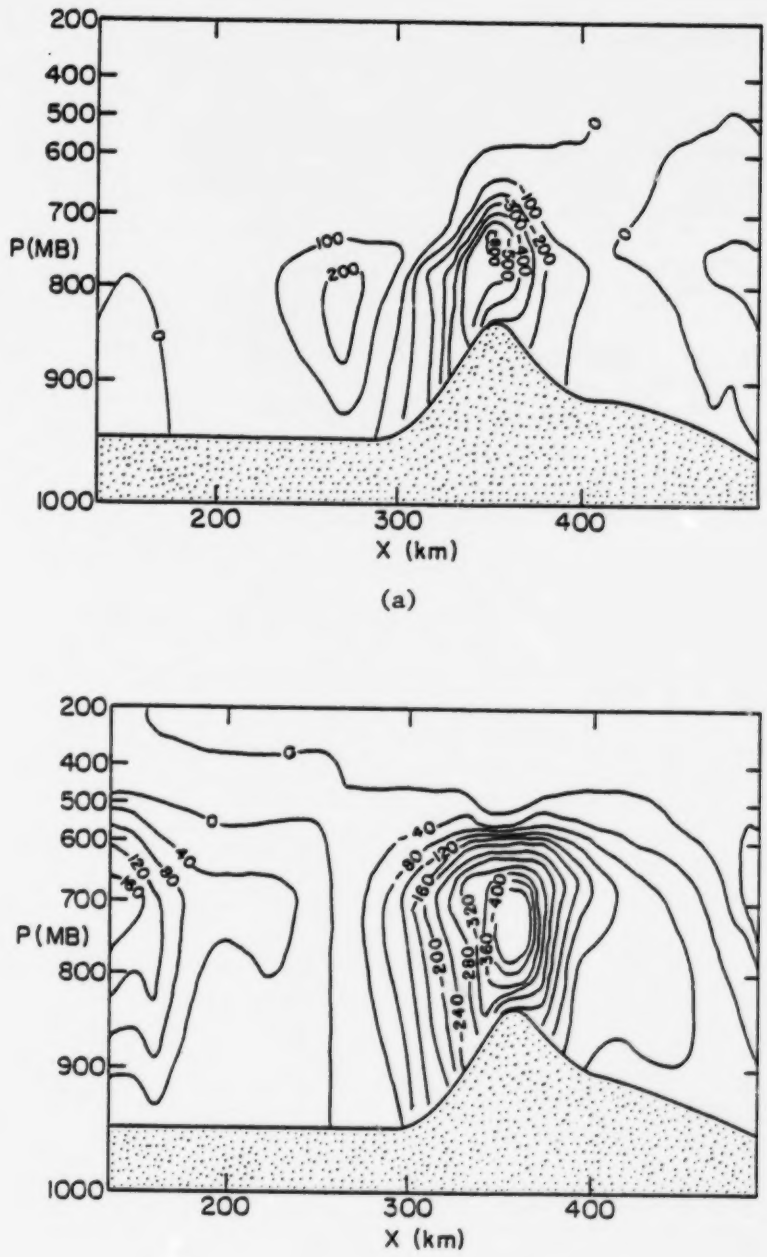

Fig. 18. Vertical velocities above the observed terrain profile with the western ridge removed after 6h (a) and 10h (b) where the solar forcing was appropriate for 21 June. The contours are labeled in cb s^{-1} ($x10^6$).

Table 5

Comparison of simulations P2 and P5
(with and without the western ridge)

Time (h)	Maximum subsidence ($cm\ s^{-1}$)		Distance of subsidence maximum from east ridge top (km)		Width of subsidence at ridge-top level (km)		Halfwidth of upward vertical motion over east ridge at ridge-top level (km)	
	P2	P5	P2	P5	P2	P5	P2	P5
2	0.7	0.7	33	33	75	120	20	20
4	2.5	2.2	55	55	70	130	35	39
6	3.8	2.6	80	85	57	130	53	55
8	3.5	2.1	90	125	55	140	55	55
10	3.1	1.7*	100	155	58	150†	59	63
12	1.5	1.7*	100	215	50	120†	70	100

*maximum is near lateral boundary

†distance from zero vertical motion isotach to west boundary

There are at least two explanations for this observation. First, the additional upward motion over the western ridge forces a region of subsidence along its steepest slope to the east which enhances the downward motion forced by the east ridge. Second, the effect of the western ridge to confine the lateral westward spread of the subsidence results in a faster downward current being required to provide the same vertical mass flux.

In order to answer question number two, a simulation without the eastern ridge is required to determine if the subsidence produced by the east ridge tends to suppress the upward motion from the west ridge. This simulation (P4) is to be compared to P2 having the same solar forcing but with both ridges included. Fig. 19 is the 6 h solution from P4. It shows a significantly enhanced field of upward motion when compared to the solution at the equivalent time in P2 (Fig. 17 a). Table 6 indicates the evolution of the upward motion over the west ridge in both P2 and P4.

Table 6

Upward motion maximum over west ridge

	maximum w (cm s^{-1})	
Time (h)	With E. ridge (P2)	Without E. ridge (P4)
2	0.45	0.48
4	1.71	2.05
6	1.73	2.79
8	1.46	2.84
10	1.24	3.02
12	0.87	2.25

The upward vertical velocities over the west ridge are being depressed significantly by the stabilizing effect of the subsidence from the east ridge.

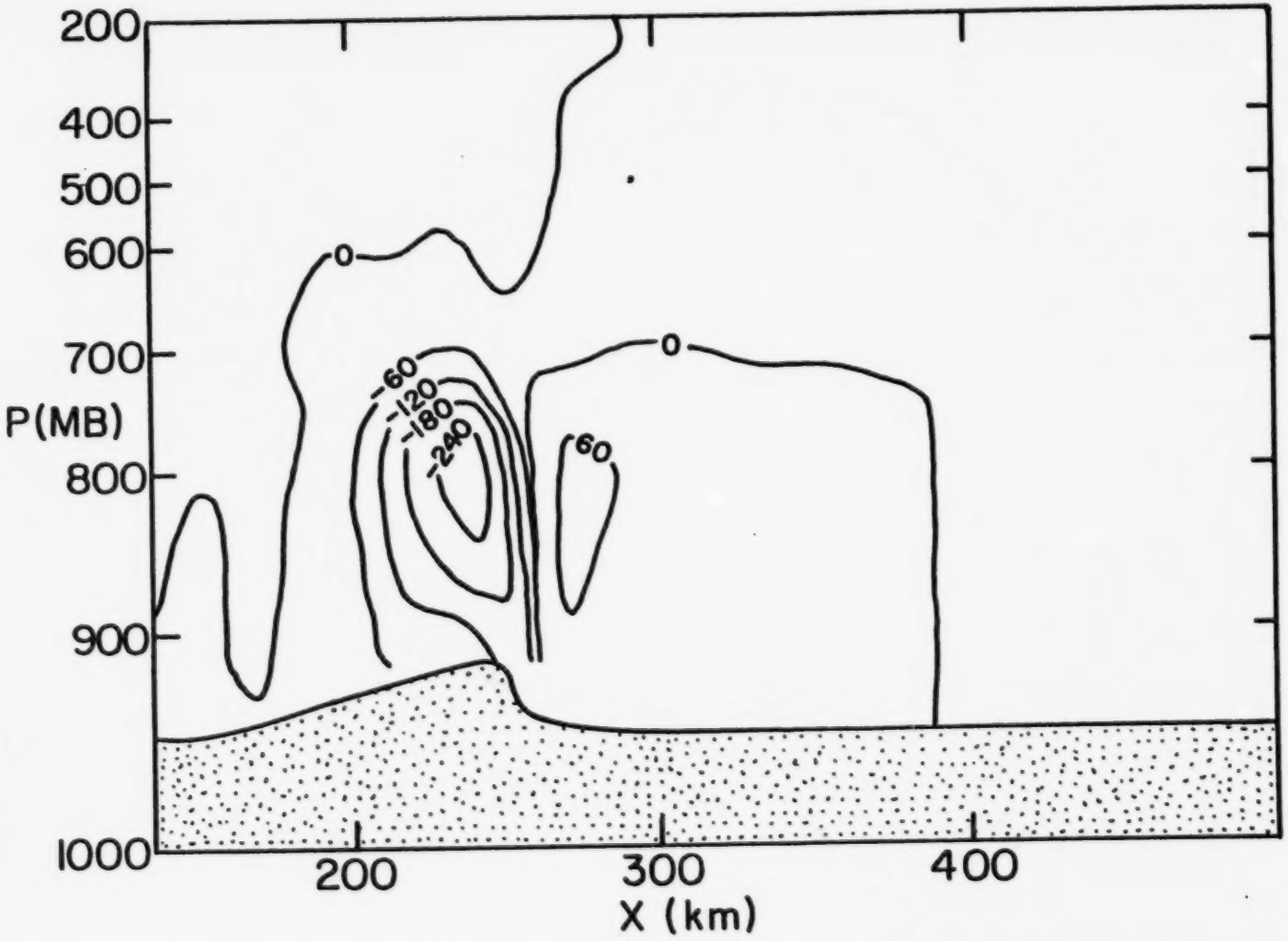

Fig. 19. Vertical velocities above the observed terrain profile with the eastern ridge removed after 6h where the solar forcing was appropriate for 21 June. The contours are labeled in cb s^{-1} ($x10^6$).

In summary, the circulations from the two ridges do interact with one another. The net effect of the superposition of the circulations from the two upper-level heat sources is not simply the sum of the individual flow fields that would be realized from the isolated ridges. It has been shown that by adding the west ridge to the topography, the subsidence field from the east ridge does not progress westward with time, but is confined to an area near the ridge itself. Also, upward motion over the west ridge is depressed by the subsidence from the east ridge while the magnitude of the subsidence over the valley is greater with both ridges than it would be with either one separately.

2. MOUNTAIN-VALLEY CIRCULATION SENSITIVITY STUDIES

The next set of experiments will evaluate the effect of the intensity of the thermal forcing on the nature of the resulting circulation patterns. The following questions will be addressed.

1) Is the response of the amplitude of the circulations, as reflected by the vertical motion maxima, an approximately linear function of the thermal forcing?

2) Does the dominance of the circulation by the large eastern ridge depend on the intensity of the forcing?

Six simulations were performed using surface, sensible heat fluxes specified according to equation (1) with values of H_o ranging from 15% to 40% of the solar constant. Figure 20 summarizes the response of the vertical motion field to the thermal forcing. It indicates a nearly linear relationship in most cases between the amplitude of the vertical motion pattern and the amplitude of the surface thermal forcing. The overall spatial pattern of the motion field is not significantly different among the six

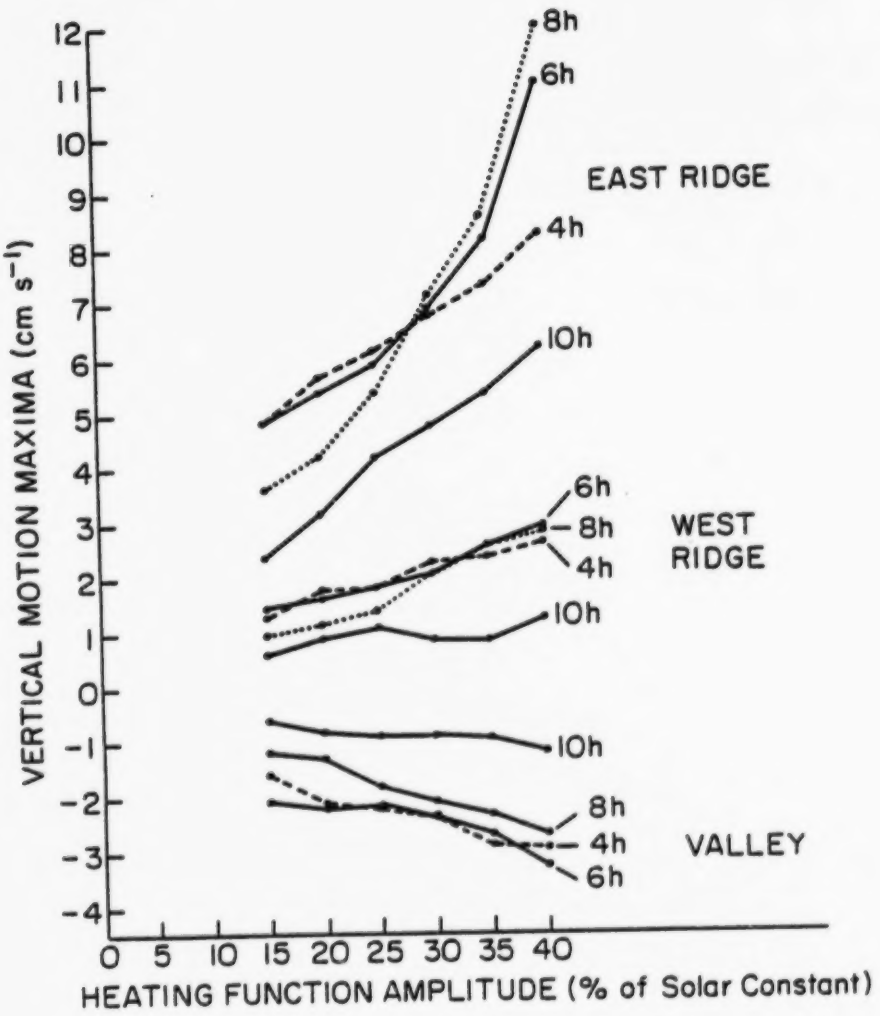

Fig. 20. Vertical motion maxima at 2h intervals for the Tennessee Valley simulation where upward motion maxima are plotted for positions over the east and west ridge and the downward motion maximum corresponds to a position over the valley.

experiments either. Figs. 21 a-c show the vertical motions at the 6 h point in the simulations. The width of the subsidence does not vary significantly with the level of forcing. Some evidence of the dominant influence of the eastern ridge is apparent in the 10 h data of Fig. 20. With increasing amplitude of the surface sensible heat flux, a decrease is observed in the upward motion over the western ridge. This probably results from the previously observed stabilizing influence of the subsidence forced by the eastern ridge. Such an effect is not evident before 10 h however.

3) OBSERVED SUBSIDENCE OVER THE TENNESSEE VALLEY

Because conventional, three dimensional observations on the mesoscale are generally not available, nonstandard sources must often be utilized. In order to subjectively verify the existence of the forecast subsidence over the Tennessee Valley and to understand its importance to the local climatology, we have surveyed visible image satellite photographs to determine if cloud patterns indicate the existence of vertical motions in the region. One would logically expect to observe enhanced convection over the main ridge of the Appalachians, however, it is not as obvious that manifestations of the predicted subsidence over the Tennessee Valley as well as convection over the small ridge to the west of the valley should be apparent.

After beginning the study of the satellite visible imagery it immediately became apparent that the existence of the Tennessee Valley often has a dramatic imprint on the local cloud formation and distribution. On numerous occasions, especially it seemed during the spring months, scattered cumulus clouds would prevail over much of the Appalachian Mountain Range and the southeast in general. In the vicinity of the Tennessee Valley however there would be a distinct absence of cumulus activity.

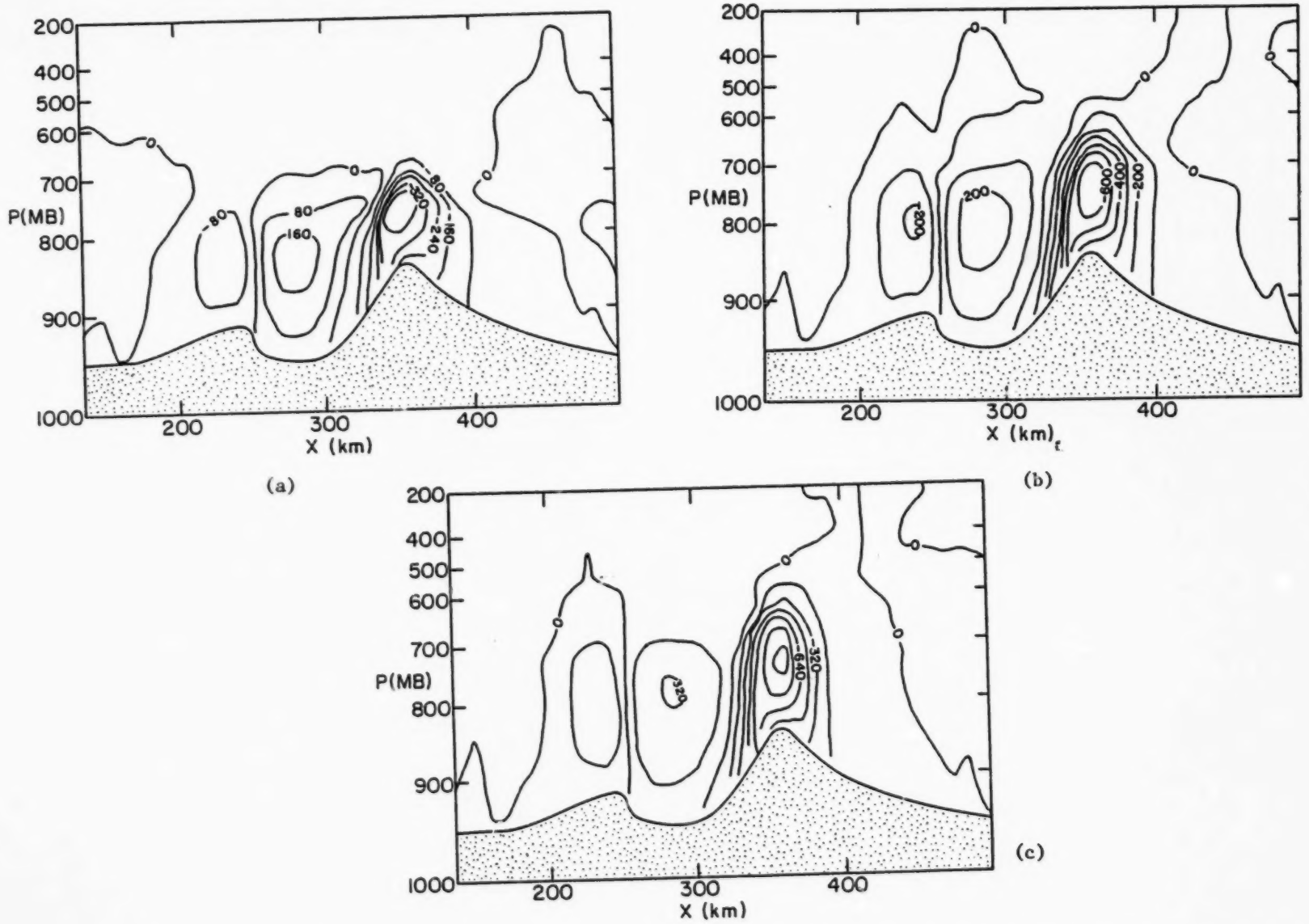

Fig. 21. Vertical velocities above the observed terrain profile after 6h of simulation where the heat flux amplitude was 15% (a), 30% (b), and 40% (c) of the solar constant. The contours are labeled in cb s^{-1} ($x10^6$).

Figs. 22 and 23 show four examples of the existence of this cloud-free zone that presumably existed because of the prevailing mesoscale subsidence pattern. In these cases, scattered cumulus clouds prevailed over a large area rather than simply being concentrated over the ridge tops. Therefore, an anomalous clear area should represent subsidence rather than simply a lack of organized upward motion. The frequency with which this feature is observed and the regularity of its location, size, and orientation implies the existence of a relationship between it and a topographic forcing mechanism. It would be unlikely, for example, that it results from anomalies in the moisture field.

c. Sensitivity of the heat flux to ground characteristics

The sensitivity studies just described were performed by varying the amplitude of a surface heat flux function. In order to relate these results to errors in the specification of ground characteristics, which are required by the surface energy equation in the version of the model where surface heat fluxes are calculated and not specified, we must understand how sensitive the computed heat flux is to these ground parameters.

Sensitivity tests were performed by Shaginaw (1979) using Blackadar's slab model (Blackadar, 1976) coupled with a one grid point, time dependent PBL model that used a bulk parameterization proposed by Deardorff (1972). The object of this series of tests was to evaluate the dependence of the surface heat flux on soil heat capacity, soil thermal conductivity, surface albedo, and surface roughness. Eighty-one forecasts were made corresponding to different combinations of surface parameters. Figs. 24 through 27 show the relationships between these parameters and the maximum daytime surface sensible heat flux. If an estimate is required of the error in the computed heat flux maximum that is associated with an error in specifying a particular surface parameter,

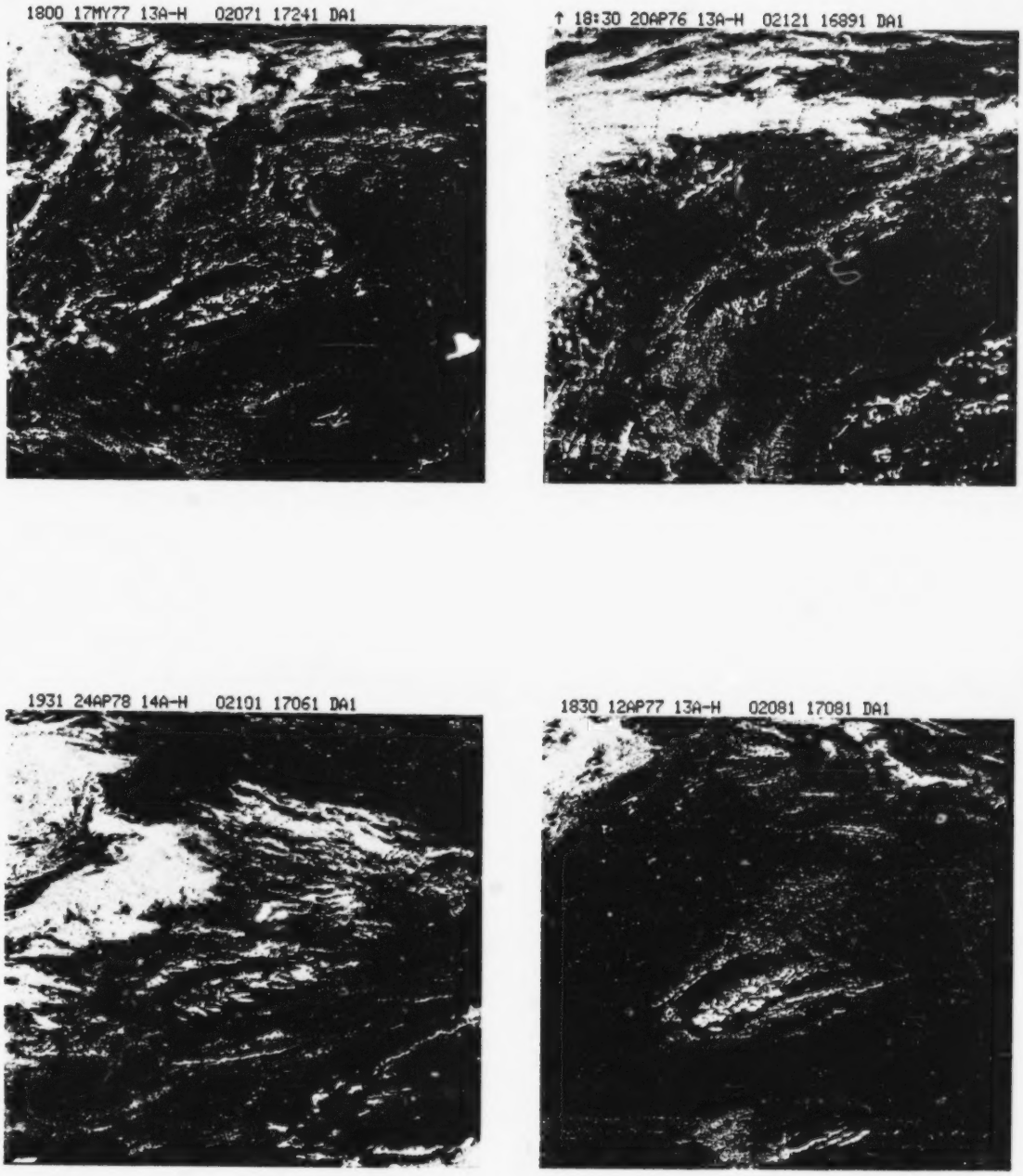

Fig. 22. Four examples of the existence of a cloud-free region over the Tennessee Valley where the surrounding areas were generally characterized by scattered cumulus clouds.

Fig. 23. Enlargement of Fig. 22 example of cloud-free region over Tennessee Valley.

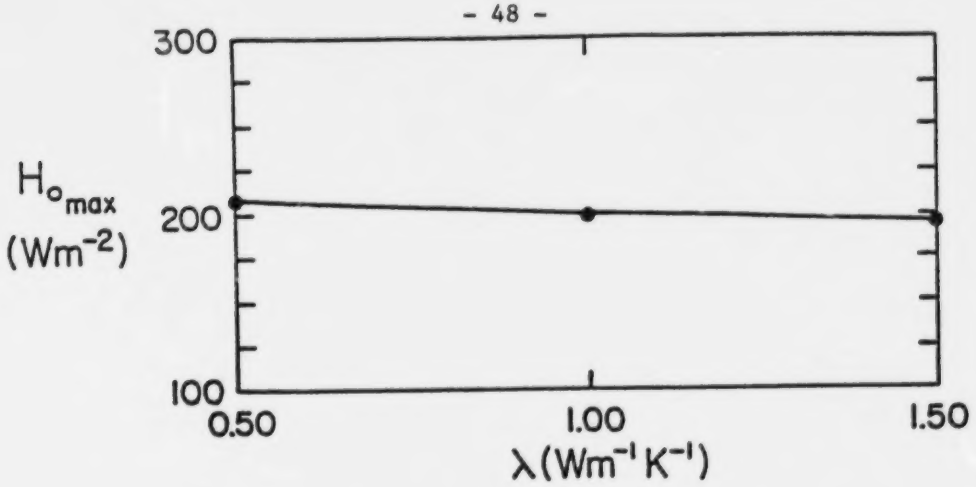

Fig. 24. Maximum surface heat flux as a function of soil thermal conductivity, λ. For these simulations, the roughnes length was 10 cm, the albedo was 0.40 and the soil heat capacity was 2.0×10^6 J m^{-3} K^{-1}.

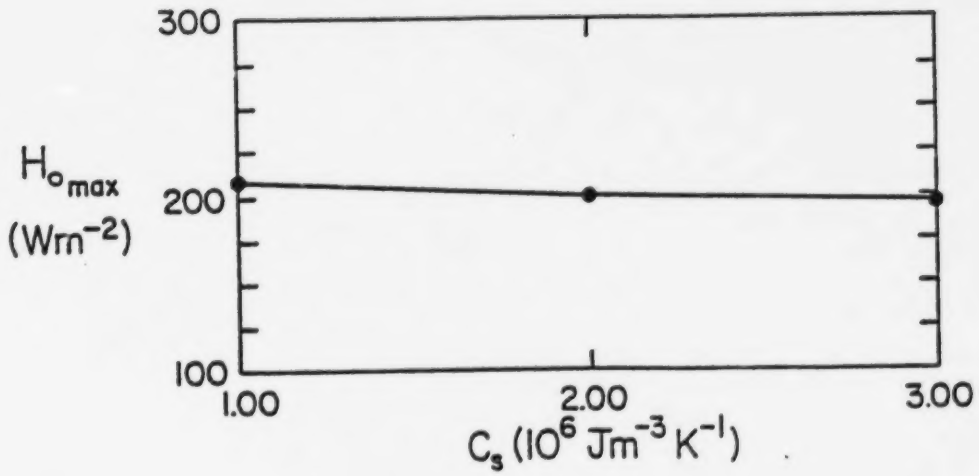

Fig. 25. Maximum surface heat flux as a function of soil heat capacity, C_s. For these simulations, the roughness length was 10 cm, the albedo was 0.40 and the soil thermal conductivity was 1.0 $Wm^{-1}K^{-1}$.

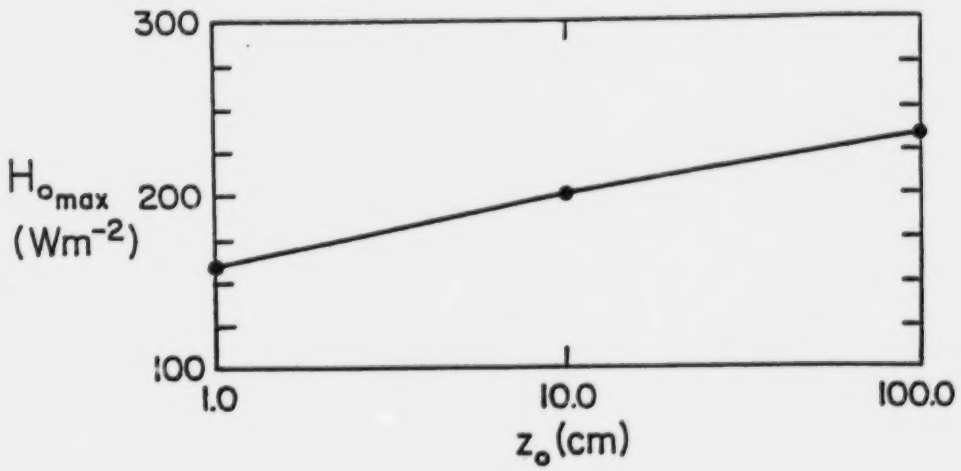

Fig. 26. Maximum surface heat flux as a function of aerodynamic roughness length, z_o. For these simulations, the albedo was 0.4, the soil thermal conductivity was 1.0 $Wm^{-1}K^{-1}$ and the soil heat capacity was 2.0 x 10^6 J $m^{-3}K^{-1}$.

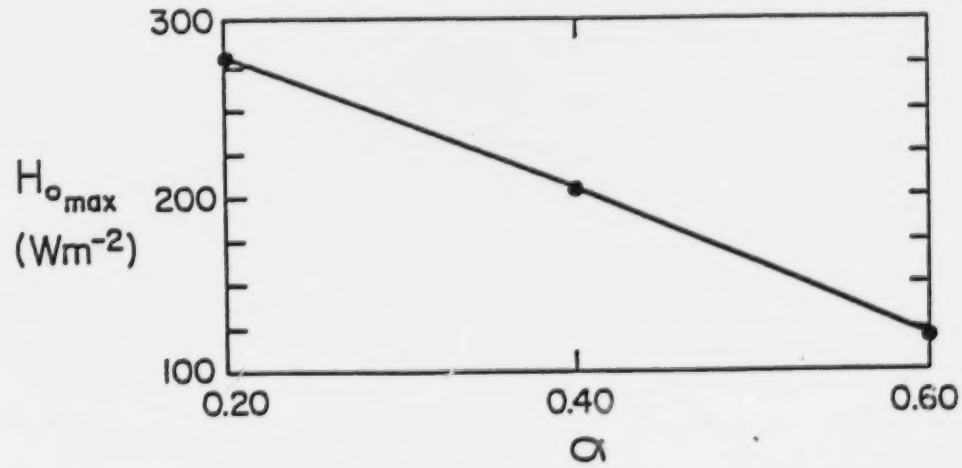

Fig. 27. Maximum surface heat flux as a function of surface albedo, α. For these simulations, the roughness length was 10 cm, the soil thermal conductivity was 1.0 $Wm^{-1}K^{-1}$ and the soil heat capacity was 2.0 x 10^6 $Jm^{-3}K^{-1}$.

these graphs may be used. In summary, reasonable errors in soil conductivity and heat capacity do not significantly alter the maximum surface heat flux. However, erroneous specification of the albedo and roughness length produces more significant errors.

4. Diurnal oscillation of the planetary boundary layer structure

In this section the transitions of the wind and thermal structure of the PBL, in the vicinity of an elevated heat source, will be evaluated for typical solar heating cycles. Experiment P1 discussed in Section 3.b., which used solar forcing appropriate for the summer solstice to generate a circulation over an idealized ridge profile, will be used to illustrate how the evolution of the atmospheric temperature structure in the PBL depends on the proximity to the ridge.

Three grid points in the vicinity of the simple ridge profile were chosen to trace the evolution of the thermal structure of the atmosphere. Point one is a lateral boundary point where only vertical flux convergences of heat altered the temperature profile during the heating cycle, with no horizontal or vertical advection or adiabatic changes being possible. This point would represent any location not affected by the terrain-related circulation. Point two is located approximately half the distance between the top and base of the ridge and point three is at the top of the ridge. Fig. 28 depicts the temperature structure at the three points at 2 h intervals between 4 h and 12 h in the heating cycle.

The results are complicated by the fact that the initial temperature profile was defined as a function of p and not in terms of height above the ground. Thus, there are small differences among the three points in the initial static stability. We believe however, that differences among the

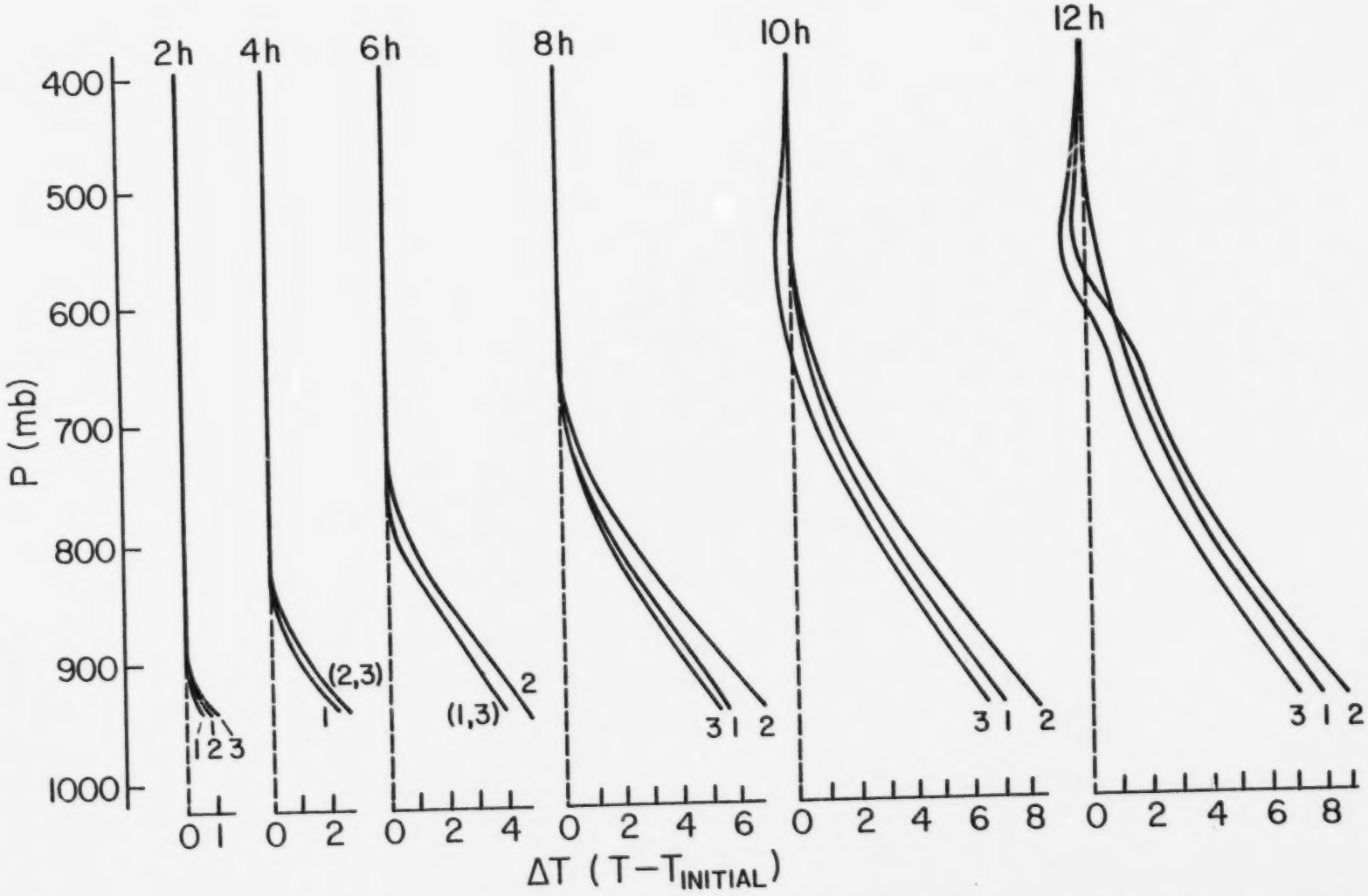

Fig. 28. Temperature change as a function of height at two hour intervals during simulation P1 for three points in the vicinity of a simple ridge profile.

three points, especially during the latter half of the heating cycle, are a result of the existence of the air motions associated with the mountain-valley circulation. Adiabatic cooling is taking place at points 2 and 3 because of the upward motion over the ridges. Three upward motion maxima actually exist; one over the ridge top and one over each slope. It should be recalled that the surface heat flux is calculated from similarity theory based on the difference between the ground temperature, calculated from the surface slab energy equation, and the air temperature at the lowest model layer. It is also proportional to u_* in the surface layer which is proportional to the wind in the lowest model layer. Also, the boundary layer heat fluxes are dependent on the local shear of the horizontal wind and the local static stability.

Two effects contribute to the enhanced heating observed on the mountain slope. The wind shear, which is greatest at low levels over the sides of the ridge, enhances the vertical heat flux out of the lowest layer and therefore reduces the temperature of this layer. The difference between the temperature in the lowest layer and the ground temperature is increased which produces larger surface heat fluxes. The most important factor however is more direct and results from the effect of the larger wind speed over the slope on the friction velocity u_* and, in turn, on the surface heat flux. The surface heat flux at point two at 6 h was 48% higher than at point one and 39% higher than at point three. This enhanced surface heat flux over the slope at point two produced a computed ground temperature at 6 h for this point that was 11°C less than at point one and 5°C less than at point three. A wind shear did not exist at point three, therefore the existence of adiabatic cooling from the upward motion represented the major dissimilarity between this point and point one. This explains the lesser amount of heating observed at point three compared to point one.

Figure 29 shows the profile of the wind component in the plane of the cross section, over either side of the ridge for various times between 2 h and 12 h of the simulation. The maximum speed at the lowest model layer exceeds 2 m s^{-1} and is attained between 6 h and 10 h. The height of the return circulation continually increases during the first 10 h of the simulation. The amplitude of this return flow does not diminish immediately after the maximum heat flux is observed as does the low-level, upslope flow. The 12 h amplitude is 2 m s^{-1} and represents an increase in the maximum speed at this level after a decrease was observed between 6 h and 10 h.

5. Summary and Conclusions

A cross-sectional, two-dimensional model was used to simulate circulations generated at a coastline and over the Tennessee Valley as a result of solar thermal forcing over land. Solar heating functions with a period of 12 h and amplitudes varying between 15% and 40% of the solar constant were imposed to investigate the sensitivity of the solution to the magnitude of the thermal forcing. Most quantifiable features of the circulations such as the speed of seabreeze-front and the magnitude of vertical motion extrema over the Tennessee Valley terrain anomalies, showed a quasi-linear response to the magnitude of the thermal forcing. The basic qualitative characteristics of the circulations such as the relative locations of vertical motion extrema in the sea breeze circulation or the relationship of these extrema to the top of the PBL, did not depend on the magnitude of the forcing however. These variations in the amplitude of the thermal forcing function were related to variations in surface characteristics such as albedo, soil conductivity and heat capacity and the roughness length, that are incorporated in a surface energy balance equation that is used to

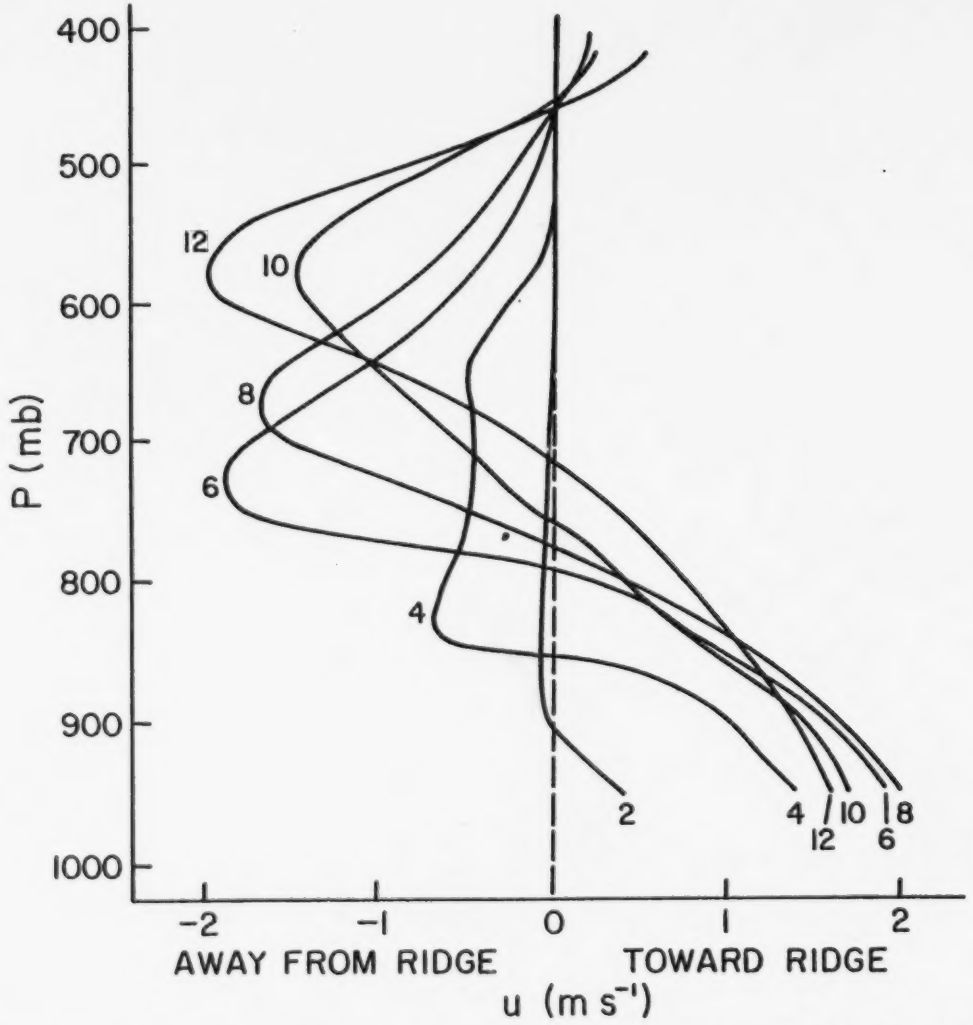

Fig. 29. Vertical profile of the horizontal wind component in the plane of the cross section for various times between 2h and 12h of simulation P1. The profile was located over the steepest terrain gradient of the simple ridge.

compute the heat flux as an alternative to specifying it. These results can be used to relate errors in the specification of any one of these surface parameters to the expected errors in the circulation features.

The Tennessee Valley simulations exhibited a pronounced subsidence region over the valley, where the cross-valley extent of the subsidence was shown to be closely related to the prevailing topographic features. A study of satellite imagery of this region showed anomalous cloud-free regions over the Tennessee Valley that could be related to the subsidence region predicted by the model.

References

Anthes, R. A., 1978: The height of the planetary boundary layer and the production of circulation in a sea breeze model. Journ. of Atmos. Sci., 35, 1231-1239.

Anthes, R. A. and T. T. Warner, 1978: Development of hydrodynamic models suitable for air pollution and other mesometeorological studies, Mon. Wea. Rev., 106, 1045-1078.

Blackadar, A. K., 1978: High resolution models of the planetary boundary layer, Advances in Environmental and Scientific Engineering, Vol. 1.

Brown, J. A., Jr., and K. A. Campana, 1978: An economical time-differencing system for numerical weather prediction, Mon. Wea. Rev., 106, 1125-1136.

Busch, N. E., S. W. Chang and R. A. Anthes, 1976: A multi-level model of the planetary boundary layer suitable for use with mesoscale dynamic models, Journ. Appl. Meteor., 15, 909-919.

Chandler, T. C., 1968: The bearing of the urban temperature field upon pollution patterns. Atmos. Environ., 2, 619-620.

Edinger, J. G. and R. A. Helvey, 1961: The San Fernando Convergence Zone. Bull. Amer. Meteor. Soc., 42, 626-634.

Findlay, B. F. and M. S. Hirt, 1969: An urban-induced meso-circulation. Atmos. Environ., 3, 537-542.

Keyser, D. and R. A. Anthes, 1977: The applicability of a mixed-layer model of the planetary boundary layer to real-data forecasting. Mon. Wea. Rev., 105, 1351-1371.

Lyons, W. A. and C. S. Keen, 1976: Computed 24-hour trajectories for aerosol and gases in a lake/land breeze circulation cell on the western shore of Lake Michigan. Proc. Sixth Conf. on Weather Forecasting and Analysis, May 10-14, 1976, Albany, N. Y., Published by the AMS, Boston, Mass., 78-83.

Lyons, W. A. and L. E. Olson, 1973: Detailed mesometeorological studies of air pollution dispersion in the Chicago lake breeze. Mon. Wea. Rev., 101, 387-403.

Metaxas, D. A., 1978: Evidence on the importance of diabatic heating as a divergence factor in the Mediterranean, Archives for Meteor., Geophys. and Bioclim., Series A., 27, 69-80.

Pielke, R. A., 1974: A three dimensional numerical model of the sea breeze over south Florida, Mon. Wea. Rev., 102, 115-139.

References (Continued)

Plank, V. G., 1960: Cumulus convection over Florida. Cumulus Dynamics: Proc. of First Conf. on Cumulus Convection (Ed. C. E. Anderson), Pergamon.

Venkatesh, S. and M. B. Danard, 1978: A model for computing small-scale wind variations over a water surface, Boundary Layer Meteor., 14, 35-57.

Warner, T. T., R. A. Anthes and A. L. McNab, 1978a: Numerical simulations with a three-dimensional mesoscale model, Mon. Wea. Rev., 106, 1079-1099.

Warner, T. T., R. A. Anthes and A. L. McNab, 1978b: Numerical simulations of coastal-zone boundary layer ventilation and pollution transport. Proc. 9th International Technical Meeting on Air Pollution Modeling and Its Application, August 28-31, 1978, Toronto, Canada.

Williams, W. A. and R. E. DeMandel, 1966: Land-sea boundary effects on small-scale circulations. Progress Report No. 2, San Jose State College Meteorology Department, NSF Grant GP-4248, 97 pp.

Comparisons of Numerical Simulations of the Planetary Boundary Layer by a Mixed-Layer and Multilevel Model.

Abstract

A series of increasingly complicated meteorological circulations is modeled by a two-dimensional, multilevel primitive equation model (MLM) and a one-dimensional mixed layer model (XLM) in order to determine the extent to which the simple mixed-layer model can provide accurate predictions of the mean structure of the planetary boundary layer (PBL). Under horizontally homogeneous conditions, the PBL structure in the XLM agreed closely with the average structure in the MLM. When horizontal inhomogeneities associated with differential heating over complex terrain and across a land-water boundary were introduced, the XLM solutions became less accurate when compared to the MLM solutions. For these conditions a multilevel model appears to be essential to the correct prediction of flow within the PBL, because mass-wind adjustments in the flow above the PBL produce important changes on the pressure gradient within the PBL.

1. Introduction

Forecasts and simulations of mean temperatures, humidities and winds in the planetary boundary layer (PBL) as well as the depth of the PBL have many applications in the fields of meteorology, air pollution, and energy. Two and three dimensional primitive equation models have recently been used to model the PBL structure in complicated situations such as mountainous terrain and coastal areas (Pielke, 1974; Mahrer and Pielke, 1975; Warner, et al. 1978; Anthes, 1978). While the above models appear to produce rather complete and realistic portrayals of the development of the PBL in response to differential heating, their complexity requires large computers and much computer time. Much simpler and less expensive models of the PBL alone exist and have been tested in various situations (Lavoie, 1972, 1974; Keyser and Anthes, 1977). These models, which typically require an order of magnitude less computing, also appear to model the mean structure of the PBL with considerable realism. The purpose of this paper is to compare the structure of the PBL as predicted by the mixed-layer model of Keyser and Anthes (1977) with the multilevel model of Anthes and Warner (1978a), in order to determine under what conditions, if any, the mixed-layer model can be used in lieu of the expensive multilevel model. We consider a hierarchy of increasingly complex physical situations. The first set of comparisons is made under the simplest situation of horizontal homogeneity, a situation in which the two models might be expected to agree most closely. Then horizontal inhomogeneties are introduced in a simple sea-breeze simulation utilizing flat terrain. Finally, terrain variations are introduced with a sea-breeze in the most complicated set of physical conditions.

2. Simulations under horizontally homogeneous conditions

As a first step in comparing the ability of the mixed layer model (XLM) to reproduce the mean structure of the PBL as forecast by a multi-level model (MLM), we eliminate all horizontal derivatives in the two models. Thus the models represent the PBL at one location in space under horizontally homogeneous conditions. The MLM equations are given by Busch et al. (1976). The XLM equations are

$$\frac{\partial \underset{\sim}{V}}{\partial t} = - f \hat{k} \times (\underset{\sim}{V} - \underset{\sim}{V}_g(H)) \quad - \frac{C_D |\underset{\sim}{V}| \underset{\sim}{V}}{(h - z_s)} + \frac{\partial \underset{\sim}{V}}{\partial t} \Big]_{ent} \tag{1}$$

$$\frac{\partial \theta}{\partial t} = \frac{F_{QV}(z_s)}{\rho(z_s) C_p (h - z_s)} + \frac{\partial \theta}{\partial t} \Big]_{ent} + \frac{\partial \theta}{\partial t} \Big]_{ca} \tag{2}$$

$$\frac{\partial h}{\partial t} = S + \frac{\partial h}{\partial t} \Big]_{ca} \tag{3}$$

Here $\underset{\sim}{V}$ is the mean horizontal velocity in the PBL, $\underset{\sim}{V}_g$ is the geostrophic wind at H, the height of the undisturbed layer, C_D is the drag coefficient, h is the height of the PBL, z_s is the terrain elevation, θ is the mean potential temperature in the PBL, F_{QV} is the vertical heat flux, ρ is density, c_p is specific heat for dry air, and S is a source term which models the growth of the mixed layer due to entrainment. The subscripts $]_{ent}$ and $]_{ca}$ denote entrainment and convective adjustment effects respectively. All of these terms are described by Keyser and Anthes (1977).

In the XLM, the initial values of θ, $\theta(h)$ (potential temperature immediately above h), and h are 296.85, 297.85 and 200 m respectively. In the MLM, the horizontal velocity components and potential temperature

Table 1 Horizontally homogeneous simulations

Exp.	Maximum Heating (α=Fraction of S_o)	z_o (cm)	u_g (m s^{-1})
1	0.25	1.0	2.0
2	0.25	100.	2.0
3	0.25	1.0	0.0
4	0.25	100.	0.0
5	0.25	1.0	5.0
6	0.25	100.	5.0
7	0.25	1.0	10.0
8	0.25	100.	10.0
9	0.0	1.0	5.0
10	0.0	100.	5.0
11	0.0	1.0	10.0
12	0.0	100.	10.0
13	0.18 sin π (t-1)/12	1.0	5.0
14	0.18 sin π (t-1)/12	1.0	0.0

are defined at 0, 50, 150, 250 ... 1850 m while the vertical fluxes of heat and momentum and the Richardson number are defined at 25, 100, 200, ... 1800 m. In both models the Coriolis parameter is 1.0×10^{-4} s^{-1} and the vertical gradient of θ above the PBL is 5 K km^{-1}.

A number of simulations were run with various values of surface roughness, geostrophic wind and heating (Table 1). The first 12 simulations are compared after 3h of either no heating or a heating function given by

$$F_{QV} = \begin{cases} 0 & 0 \leq t < 1 \text{ h} \\ \alpha S_o (t-1) & 1 \leq t < 2 \text{ h} \\ \alpha S_o & 2 \leq t < 3 \text{ h} \end{cases} \qquad (4)$$

where S_o is the solar constant (1395 W m^{-2}) and t is time in hours. This heating function was chosen to enable a comparison of the temporal behavior of each experiment under no heating (0-1 h) and a constant, moderately strong heating between 2 and 3 h. The period (2-3 h) represents a simple transition in the heating function. In the first 12 simulations, the surface roughness is either 1 or 100 cm, and the geostrophic wind (u_g) is 0.0, 2.0, 5.0 or 10.0 m s^{-1}.

In comparing the two models, the interesting parameters are the mean values of potential temperature (θ), horizontal wind components (u and v) and depth (h) of the PBL. Because of the different methods of computing these variables in the two models, there is no guarantee that these parameters will be equal, even though the initial conditions and surface heat flux are identical. Agreement between the two models does not say that both models are correct, it only implies a certain consistancy

between them. However, serious disagreement indicates a deficiency in one (or both) of the models and would have to be explained. Reasonable agreement in these simple comparison simulations is a prerequisite for further comparisons under inhomogeneous conditions.

In the XLM, the initial winds are computed from an approximate balance among the friction, Coriolis and pressure gradient forces

$$\underset{\sim}{V}_B = \left(\frac{f^2 + fK\hat{k}x}{f^2 + K^2} \right) \underset{\sim}{V}_g \qquad (5)$$

where K is given by

$$K = \frac{C_D |\underset{\sim}{V}_g|}{(h - z_s)} \quad . \qquad (6)$$

In the MLM, such a simple balance is impossible and so the initial winds are geostrophic at t=0. Thus the initial u and v components in the PBL differ in the two models, especially for strong geostrophic wind conditions.

Fig. 1 shows the temporal evolution of θ, u and h in Exp. 1 for both models. During the first hour, in which heating is zero, θ and h remain nearly constant. The mean velocity decreases very slowly during this adiabatic period because of the weak frictional force under light winds and zero heating. At 1.0 h, θ and h begin to increase in both models at a similar rate. By 3.0 h the difference in θ is 0.4K (out of an increase of 3.85K), and the difference in h is 60 m (out of an increase of 600 m). The mean wind components are 1.79 and 1.73 m s^{-1} in the XLM and MLM respectively. The above agreement between the two models is typical for the first 12 experiments and is considered satisfactory.

A comparison of θ, h, u and v at 3 h in these preliminary forecasts is summarized in Figs. 2-5. The agreement between the two predictions

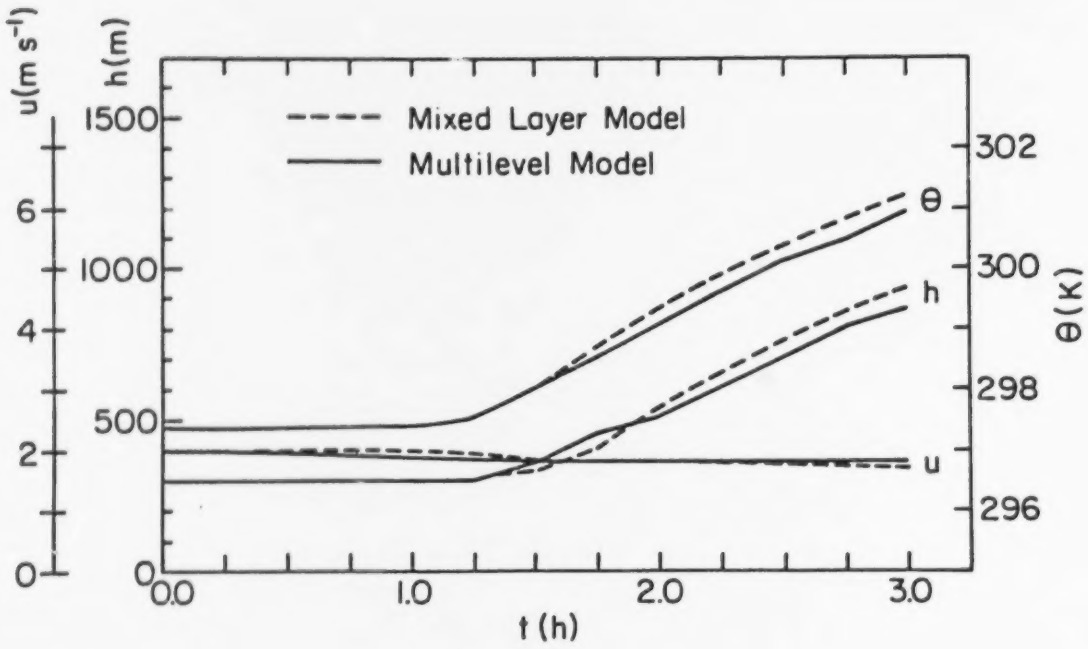

Figure 1. Temporal variation of θ(K), mixed-layer depth, h(m), and mean PBL wind component, u(m s^{-1}), parallel to geostrophic wind in simulation 1. (Horizontally homogeneous conditions)

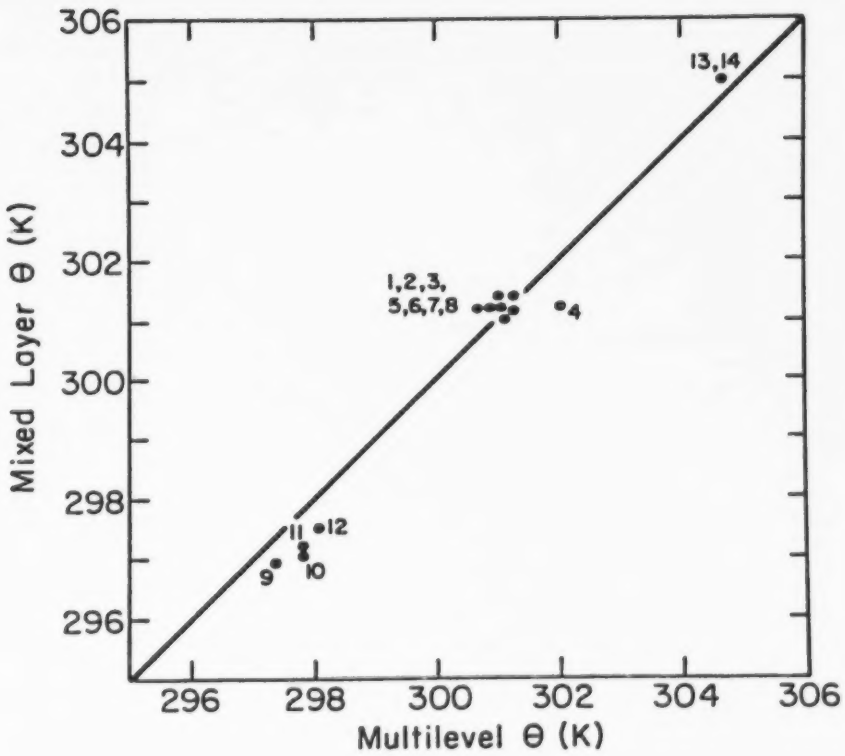

Figure 2. Mean PBL potential temperature, θ(K), after 3 h of simulation under horizontally homogeneous conditions predicted by the mixed-layer (XLM) and multilevel (MLM) model. The characteristics of the 14 simulations are described in Table 1 and the text.

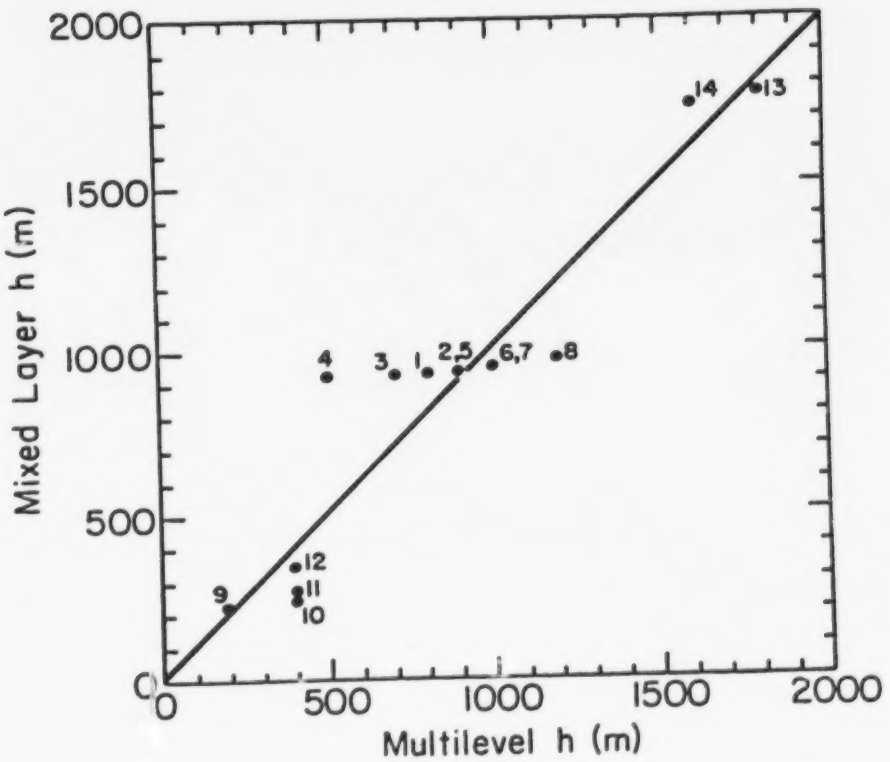

Figure 3. As in Fig. 2 except for height, h(m), of mixed layer.

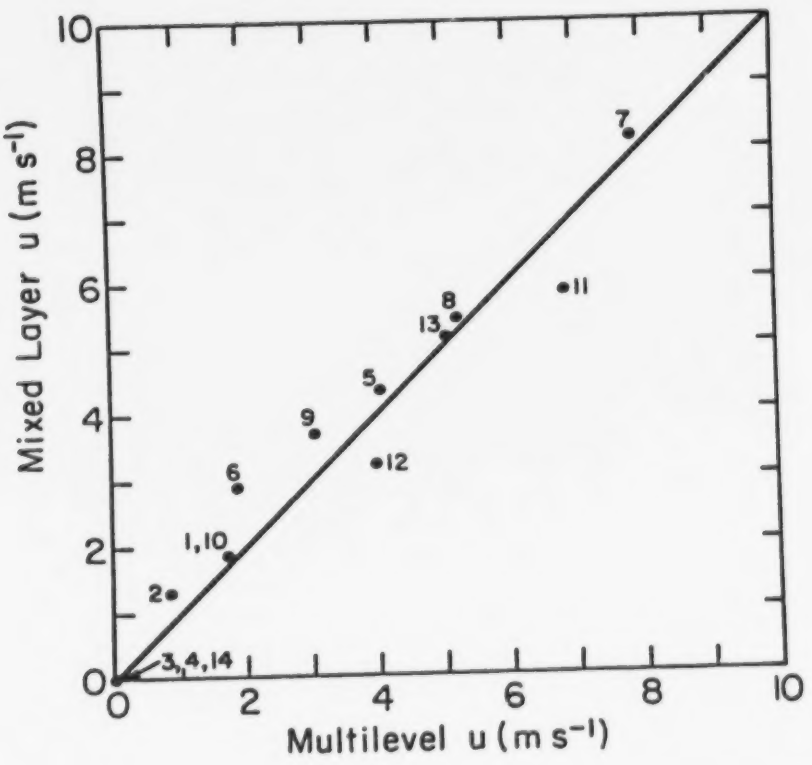

Figure 4. As in Fig. 2 except for mean PBL u-component ($m\ s^{-1}$).

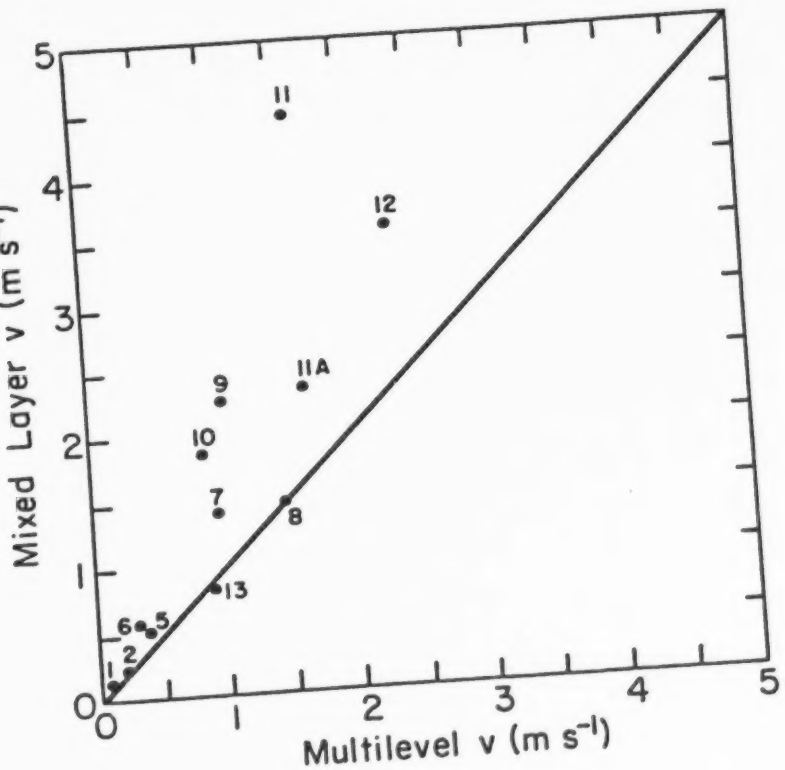

Figure 5. As in Fig. 2 except for mean PBL v-component (m s^{-1}).

of θ is quite good, as shown in Fig. 2. Without heating (Exp. 9-12), θ in the XLM is approximately 0.5K lower than θ in the MLM. With heating, the maximum difference is 0.8K. These small differences result from slight (0.5K) variations in initial values of θ and different methods of calculating the entrainment rates at h; they are not considered significant.

Fig. 3 shows a comparison of h at 3 h. The general agreement is fair, however, the MLM shows a greater range of h values for a given heat flux. In the first eight simulations, part of the variation in h predicted by the MLM is related to the variable geostrophic wind. The lowest mixed layers occur with zero geostrophic winds (Exps. 3 and 4) while the greatest depths occur for the fastest geostrophic winds (Exps. 7 and 8). The XLM, on the other hand, shows only a weak dependence of h on mechanical mixing.

There is an uncertainty in the value of h predicted by the MLM which makes comparisons of this parameter somewhat difficult. The MLM maintains a slightly stable temperature profile at all times. The height of the mixed layer is defined as the level above the highest level at which the Richardson number R_i is 0.25 or less. In calculating R_i under light wind conditions, a minimum wind shear of $10^{-3}s^{-1}$ is assumed. If the values of R_i at the model levels are close to 0.25, slight noise in the R_i profile may give different values of h. In any case, h can only be resolved to the nearest 100 m. This uncertainty is probably responsible for part of the range of values shown in Fig. 3.

The mean value of u predicted by the two models at 3 h is shown in Fig. 4. The agreement is quite good, with maximum differences being less than 1 m s^{-1}. The mean v-component, on the other hand, is significantly different in the two models (Fig. 5). The XLM v is consistently greater than the mean MLM v by about 1 m s^{-1}. This difference is related to the different initial conditions. In the MLM, $u=u_g$ and $v=0$ at the initial time. Therefore, it takes time for the cross-isobar flow component, v, to develop. To show that this is the main reason for the differences in Fig. 5, we reran Exp. 11 with geostrophic initial conditions for the XLM (Exp. 11A). The values of θ, h, and u at 3 h were virtually indistinguishable from those given by Exp. 11. However, the v-component was significantly less as shown in Fig. 5.

In the last two simulations of this section, the behavior of the two models over a 13h period under two geostrophic wind speeds is examined. In Exp. 13, $u_g=5$ m s^{-1} while in Exp. 14, $u_g=0$. In both experiments the initial conditions consist of geostrophic winds. Heating is zero for the first hour; then it is given by the function

$$F_{QV} = 0.18\ S_o \sin \pi\ (t-1)/12. \qquad 1h \leq t \leq 13h \tag{7}$$

Fig. 6 shows the temporal variation of the mean values of θ, h, and u for Exp. 13. After the first hour, the agreement is very close. Maximum differences are less than 0.5K, 80 m and 25 cm s^{-1} respectively. Somewhat greater differences in h are predicted in Exp. 14 (Fig. 7) in which the geostrophic wind is zero. Here h from the MLM is about 150 m less than

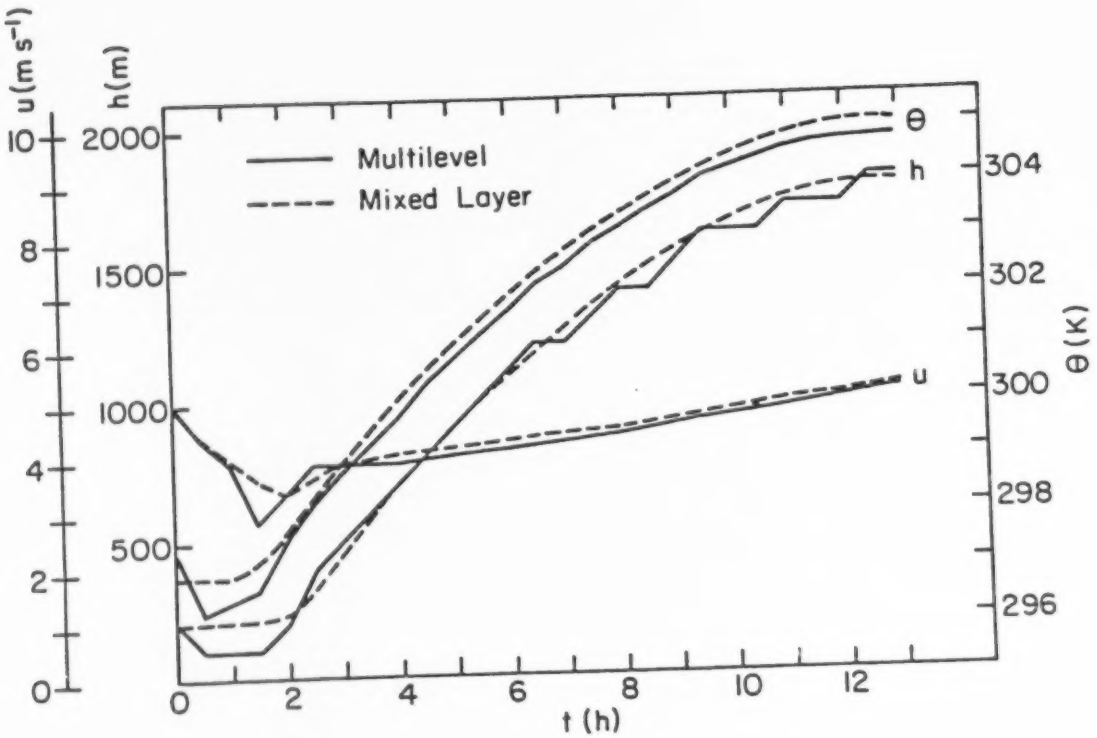

Figure 6. Temporal variation of θ(K), h(m) and u ($m\ s^{-1}$) over 13 h simulation 13 (geostrophic wind = 5 $m\ s^{-1}$) for XLM and MLM.

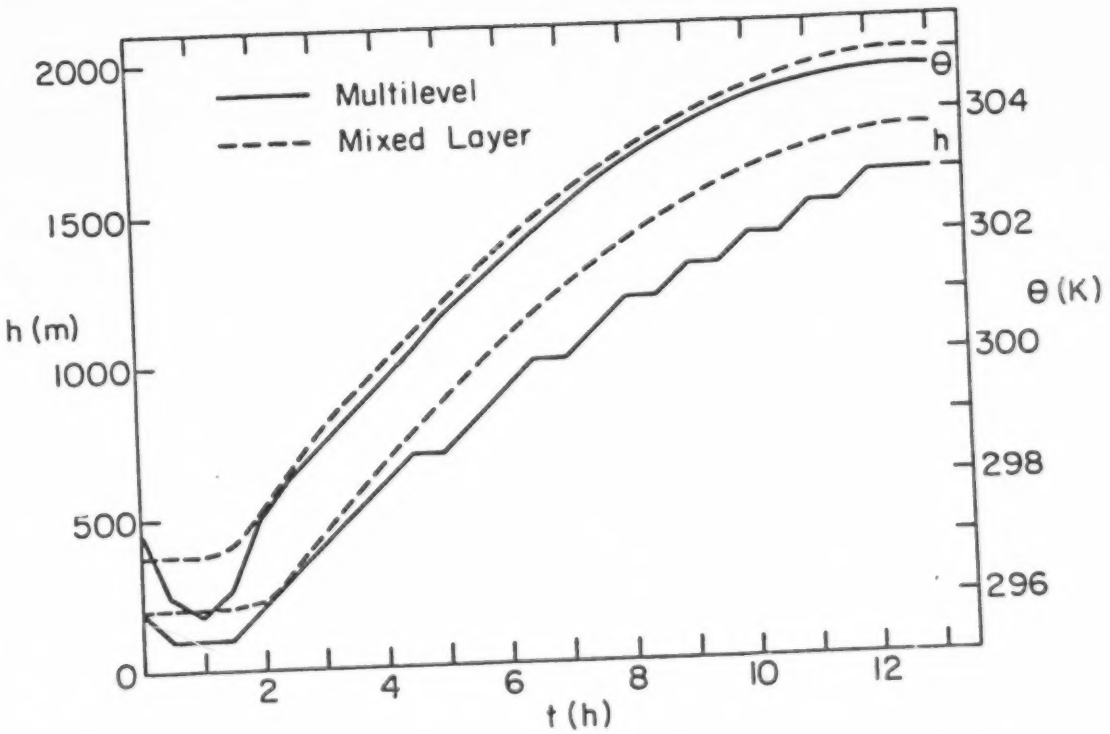

Figure 7. As in Fig. 6 except for simulation 14 (geostrophic wind=0).

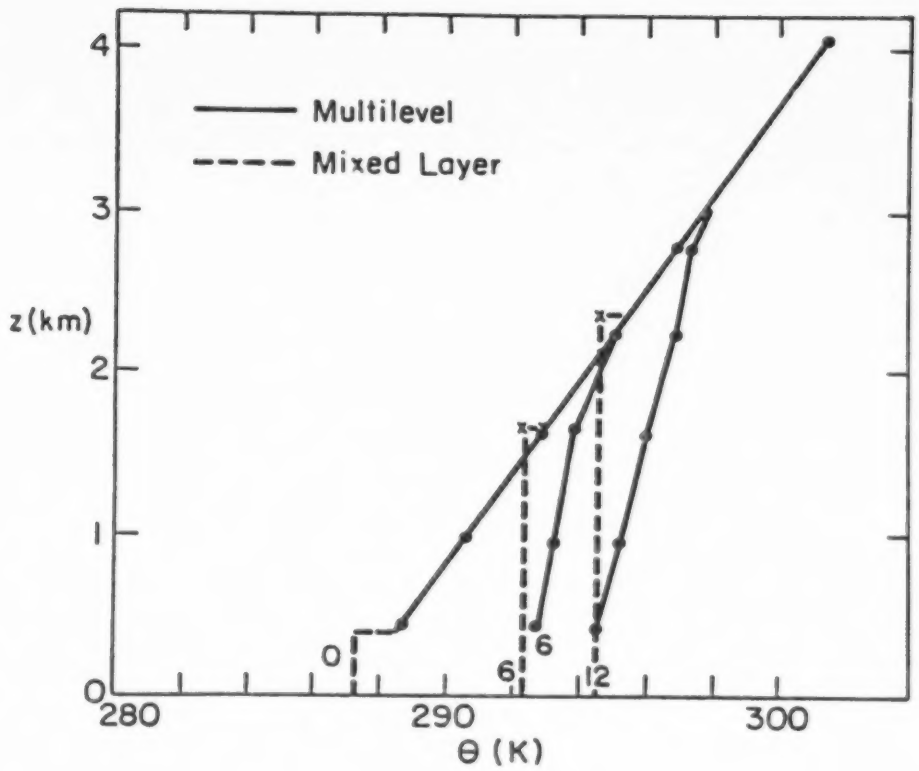

Figure 8. Potential temperature sounding at 0, 6, and 12 h at inland point far from coast as predicted by the XLM and MLM in a sea-breeze simulation over flat terrain.

PRECEDING PAGE BLANK-NOT FILMED

Table 2 Characteristics of sea breeze simulations with mixed layer and multilevel model

	Sea Breeze	Israel
Δx_{min} (km)	10	7.3
land:	$-310 \text{ km} \leq x < 0 \text{ km}$	$-230 \text{ km} \leq x \leq 0 \text{ km}$
sea:	$0 \text{ km} \leq x < 510 \text{ km}$	$0 \text{ km} \leq x \leq 80 \text{ km}$
coast at:	0 km	0 km
θ^i (K)	287.2	variable
$\theta(h)^i$ (K)	288.5	$\theta^1 + 1.0$ K
$h^i - z_s$ (m)	400	400
f (s^{-1})	1.0×10^{-4}	7.27×10^{-5}
γ^i (K km^{-1})	3.5	4.66
α (fraction of S_o in surface heating function)	0.25	0.288

Characteristics of both simulations

$K_{mH} = K_{\theta H} = 2.5 \times 10^4 \left(\frac{\Delta x}{\Delta x_{min}}\right) m^2 s^{-1}$

$u^i = v^i = 0$

z_o: 0.04 m land
0.00164 m sea

$V_g(H) = 0$

$C_D = 7.0 \times 10^{-3}$ over land, 1.5×10^{-3} over sea

$\rho(z_s) = 1.16 \text{ kg m}^{-3}$

$\rho(H) = 0.85 \, \rho(z_s)$

Boundary conditions:

u,v = 0 at west and east boundaries

θ,h forecast neglecting horizontal advection terms

The MLM contains 12 layers bounded by sigma ($\sigma = \frac{p-p_t}{p_s-p_t}$) levels 0.0, 0.2, 0.4, 0.6, 0.68, 0.72, 0.76, 0.80, 0.84, 0.88, 0.92, 0.96 and 1.0. The pressure, p_t, at the top of the model is 200 mb and the time step is 17 s.

Before comparing the simulations from the two models, we present a brief description of results from the MLM simulation to show how the complete (and presumably more accurate) solution evolves. The horizontal and vertical circulation is revealed by the streamfunction at 4, 8 and 12 h (Fig. 9). The streamfunction, which has dimensions of pressure/time, is related to the u-component and $\dot{\sigma}$ by the relations $p^*u' = \frac{\partial \psi}{\partial \sigma}$ and $p^* \dot{\sigma} = -\frac{\partial \psi}{\partial x}$, where $u'=u/L$, $x'=x/L$, L is a horizontal length scale and $p^*=p_s-p_t$. Because ψ is 0 on the boundaries, the overall intensity is given by the maximum streamfunction value. By this indicator, the circulation intensity increases rapidly from 4 to 8 h (38 to 115 x 10^{-6}cb s^{-1}), then increases more slowly between 8 and 12 h (115 to 134 x 10^{-6}cb s^{-1}). As found by Anthes (1978), the circulation center moves from the coast at 4 h to about 60 km inland at 12 h.

The circulation is close to its maximum intensity at 8 h. The maximum onshore flow of 4.7 m s^{-1} occurs just inland from the coast while the return flow reaches a maximum speed of 3.05 m s^{-1} at around 700 mb.

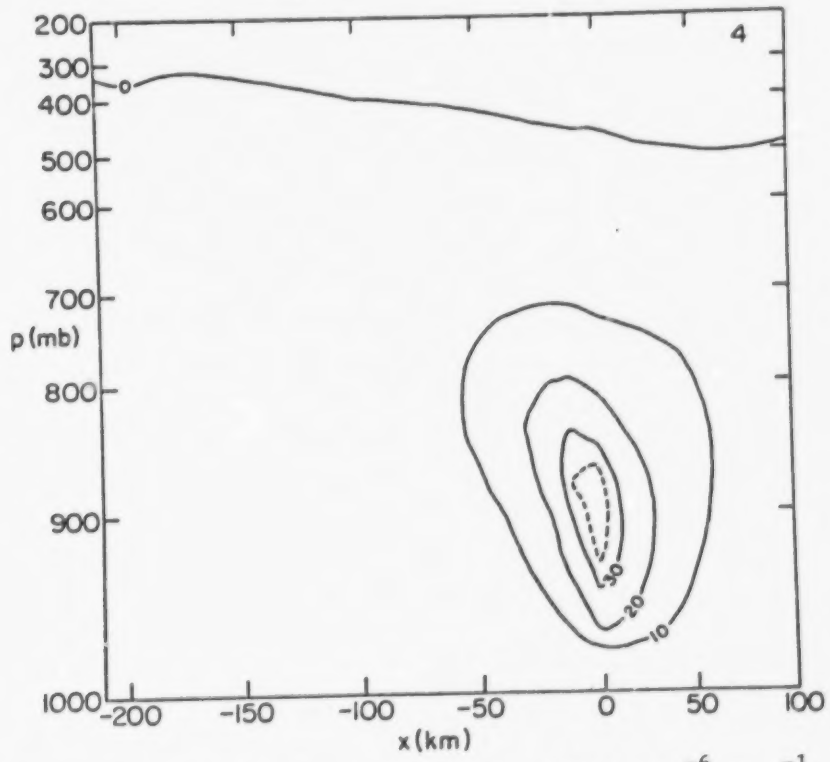

Figure 9a. at 4 h, maximum value of ψ is 38 x 10^{-6} cb s^{-1}.

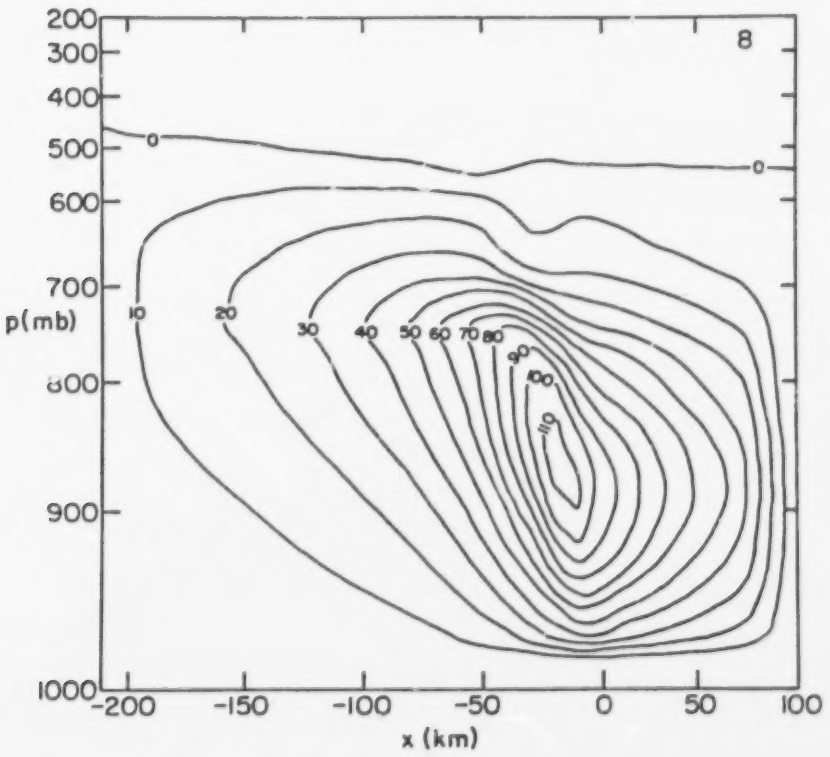

Figure 9b. at 8 h, maximum value of ψ is 115 x 10^{-6} cb s^{-1}.

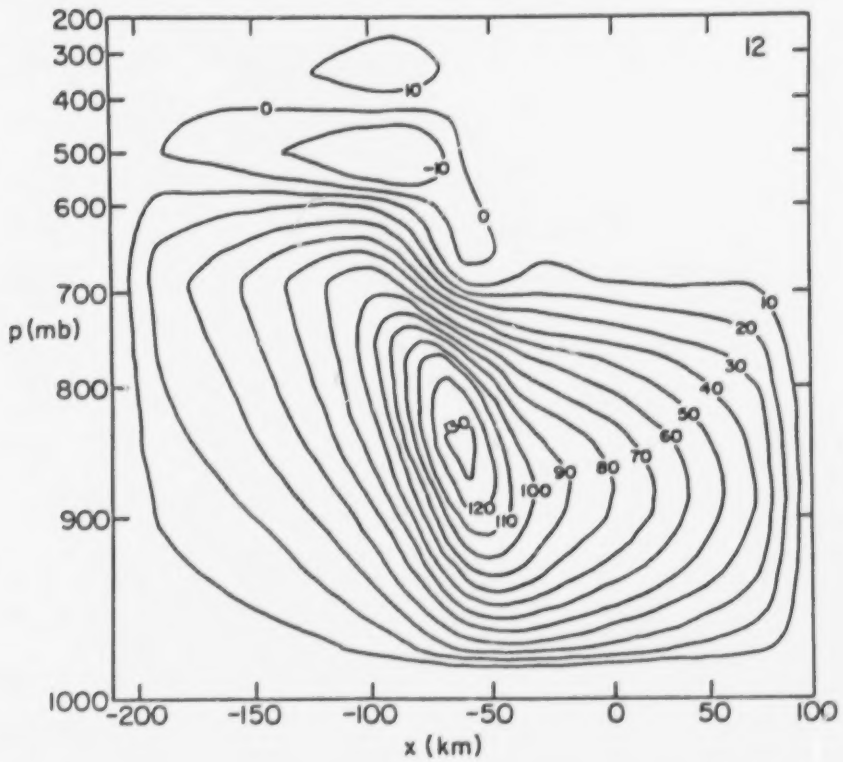

Figure 9c. at 12 h, maximum value of ψ is 134 x 10^{-6} cb s^{-1}.

Figure 9. Streamfunction of multilevel simulation of sea breeze over flat terrain. Contour interval is 10 x 10^{-6} cb s^{-1}.

The temperature change cross section (not shown) at 8 h indicates warming over land with a temperature increase of 5.5 K. It also shows slight cooling above the mixed layer (less than 0.5°C) and slight warming in the subsiding branch of the circulation ($\sim$ 1.0°C) over the water.

In comparing the behavior of the two models, we first consider the temperature change in the PBL and the growth of the mixed layer at the inland point farthest away from the coast, where the sea-breeze effect is minimal. Fig. 8 shows the temperature sounding at 0, 6 and 12 h at this point. While the XLM predicts a PBL with vertically constant θ (by definition), the MLM maintains a slightly stable lapse rate. However, the behavior of the mean PBL θ is similar in both models at this inland point.

The growth of the mixed layer depth with time at the inland location is shown in Fig. 10. While the behavior in both models is similar, the MLM shows a greater h (by about 500 m) late in the simulation. The difference probably results from uncertainties in diagnosing h, especially late in the day when the sounding becomes gradually more stable with elevation (Fig. 8).

Fig. 11 shows the spatial variation of h across the domain at 2, 4, 6, 8 and 12 h as predicted by the XLM. While h remains nearly constant over the water, it grows rapidly over land. The transition between land and water values of h occurs in a zone which varies from 20 km wide at 2 h to 80 km at 12 h.

The temporal evolution of the PBL potential temperature across the domain is illustrated in Fig. 12 for the two models. Both models show the region of maximum temperature gradient originating at the coast and moving inland during the day. The spatial and temporal variation of θ over land is quite

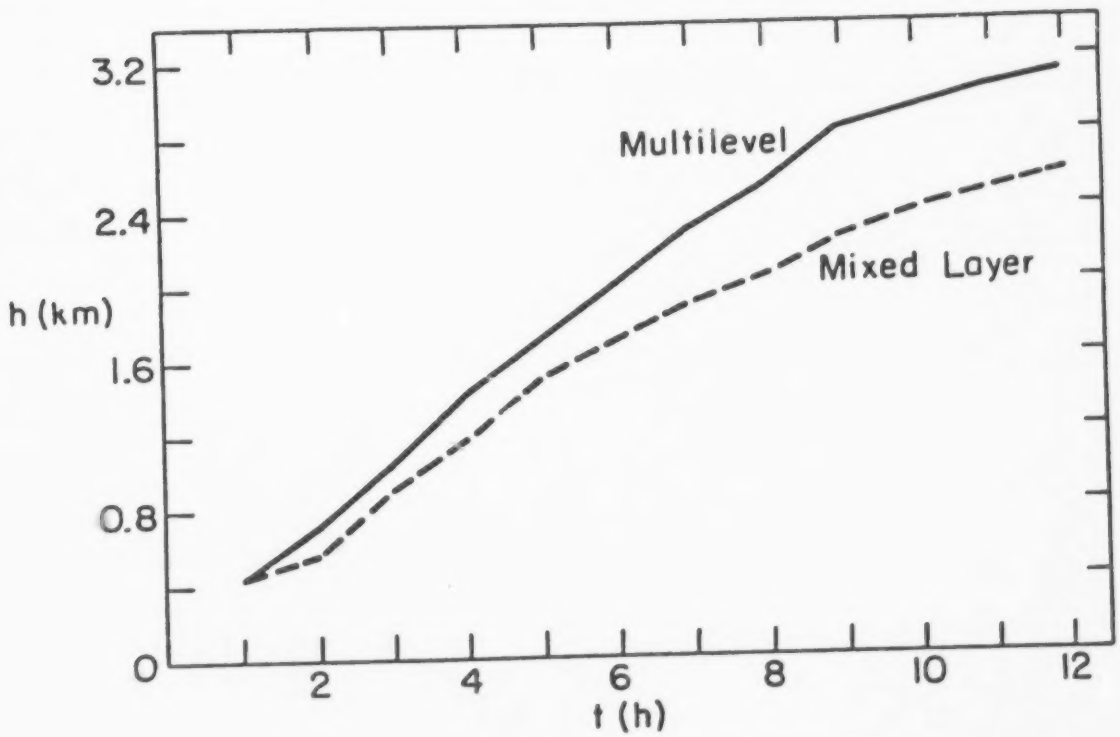

Figure 10. Growth of mixed-layer in XLM and MLM at inland point far from coast in sea-breeze simulation over flat terrain.

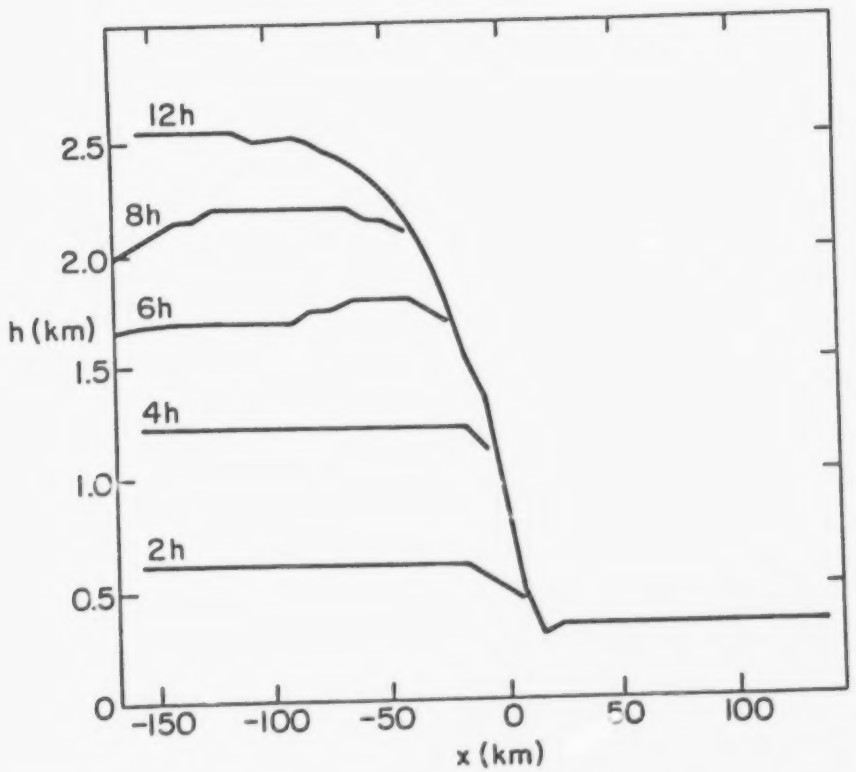

Figure 11. Height of mixed layer at 2, 4, 6, 8, and 12 h as predicted by XLM. The coast is at x=0, km.

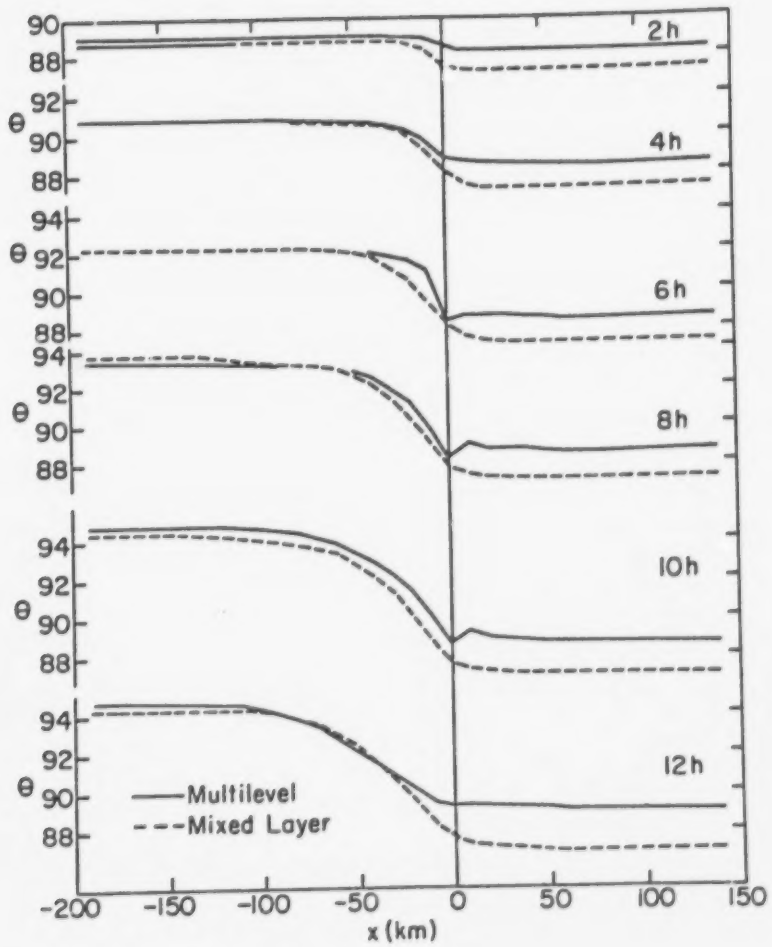

Figure 12. Horizontal profiles of mean potential temperature in mixed layer as predicted by XLM and MLM at 2, 4, 6, 8, 10, and 12 h in sea-breeze simulation over flat terrain.

similar in both models, the maximum difference being about 1°K. Over the water the MLM θ rises by slightly more than 1°K during the day due to subsidence. This warming does not occur in the XLM which preserves its initial value of θ . Overall it is evident that the XLM is capable of resolving the temporal and spatial behavior of PBL θ in a sea-breeze simulation.

Fig. 13 shows the spatial profiles of the u-component at the lowest level in the MLM, (u_s), the average value in the PBL of the MLM, ($\bar{u}$), and the value of $\bar{u}$ predicted by the XLM. Through 8-h the XLM faithfully reproduces the mean value of u in the MLM, with maximum differences being about 1 m s^{-1}. These values are naturally less than the value of u at the lowest level of the MLM since the strength of the sea-breeze winds decreases with height. Beginning around 8 hours, the two models show different behaviors of the predicted $\bar{u}$. While the maximum $\bar{u}$ in the MLM moves inland, reaching a point 50 km from the coast by 12 h, the maximum $\bar{u}$ in the XLM remains at the coast. During this time the XLM $\bar{u}$ becomes more westerly off the coast while $\bar{u}$ remains easterly in the MLM.

The above behavior of $\bar{u}$ in the XLM near the coast during the last four hours of the forecast is undoubtedly erroneous. It probably results from the inadequate parameterization of the layer above the PBL, in particular the modeling of the potential temperature between h, the height of the mixed layer, and H, the assumed depth of the undisturbed layer. The determination of H is arbitrary. While it makes sense that H should rise during the day to remain at some significant elevation above the maximum height of the inversion, there is no physical basis for predicting H. Here, as in Keyser and Anthes (1977), H is assumed to be time dependent and proportional to the depth of the perturbation induced in the h field, so that

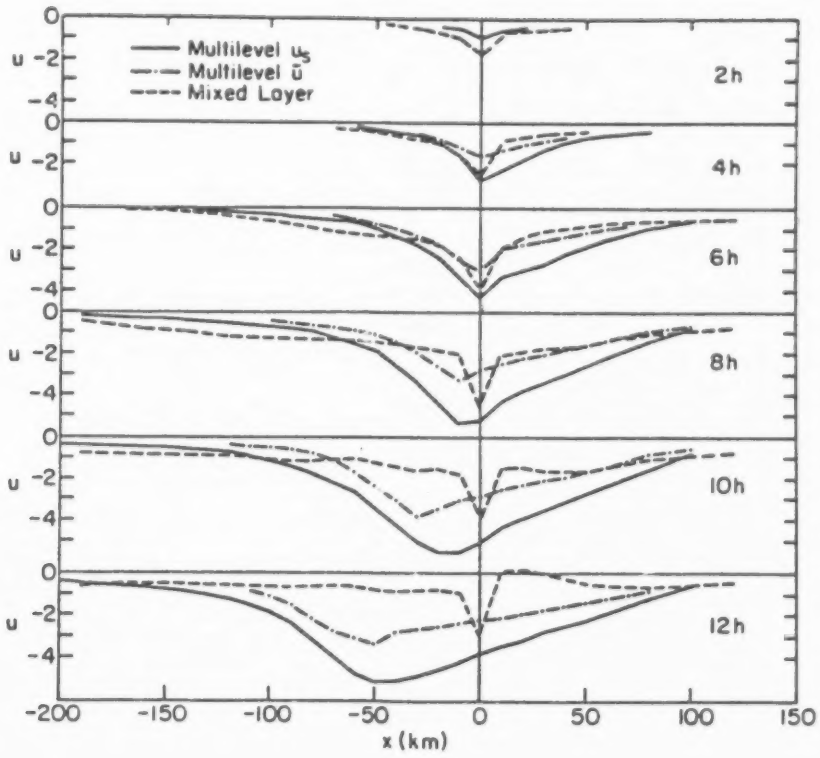

Figure 13. Horizontal profiles of u at lowest level in MLM, mean u in PBL from XLM and MLM at 2, 4, 6, 8, 10, 12 h in sea-breeze simulation over flat terrain.

$$H = \max \left\{ \begin{array}{l} 2h_{max} - \bar{h} \\ h_{max} + 1000\text{m} \end{array} \right\} . \qquad (9)$$

During the early portion of the forecast, the depth (H-h) is small over the water and coastal regions and the model is not too sensitive to the assumptions made concerning the thermodynamic structure between h and H. At 8h, however, the depth of this layer is 2600 m over the water, and small errors in the temperature structure can lead to significant erroneous accelerations in the mixed-layer wind. The acceleration due to the pressure gradient force in this simulation is (see Keyser and Anthes, 1977, Eq. 12)

$$\frac{du}{dt} = \frac{g(H-h)}{2\theta} \frac{\partial \theta(h)}{\partial x} - \frac{g(H-h)}{2\theta} \gamma \frac{\partial h}{\partial x} - \frac{g(\theta(h)-\theta)}{\theta(h)} \frac{\partial h}{\partial x} + \frac{gh}{2\theta} \frac{\partial \theta}{\partial x} \quad . \qquad (10)$$

$$(-1.3) \qquad (+0.88) \qquad (+0.39) \qquad (-0.14)$$

The numbers under each term are the accelerations (in 10^{-2} m s^{-2}) at 8h of the simulation at the coast, where the wind is strongest (Fig. 13). From (10), it is obvious that the inward acceleration is being maintained by the first term which contains the gradient in θ immediately above h multiplied by the depth (H-h). This term reflects the mean temperature gradient in the layer (H-h), which is illustrated by the isentropic cross section in Fig. 14. The steep slope of the isentropes across the coast is a result of subsidence. This subsidence, in turn, is forced by the divergent winds in the PBL.

The potential temperature $\theta(h)$ can change by two processes, convective adjustment and entrainment. Both processes increase $\theta(h)$ while also increasing

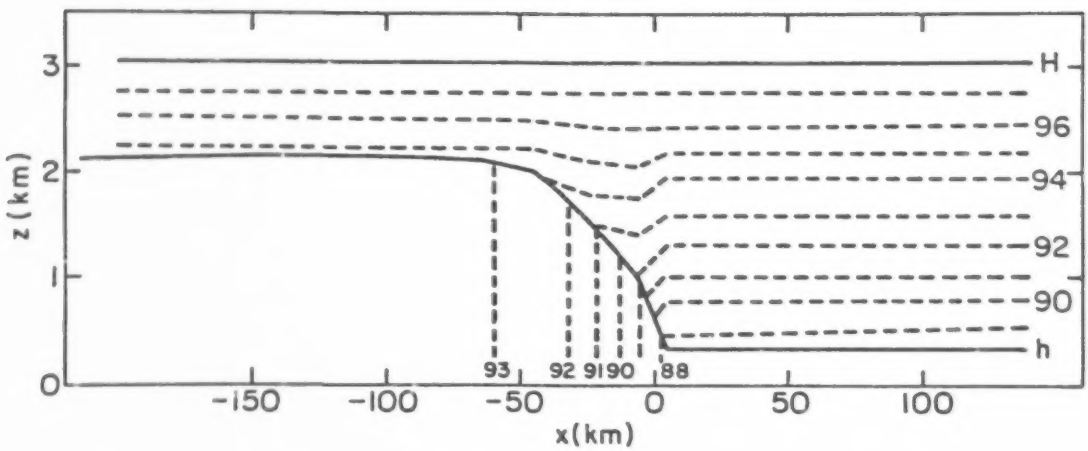

Figure 14. Potential temperature cross section at 8 h from XLM. Dashed lines are isentropes (θ-200 K).

h. Without vertical motion, the term involving $\gamma \frac{\partial h}{\partial x}$ in (10) compensates for the first term in a boundary layer growing entirely by heating from below. If PBL divergence exists, however, h will not rise as fast as predicted by the convective adjustment and entrainment terms. The result is the warm wedge of air above h as shown in Fig. 14. The greater the value of (H-h), the greater the effect of this temperature gradient will be. In the MLM, pressure forces in the layer above the PBL cause horizontal accelerations, producing a return flow which causes compensating pressure changes at the surface. The net effect is to allow the entire circulation, including the low-level inflow, to move inland.

Although the sea-breeze circulation is inherently two-dimensional, with an important part of the circulation occurring above the PBL, the XLM, which explicitly predicts only the mean PBL structure, does surprisingly well in reproducing the lower branch of the sea-breeze circulation. The mean potential temperature, horizontal winds, and height of the mixed layer are faithfully portrayed, at least for the first eight hours of the 12-h simulation. Beyond 8h, the uncertainties in the structure above the mixed layer result in a degradation of the XLM solution with time. The main difficulty is a failure of the onshore wind maximum to move inland during the late afternoon. We conclude that although the XLM is inferior to the MLM in simulating the sea breeze, it does model the main aspects of the low-level sea breeze and may have some use in coastal regions where an economical model is necessary.

4. Simulations over complex terrain and coastal region

In the previous comparison between the XLM and MLM, the terrain was flat so that the effects of the sea breeze alone could be isolated. In the second comparison, flow across topography similar to that of Israel is

modeled in order to compare the models in a situation with sloping terrain as well as a coast. The terrain used in this simulation consists of a coast at x=0, a ridge with elevation 960 m about 60 km east of the coast, a narrow valley about 100 km east of the coast, and a flat plateau of elevation 600 m extending eastward from the valley (Fig. 17). The characteristics of the XLM are given in Table 2.

a. Initialization of mixed layer model over variable terrain.

Because of the fundamental assumption of the existence of a layer of constant potential temperature in the XLM, initialization of the model under stable conditions requires an artificial modification of the temperature sounding. If the initial mixed layer is shallow, the modification should have little effect on the later forecast. The procedure used here is outlined below:

(1) Specify terrain height, z_s.

(2) Specify height, h, of PBL, usually some constant small value above z_s. Typically $h-z_s=400$ m.

(3) Diagnose height, H, of undisturbed layer using (9).

(4) Specify $\theta(H)$ from sounding

(5) Estimate $\gamma(\frac{\partial\theta}{\partial z})$ from sounding

(6) Calculate $\theta(h) = \theta(H) - \gamma(H-h)$

(7) Calculate $\theta(z_s) = \theta(H) - \gamma(H-z_s)$

(8) Define $\theta = (\theta(h) + \theta(z_s))/2$.

In regions of steeply sloping terrain the above method is preferable to that used by Keyser and Anthes (1977), which consisted of specifying h to be spatially constant at some value which was above the highest terrain elevation. This method requires unrealistically large initial values of h for stable conditions.

The initial values of H and $\theta(H)$ are saved for use in calculating $\theta(H)$ during the forecast as H rises,

$$\theta(H^t) = \theta(H^o) + \gamma(H^t - H^o) \tag{11}$$

b. Multilevel simulation

The streamfunction at 4 and 8 h is shown in Fig. 15. The circulation associated with the sea breeze is inhanced by the ridge in the center of the domain, as found by Mahrer and Pielke (1977). The maximum value of the streamfunction is about 65 x 10^{-6}cb s^{-1} at 4 h compared with a value of 38 x 10^{-6}cb s^{-1} in the sea-breeze simulation without a ridge (compare Figs. 15a and 9a).

During the early part of the simulation (0-4 h), three distinct circulations occur (Fig. 15a). The strongest is associated with the combined sea breeze and valley breeze over the sloping terrain between the ridge and the coast. At the coast the wind exceeds 4 m s^{-1} near the surface. Somewhat weaker circulations are generated over the sloping terrain on either side of the valley. Maximum horizontal velocities associated with these lesser circulations are about 1.7 m s^{-1}. As the heating continues, the two weaker valley circulations disappear (Fig. 15b). The intensity and scale of the main sea-breeze circulation cell increase and eventually this cell dominates the entire domain. Westerly winds cross the central ridge as found by Anthes and Warner (1978b).

The potential temperature distribution at 8 h is shown in Fig. 16. Notable features include cool air over the water, hot air over the eastern plateau, and a zone of temperature gradient between the ridge top and the coast. The height of the PBL, shown by the kink in the isentropes, slopes upward from the coast. The initial shallow pool of cold air has been

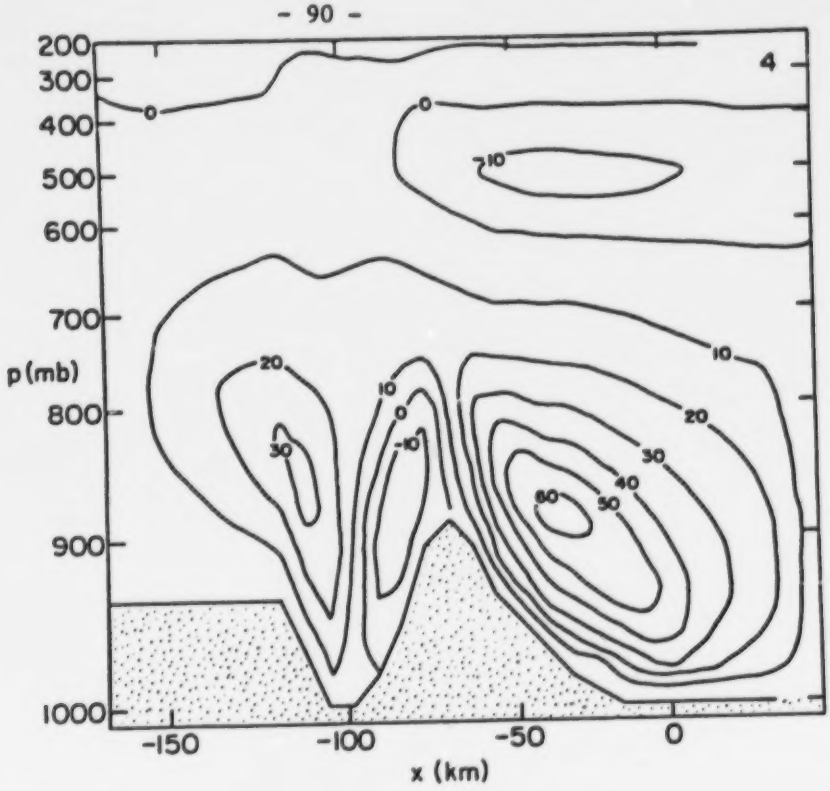

Figure 15a. at 4 h. Extreme values of ψ associated with three low-level circulations are (left to right) 34, -14, 66 x 10^{-6} cb s^{-1}.

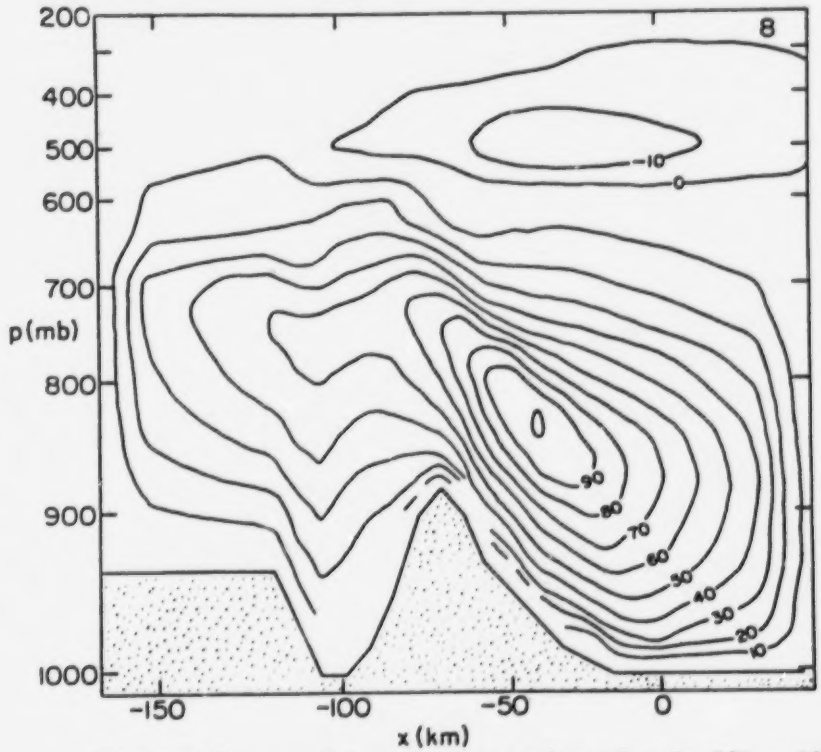

Figure 15b. at 8 h. Maximum value of ψ is 101 x 10^{-6} cb s^{-1}.

Figure 15. Streamfunction in multilevel simulation of sea-breeze over complex terrain. Contour interval is 10 x 10^{-6}cb s^{-1}. The coast is at x=0 km.

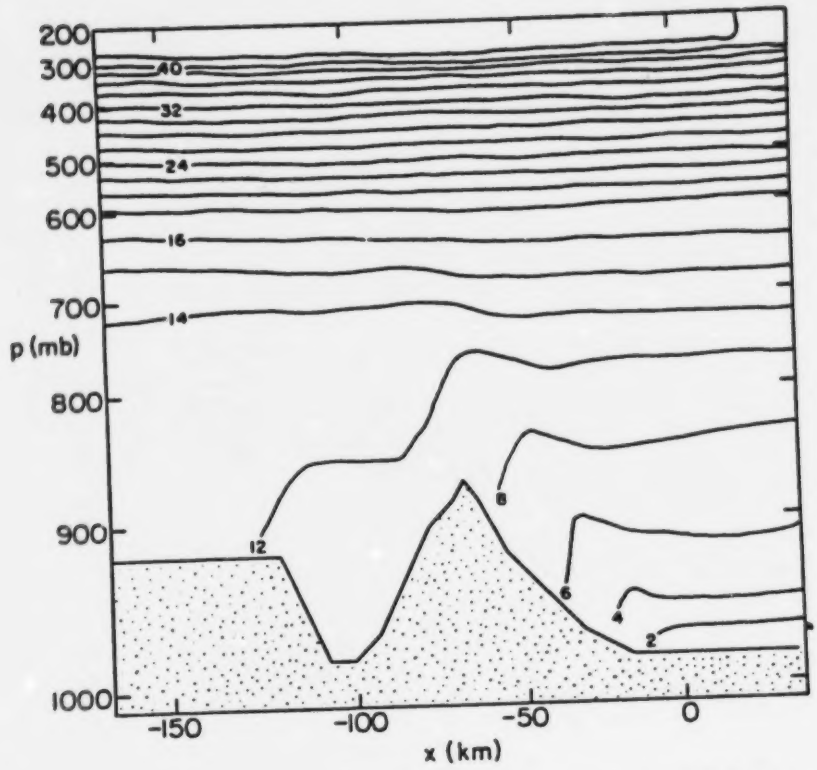

Figure 16. Isentropic cross section (θ-300K) at 8 h in MLM simulation of sea breeze over complex terrain. The coast is at x=0 km.

eliminated in the valley. The dip in the isentropes over the western slope of the ridge and above the PBL is a result of the subsiding branch of the circulation (Fig. 15b).

In summary, the introduction of the ridge-valley-plateau system parallel to the coast adds significant complications to the simple sea breeze. The depth and slope of the induced circulations pose a difficult challenge for the XLM.

c. Multilevel and mixed layer simulations

Fig. 17 shows the horizontal profiles of mean PBL θ at 0, 2, 4, 6, 8, 10 and 12 h for the two models. As in the previous simpler simulations, the agreement is very good, with differences generally less than 1 K over the land. As in the simple sea-breeze simulation, subsidence over the water produces a warming in the MLM which is not observed in the XLM. Also, the maximum temperature gradient tends to be advected inland in the MLM while remaining at the coast in the XLM.

Fig. 18 depicts the evolution of the mean horizontal wind component u. Early in the simulation, both models indicate west winds from the water to the ridge and upslope winds on both sides of the valley. By 6 h the west winds have vanished as the valley circulation becomes dominated by the main sea-breeze circulation. There are significant differences in the mean u-profiles predicted by the two models during the last six hours of the simulation, especially near the coast and ridge. The XLM shows much weaker westerly flow; in particular, it does not develop the maximum over the peak as does the MLM. Part of this problem is the failure of the XLM to move the sea-breeze circulation inland, a difficulty noted in the simple sea-breeze circulation (see Fig. 13). Furthermore, the XLM develops unrealistic offshore

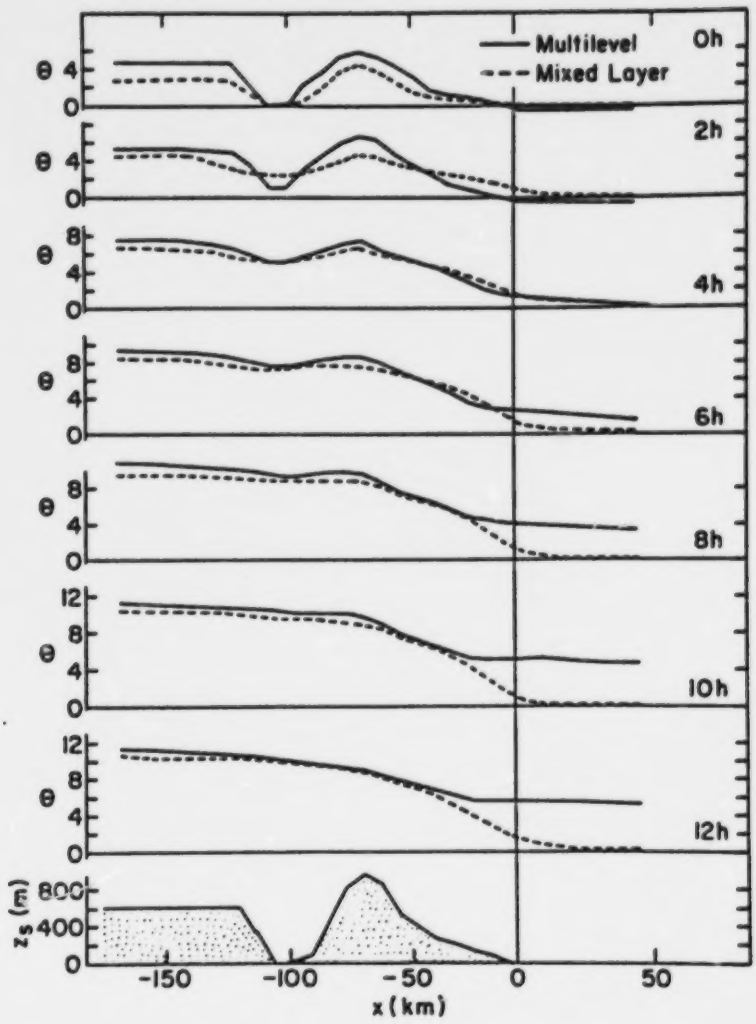

Figure 17. Horizontal profiles of mean potential temperature in mixed layer as predicted by XLM and MLM at 0, 2, 4, 6, 10, 12 h in sea-breeze simulation over complex terrain.

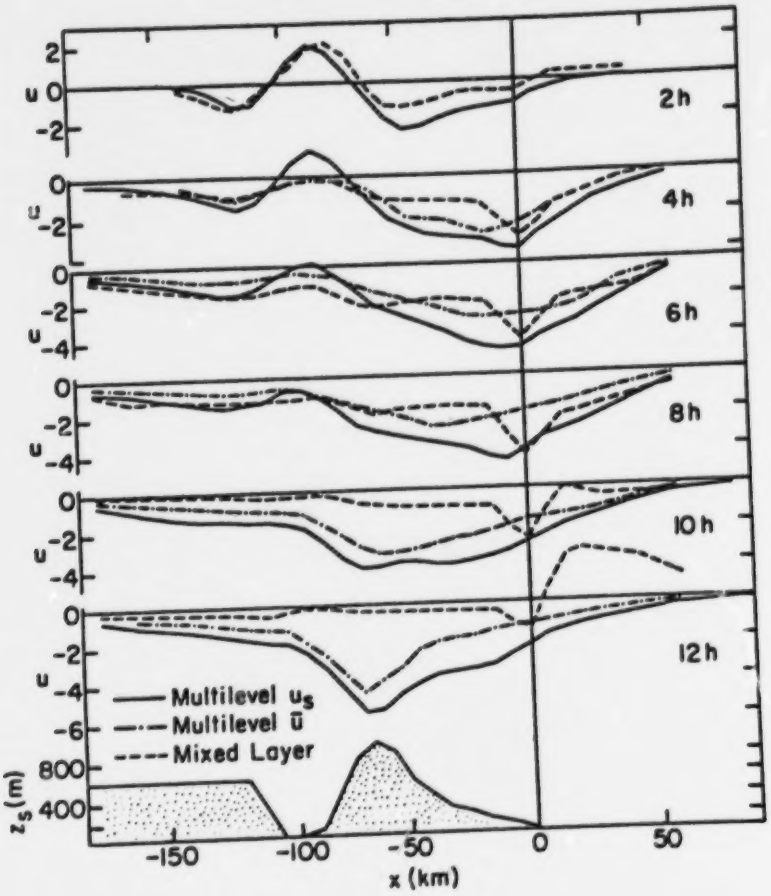

Figure 18. Horizontal profiles of u at lowest level in MLM, mean u in PBL from XLM and MLM at 2, 4, 6, 8, 10 h in sea-breeze simulation over complex terrain.

winds at 12 h, in contrast to the weak onshore winds which are maintained by the MLM.

Because the depths of the mixed layers (Fig. 19) and the potential temperatures are similar in both models, these unrealistic features of the XLM flow must be related to the parameterization of the upper layer. At 8 h the height of the "undisturbed" layer in the XLM is diagnosed to be 3.9 km, which corresponds to a pressure of about 625 mb. As shown by the circulation in the MLM (Fig. 15b), significant perturbations to the flow exist above this level. More importantly, the vertical variations in the lapse rate above h associated with the tilted isentropic pattern (Fig. 16) cannot be represented by the XLM. Thus temperature gradients immediately above h persist throughout the entire layer (H-h) (see Fig. 14 for example). These factors, and the fact that (H-h) becomes large late in the forecast, makes the sum of the first two terms in the pressure gradient force (10) much larger than the last two. Uncertainty in these largest terms then makes the entire pressure gradient inaccurate. An evaluation of the terms in (10) at x=15 km (the point of maximum offshore flow) at 12 h showed the four terms to be +0.9, +31.3, +1.3, and -18.7×10^{-5} m s^{-2} respectively. Thus the unreasonable winds arise from an improper balance between the first two terms.

5. Summary

The mean structure of temperature and wind within the PBL as predicted by a mixed layer and multilevel model was studied for a variety of physical situations. Under horizontally homogeneous conditions the XLM predicted values of θ, V, and h which agreed closely with the mean values predicted by the MLM, both with and without heating. When horizontal inhomogeneities

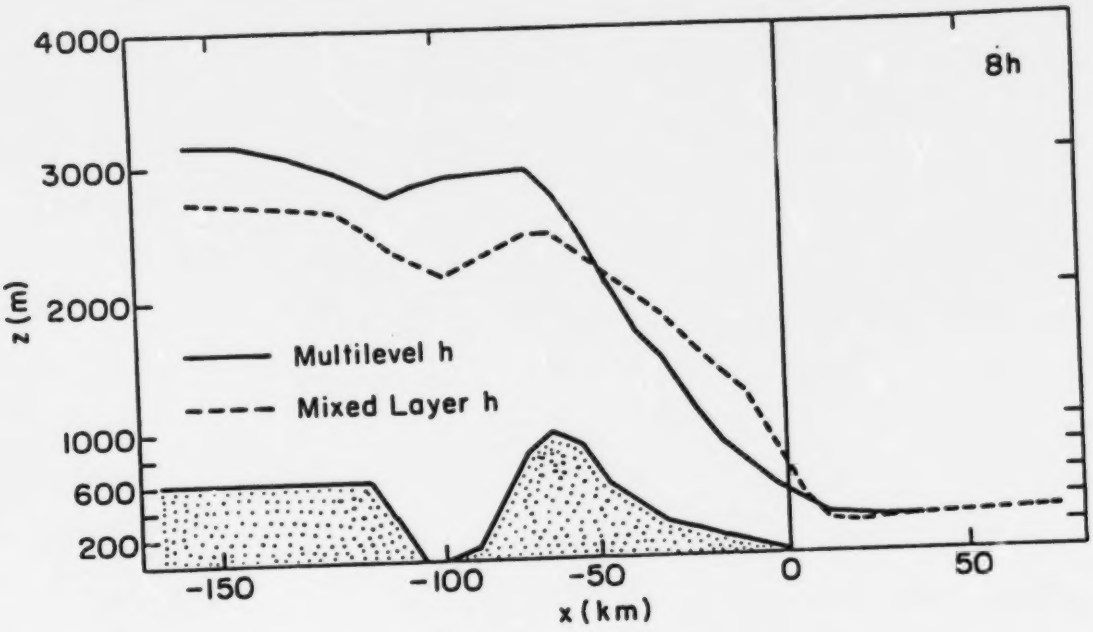

Figure 19. Height of PBL at 8 h as predicted by XLM and MLM in sea-breeze simulation over complex terrain.

associated with differential heating were introduced, the XLM solutions in the PBL became less accurate when compared to the MLM solutions. In a simple sea-breeze simulation over flat terrain, the XLM failed to move the onshore winds inland during the day, presumably because of erroneous treatment of mass and wind adjustments above the PBL. Variable terrain exacerbates the discrepancy between the XLM and MLM found in the later stages of the simple sea-breeze simulation. While the mean PBL flows agreed fairly well during the first several hours of the heating cycle when the depth (H-h) is not very large, the flow in the XLM became unrealistic near the coast and ridge during the latter half of the simulation. The unreasonable winds develop because the XLM is unable to represent perturbations in the flow above the mixed layer, in particular the tilted nature of the temperature pattern aloft. Thus mixed layer models in general appear to have distinct limitations when trying to resolve PBL flow over complex terrain under strong heating. For these conditions, a multilevel model appears to be essential to the correct prediction of flow within the PBL, since rather complicated adjustments in the mass field above the PBL produce important effects on the pressure gradient within the PBL.

Acknowledgments

This research was supported by U.S. Army Grant DAAG 29-76-G-0157 and EPA Grant R-805659-01.

References

Anthes, R. A., 1978: The height of the planetary boundary layer and the production of circulation in a sea-breeze model. J. Atmos. Sci., 35, 1231-1239.

Anthes, R. A. and T. T. Warner, 1978a: Development of hydrodynamic models suitable for air pollution and other mesometeorological studies. Mon. Wea. Rev., 106 1045-1078.

Anthes, R. A. and T. T. Warner, 1978b: Simulation of mesoscale flows over Israel. Israel Meteorological Research Papers Vol. II. Israel Meteor. Soc., Bet Dagan 93-123.

Busch, N. E., S. W. Chang and R. A. Anthes, 1976: A multi-level model of planetary boundary layer suitable for use with mesoscale dynamic models. Jour. Appl. Meteor., 15, p. 909-191.

Keyser, D. and R. A. Anthes, 1977: The applicability of a mixed-layer model of the planetary boundary layer to real data forecasting. Mon. Wea. Rev., 105, 1351-1371.

Lavoie, R. L., 1972: A mesoscale numerical model of lake-effect storms. J. Atmos. Sci., 29, 1025-1040.

Lavoie, R. L., 1974: A numerical model of trade wind weather on Oahu. Mon. Wea. Rev., 102, 630-637.

Mahrer, Y. and R. A. Pielke, 1975: A numerical study of the air flow over mountains using the two-dimensional version of the University of Virginia mesoscale model, Jour. Atmos. Sci., 32, 2144-2155.

Mahrer, Y. and R. A. Pielke, 1977: The effects of topography on sea and land breezes in a two-dimensional numerical model. Mon. Wea. Rev., 105, 1151-1162.

Pielke, R. A., 1974: A comparison of three-dimensional and two-dimensional numerical predictions of sea breezes. Jour. Atmos. Sci., 31, 1577-1585.

Warner, T. T., R. A. Anthes, and A. L. McNab, 1978: Numerical simulations with a three-dimensional mesoscale model. Mon. Wea. Rev., 106, 1079-1099.